Master’s thesis

On the effect of surface roughness on velocity profiles and runout lengths of dry granular flows

Submitted by:

Lukas Reider

00926677

to be awarded the degree of

Diplom-Ingenieur

at the University of Natural Resources and Life Sciences

Institute of Mountain Risk Engineering

Supervisor:

Assoc. Prof. Dr. Roland Kaitna

Co-supervisor:

Priv.-Doz. Dr. Christian Scheidl

Vienna, March 2020

Author’s Declaration

Unless otherwise indicated in the text or references, or acknowledged above, this thesis is entirely the product of my own scholarly work. Any inaccuracies of fact or faults in reasoning are my own and accordingly I take full responsibility. This thesis has not been submitted either in whole or part, for a degree at this or any other university or similar institution. This is to certify that the printed version is equivalent to the submitted electronic one.

March 20st, 2020 Signature

Gratitude

I want to express my special thanks to Professor Roland Kaitna for the professional discussions, his patience and supportive conversations during the whole time I worked on this topic. I would furthermore like to thank Friedrich Zott for the technical support in the laboratory.

A special thanks goes to my family starting with my parents, who made it possible for me to study, my siblings up to my daughter for their support during the last years of my studies through whom I could draw energy again and again. A very special thanks goes to my partner Christina Gobin for her endless patience, the enriching conversations and the proofreading of my work.

Kurzfassung

Gravitative Massenströme wie z.B. Murgänge, werden oft physikalisch als eine Ansammlung von Partikeln modelliert, die in vereinfachten Rinnenkonfigurationen fließen. Es gibt Hinweise, dass das natürliche Fließverhalten eine kombinierte Bewegung aus Gleiten und interner Verformung aufweist. Dies ist nach wie vor noch nicht vollständig erforscht und auch in Laborexperimenten unterrepräsentiert.

In dieser Masterarbeit wird der Einfluss der Oberflächenrauigkeit auf das Geschwindigkeitsprofil, das basale Gleiten und die Auslauflänge von trockenen, granularen Lawinen anhand von kleinskaligen Laborversuchen untersucht. Der Versuchsaufbau besteht aus einem 0,17 m breiten Kanal mit einer Neigung von 34° auf den ersten 1,5 m. Anschließend folgt eine 0,8 m lange, gekrümmte Übergangszone mit einem Radius von 1,7 m, welche anschließend in einer Auslaufzone mit einem Winkel von 4° endet. Das getestete Material bestand aus nicht perfekt kugelförmigen Keramikkugeln mit einem Durchmesser von 2,8 bis 4,3 mm. Vier verschiedene Arten von Oberflächenrauigkeiten im Bereich von 0 bis 6 mm Höhe und zusätzlich eine Makrorauigkeit, die höher als die maximale Fließhöhe war, wurden getestet. Um auch Informationen über den Einfluss der relativen Rauigkeit zu erhalten, wurden Experimente mit drei verschiedenen Startvolumina durchgeführt. Alle vierzehn verschiedenen Variationen wurden dreimal wiederholt. Die Fließhöhen wurden mit Lasersensoren an vier verschiedenen Positionen entlang des Kanals gemessen. Drei davon wurden zur Berechnung der mittleren Frontgeschwindigkeit der strömenden Masse in zwei Querschnitten verwendet. Darüber hinaus wurden die Experimente mit einer Hochgeschwindigkeitskamera durch eine Seitenwand aus Acrylglas aufgezeichnet. Die Aufzeichnungen wurden mittels PIV (Particle Image Velocimetry) analysiert, um Geschwindigkeitsprofile in 1/1500 Sekunden Schritten abzuleiten. Die Ergebnisse zeigen, dass sich die Geschwindigkeitsprofile vom Kopf bis zum Endbereich der Lawine änderten und dass die Profile der beiden rauesten Oberflächen ähnlicher sind als jene mit der geringsten Rauigkeitskonfiguration. Der Anteil des Gleitens an der Gesamtbewegung variierte zwischen Null und der gesamten Bewegung. Die Auslauflänge verringerte sich je höher die Rauigkeit war und erhöhte sich mit höherem Startvolumen. Die Form der Geschwindigkeitsprofile änderte sich mit der Oberflächenrauigkeit und mit dem Startvolumen. Nur die Geschwindigkeitsprofile für die beiden rauesten Oberflächen zeigen unabhängig vom Startvolumen einen klaren Wendepunkt. Die Experimente unterstreichen die Bedeutung der Oberflächenrauigkeit sowie der relativen Rauigkeit für granulare Massenbewegungen und liefern weitere Daten, um Modelle zu testen.

Abstract

Gravitational mass flows like debris flows are often physically modelled as an assembly of particles flowing in simplified flume configurations. There is indication that natural flows exhibit a combined movement of sliding and internal deformation, which is not well understood and underrepresented in scaled laboratory experiments.

In this master's thesis the effect of surface roughness on velocity profiles, basal sliding, and the runout of small-scale, dry granular avalanches is investigated. The experimental setup a 0.17 m wide flume with an inclination of 34° for the first 1.5 m, following an 0.8 m curved transition zone with a radius of 1.7 m, and ending in a runout zone with an angle of 4°. The tested material consisted of non-perfect spherical ceramic beads with a diameter of 2.8 to 4.3 mm. Four different types of surface roughness ranging from 0 to 6 mm height and additionally one macro roughness, which was higher than the maximum flow height, were tested. To also get information about the influence of the relative roughness experiments with three different starting volumes were undertaken. All fourteen experimental variations were repeated three times. Flow heights were measured with laser sensors at four different positions along the channel. Three of them were used to calculate the mean front velocity of the flowing mass in two cross sections. Furthermore, the experiments were recorded with a high-speed camera through one sidewall out of acrylic glass. The recordings were analysed using a PIV (Particle Image Velocimetry) software to derive velocity profiles in 1/1500 second time steps. Results show that the velocity profiles changed from the head to the tail of the flow and that the profiles of the two roughest surfaces are more alike than the smooth roughness configurations. The fraction of sliding on the total movement varied between 0 and close to unity. The runout lengths decreased the higher the roughness was and increased with higher starting volume. The shape of the velocity profiles at the deepest sections of the flows changed with surface roughness and with starting volumes. Only the velocity profiles for the two roughest surfaces show a clear inflection point independent from starting volume. The experiments highlight the importance of surface roughness as well as relative roughness for granular mass flows and provide data for model testing.

Table of content

List of figures

List of tables

List of abbreviations

CLAHE	Contrast limited adaptive histogram equalization
DCC	Direct cross correlation
DFT	Discrete Fourier transform
IAN	Institute of Mountain Risk Engineering
L1	Laser sensor one
L2	Laser sensor two
L3	Laser sensor three
L4	Laser sensor four
(D)PIV	(Digital) Particle Image Velocimetry
R0	Roughness 0 mm
R1	Roughness 2 mm
R2	Roughness 4 mm
R3	Roughness 6 mm
RxW	Adaptable macro roughness with sticks Ø 5 mm (x = 0 to 3 for roughness R0, R1, R2, R3)
V1	Volume 1 with a mass of 7.0 kg
V2	Volume 2 with a mass of 3.5 kg
V3	Volume 3 with a mass 10.5 kg
WLV	Wildbach- und Lawinenverbauung/ Austrian Service for Torrent and Avalanche Control

1 Introduction

„Debris flows are amongst the most frequent and destructive of all geomorphic processes, they mainly affect mountainous areas in a range of morphoclimatic environments and the damage they cause is often devasting. Increased anthropisation calls for improvements in the criteria used to identify debris-flow risk areas and the prevention measures adopted." [1]

Physical modelling of debris flows, which is used in various simulation software, is one way to support experts in predicting vulnerable areas. They all are based on simplified models to capture the complex behaviour of gravitational mass flows. For this purpose, it is necessary to understand the flow behaviour of natural flows to represent them as accurately as possible. To gain more understanding of this important topic and besides, to provide data for further model testing, the effect of surface roughness on velocity profiles and runout lengths of dry granular avalanches was investigated in this master's thesis. There is indication that natural flows exhibit a combined movement of sliding and internal deformation, which is not well understood. Therefore, small scale laboratory experiments are carried out. In the different experimental configurations, the height of the surface roughness is varied. Since the height of the surface roughness always must be considered in relation to the flow height, different starting volumes are tested. Hence, 14 different setups with three repetitions each are undertaken, leading to a total of 42 experiments.

The master's thesis is divided into a theoretical and a practical part. In the first, the problem statement and the research questions are formulated. Additionally, a short introduction on the topic and the relevant terminology is given to ensure a homogenous understanding of the used terms and theories. The practical part consists of the methodology used, including the experimental setup, the measurement techniques, as well as how the data obtained was processed. Moreover, this part presents the results and provides a discussion.

[1] Lorenzini, G. and Mazza, N. (2004), p. 1.

2 Problem statement and research questions

Debris flows cause damages worth millions every year. Millions also flow into protective structures to protect inhabited areas. Giving a general example, the total economic damage caused by natural catastrophes internationally in 2017 was about 340 billion US-Dollars. Since, experts calculate with an average annual damage of more than 200 million Euros for Austria.[2] From 2002 to 2011, the Austrian Federal Government invested more than 1.8 billion Euros in the protection against natural disasters[3] but investments usually come from several sources. One of the most recent projects, which is also the largest investment of the Austrian Forest Service for Torrent and Avalanche Control (WLV) up to date, is the protection project "Saalach 2018" in Salzburg. Here, the first protective measures range from flood and bed load retention to the stabilization of sliding slopes. The sum of total investment for this huge project is calculated with 58 million Euros, whereas the Austrian Federal Government invests 60 %, the province of Salzburg invests 15 % and the water cooperative invests the remaining 25 %.[4]
Having the economical aspect on one side and the human aspect – with i.e. injuries and the loss of homes – on the other side, it is necessary to be able to predict which areas are affected as accurately as possible. Different model approaches exist to simplify the complex behaviour of gravitational mass flows. These models are used to predict affected areas and to substantiate expert statements.[5] However, these models are based on strong simplifications of these processes as we lack a sound understanding of the actual mechanics of debris flows. For example, there is an indication that natural flows exhibit a combined movement of sliding and internal deformation. In order to be able to improve the models, further research on the flow behaviour of gravitational mass flows is necessary.

Most previous laboratory experiments were done on smooth surfaces like metal and with uniform roughness heights not higher than the mean diameter of the flowing material[6], or with an erodible layer[7]. However, it is important to also investigate how the velocity profiles change on different heights of surface roughness and to get a better understanding of the relative importance of basal sliding and internal deformation within gravitational mass flows.

---

2 VVO Versicherungsverband Österreich (2018) (see web sources).

3 BMLFUW (2012).

4 Wildbach- und Lawinenverbauung und Schutzwaldpolitik (Abteilung III/4) (2019) (see web sources).

5 Kaitna, R. et al. (2007), p. 71.

6 cf. Hungr, Oldrich (2008).

7 cf. Armanini, Aronne et al. (2005).

It has not yet sufficiently been researched which boundary conditions in which form influence the flow of gravitational mass movements. In most rheological models, bulk flow resistance is represented by one or two parameters. It is not clearly defined how these parameters are influenced by the several boundary conditions. Therefore, the aim of this master's thesis is to investigate how runout distance and flow behaviour of dry granular avalanches change with changing boundary conditions. In particular, the influence of surface roughness shall be investigated.

To limit the number of influencing parameters, the available test flume has a constant width over its entire length and the test channel is straight and not bent. Therefore, there is no lateral distribution of deposits. There are no obstacles along the path on the roughness R0 to R3. Only the adaptable macro roughness RxW can be considered as an obstacle. Regarding the runout distance, the shape of the granular avalanche and the occurring velocities on different types of surface roughness, three research questions (RQs) are formulated:

RQ 1: How does the surface roughness affect the runout distance of dry granular avalanches?

RQ 2: How does the surface roughness affect the velocity profiles?

RQ 3: How does the surface roughness affect the flow height and does the relative roughness play a role?

3 Overview of relevant terminology

This chapter provides a short overview of the most relevant terminology to ensure a common understanding in the practical part of the thesis. Additionally, some rheological models for the basal shear resistance are presented.

3.1 Gravitational mass flows

Gravitational mass flows are gravity-driven mass movements on slopes[8] where a transformation of potential energy into kinetic energy takes place.[9] They can range from dry granular flows to water saturated viscous flows. Examples for such gravitational mass movements are debris flows, lahars, rock and snow avalanches.[10] The experiments in this master's thesis were carried out with dry granular material which means that the particles alone, and not the intermediate medium, play the greatest role in momentum transport. Campbell (1990) divided granular flows into slow and rapid flows, depending on their behaviour as an elastic solid or a fluid. In the elastic solid behaviour, the load is supported through frictional bonds. If those bonds are overcome, the system fails but the particles stay in contact and start to flow as many particle-blocks in a "quasistatic" flow regime. On the other hand, if the motion is rapid enough, a rapid-flow regime occurs where the particles move independently of their neighbours.[11] Moreover, granular flows can be divided into three classes: the "quasistatic" where grain inertia can be neglected, the "gaseous" when the medium is strongly loosened up and the "liquid" regime with a dense flow where grain inertia becomes important.[12] Furthermore, a distinction must be made between viscous and dry granular flows. In dry granular flows, the dominating forces are acting due to friction and collision of the grains. In viscous suspensions, the interaction between the grains and the surrounding fluid affects the rheological behaviour.[13] So, the pore pressure can reduce the internal friction and lead to a complete liquefaction.[14] Due to these complex processes, the mobility of granular mass movements can be increased significantly. Consequently, the experiments in this master's thesis are undertaken with dry granular material only, to separate the effect of surface roughness.

8 Gollin, Devis (2017), p. 6.

9 Fischer, Jan-Thomas et al. (2018), p. 1.

10 Heiser, M. et al. (2017), p. 2.

11 Campbell, C S (1990), p. 1, 2.

12 GDR MiDi (2004), p. 341.

13 Pellegrino, Anna and Schippa, Leonardo (2017), p. 2.

14 Iverson, Richard M. (1997), p. 266,279,285.

3.2 Surface roughness – roughness due to bedform

In general, the roughness is a resistance to the flow which leads to a loss of energy. For open channel flows this resistance can be divided into the skin drag (grain roughness), the form drag (surface geometry like dunes) and the shape drag (channel shape like meanders).[15] In this thesis the surface roughness is defined as the height of the resistance elements on the channel bed, so the skin drag. In contrast to this, the resistance of the form of channel bed or the shape of the channel, i.e. the roughness due to the bedform, are the form drag and the shape drag. Examples are a step-pool or a cascade structure or the meandering of the channel. Further, the roughness height is defined as the diameter of the roughness elements, i.e. the grains of which the roughness consists of. The relative roughness is the roughness height in relation to the hydraulic radius.[16]

3.3 Runout parameters

"Runout parameters include the maximum distance reached, flow velocities, thickness and distribution of deposits, and behaviour in bends and at obstacles in the flow path." [17]

In the following experimental setup, the runout distance respectively runout length is defined as the maximum distance the material travels. Also, the thickness of deposits, flow heights perpendicular to the bed and flow velocities in the transition zone are measured to assess the runout distance. However, the runout zone is a straight, channelled flume with the same width over the whole length. Thus, no distribution of deposits can be measured.

3.4 Types of movement

From previous laboratory experiments different types of movement from basal sliding to internal deformation or a combination of both can be derived. In Figure 1 it is shown how velocity profiles change regarding the basal shear and internal deformation. Figure 1a represents the all-slip case. The grains at the base have the same velocity as on the surface i.e. the material is sliding as a block and there is no internal deformation. In Figure 1b a typical velocity profile of a fluid over a rigid base is shown. In this case no slip at the base occurs and the shear rate decreases with distance from the bed. Figure 1c illustrates a positive velocity at the bed and a changing velocity over the flow height. This means that here a combination of basal sliding and internal

15 Morvan, Hervé et al. (2008), p. 5.

16 Limerinos, J.T. (1970), p. 9.

17 Hungr, Oldrich (1995), p. 610.

deformation is present. At least in Figure 1d the velocity profile of a flow over an erodible bed, where the shape of the profile changes between the erodible base and the upper part, is shown.[18]

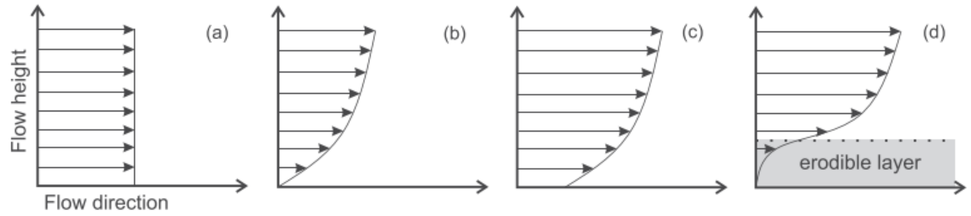

Figure 1: Schematic illustration of possible types of movement.

(a) Constant velocity profile with full basal sliding. (b) Flow profile over a rigid bed with no basal sliding. (c) Combination of basal sliding and internal deformation. (d) Flow over an erodible b

Source: Nagl, Georg et al. (2020), p. 2.

Furthermore, the shape of the velocity profile regarding the internal deformation can change, which is illustrated in Figure 2. The simplest modelling approach is when the shear rate changes linearly (dashed line in Figure 2). The dashed-dotted line describes a granular-type profile and the solid line a half-parabolic profile. With the dotted line a viscous or viscoplastic modelling approach is shown. In this modelling approach the internal deformation is described by a viscosity term. On the top a rigid plug layer can be seen. To take this solid-like behaviour in account a critical yield stress is employed (e.g. Herschel-Bulkley model).[19]

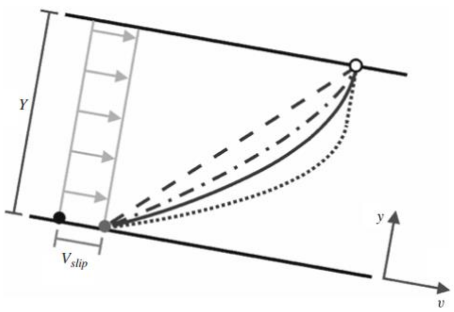

Figure 2: Illustration of the different shapes of velocity profiles over a non-erodible bed.

If sliding at the bed occurs $V_{slip} \neq 0$. Internal deformation is often modelled with a linear profile (dashed line), granular-type profile (dashed-dotted line), half-parabolic profile (solid line) or a viscoplastic-type profile (dotted line). The latter is characterized by an unsheared surface layer.

Source: Kaitna, R. et al. (2014), p 378.

[18] Nagl, Georg et al. (2020), p. 1,2.

[19] Kaitna, R. et al. (2014), p. 378.

3.5 Rheological models

In this chapter, examples for rheological models used in simulation software are presented together with their parameters for the flow resistance term. For example, in the numerical simulation software DAN3D different types of resistance laws can be chosen, like laminar, turbulent, Bingham, frictional or Voellmy rheology.[20] In RAMMS DF, frictional behaviour is represented by the Voellmy model.[21] Only few of these models contain an additional parameter for the calculation of the basal shear stress, like i.e. the basal friction angle. In the following, three examples for commonly used models are given that include a separate parameter for the basal friction.

Frictional basal resistance: [22]

In this model, the basal shear stress is a function of the bed normal stress, the pore pressure at the base and a dynamic basal friction angle.

$$\tau_{zx} = -(\sigma_z - u) * \tan(\phi)$$

τ_{zx} ... *basal shear stress*

σ_z ... *bed normal stress*

u ... *porepressure at the base*

$\tan(\phi)$ ... *dynamic basal friction angle*

Voellmy resistance model: [23]

This model was introduced by Voellmy (1955) and includes the friction parameter f for the frictional term and ξ for the turbulent term.

$$\tau_{zx} = -(\sigma_z * f + \frac{\rho * g * v_x^2}{\xi})$$

f ... *friction coefficient analogous to* $\tan(\phi)$

ρ ... *density*

g ... acceleration due to gravity

v_x ... *velocity*

ξ ... turbulence parameter

20 Mcdougall, Scott (2006), p. 76.

21 WSL - Institut für Schnee- und Lawinenforschung SLF (2020) (see web sources).

22 Hungr, Oldrich and McDougall, Scott (2009), p. 983.

23 Ibid., p. 983.

Turbulent flow:

Turbulent flows of mixtures with low solid concentration are often analysed using the Manning's equation with the Manning's coefficient or the Chézy equation with the Chézy coefficient. The Manning's roughness or friction coefficient is an empirically derived coefficient. It depends on many factors, including the surface roughness, roughness due to bed-form and flow reach.[24] Manning also established a connection between his and the Chézy coefficient.

Manning's equation: [25]

$$\tau_{zx} = \frac{\rho * g * n^2 v_x^2}{R^{1/3}}$$

n … Manning's coefficient
R … hydraulic radius

Chézy equation: [26]

$$\tau_{zx} = \frac{\rho * g * v_x^2}{C^2}$$

C … Chézy coefficient

With a connection experimentally discovered by Manning between n and C: [27]

$$C = \frac{R^{1/6}}{n}$$

---

24 Calo, Victor M. et al. (2013), p. 2.

25 Hungr, Oldrich and McDougall, Scott (2009), p. 983.

26 Ibid., p. 983.

27 Limerinos, J.T. (1970), p. 8.

4 Methodology

To investigate the effect of the surface roughness on the velocity profiles and the runout lengths of gravitational mass movements, laboratory experiments in a small scale were carried out. The tested material and the inclination of the flume was the same in each experiment. Four different types of surface roughness were tested. To also get information about the influence of the relative roughness, experiments with three different starting volumes were undertaken. Each experiment was repeated three times. In total, 42 experiments were therefore carried out with 14 different variations.

Table 1: Overview of the experiments.

Experiment	Roughness	Volume
1_1 to 1_3	R1 = 2 mm	V1, M = 7.0 kg
1_4 to 1_6	R1 = 2 mm	V2, M = 3.5 kg
1_7 to 1_9	R1 = 2 mm	V3, M = 10.5 kg
1_10 to 1_12	R1W = 2 mm + sticks	V1, M = 7.0 kg
1_13 to 1_15	R1W = 2 mm + sticks	V2, M = 3.5 kg
2_1 to 2_3	R2 = 4 mm	V1, M = 7.0 kg
2_4 to 2_6	R2 = 4 mm	V2, M = 3.5 kg
2_7 to 2_9	R2 = 4 mm	V3, M = 10.5 kg
3_1 to 3_3	R3 = 6 mm	V1, M = 7.0 kg
3_4 to 3_6	R3 = 6 mm	V2, M = 3.5 kg
3_7 to 3_9	R3 = 6 mm	V3, M = 10.5 kg
0_1 to 0_3	R0 = 0 mm	V1, M = 7.0 kg
0_4 to 0_6	R0 = 0 mm	V2, M = 3.5 kg
0_7 to 0_9	R0 = 0 mm	V3, M = 10.5 kg

4.1 Experimental setup

For the experimental setup, a small chute out of acrylic glass, which has already been used for previous experiments at the laboratory of the Institute of Mountain Risk Engineering (IAN), was rebuilt and adapted to the new needs. The experimental setup can be seen in Figure 3 and a sketch with the dimensions in Figure 4.

Figure 3: Experimental setup.

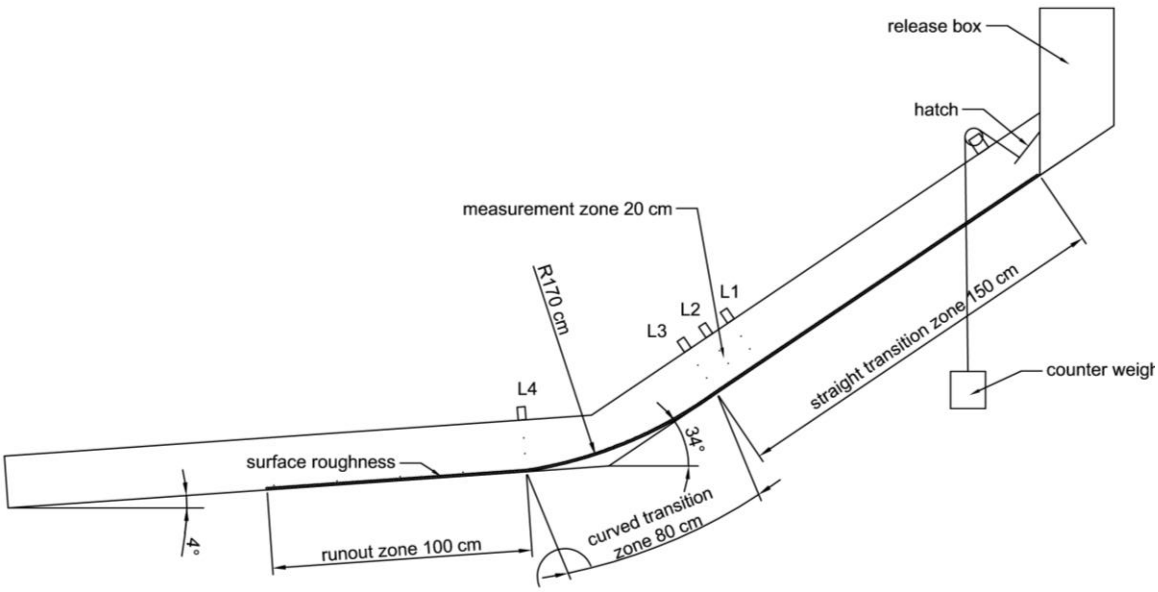

Figure 4: Sketch of the experimental setup.

It consists of a channel with a total length of four meters. A release box is at the top, a measurement zone in the middle and a runout zone in the end. The flume is 0.17 cm wide and has a fixed inclination of 34° for the first 1.5 m after the release box. The inclination of 34° has been chosen because on one hand, in test experiments a flow of the mass could also be achieved on the roughest surface and on the other hand, it was flat enough to do not get a continuous acceleration and thus a steady flow. Within the last 0.2 m of the 34° inclined transition zone and directly before the curved transition zone is the measurement zone. Then the 0.8 m long curved transition zone with a radius of 1.7 m follows. After the transition zone the flume ends in a 4° inclined runout zone. The rear side wall is out of acrylic glass in the upper part and out of wood in the lower part. The front side wall is out of acrylic glass along the whole length to be able to observe the flow behaviour. The experiments were designed as dam break experiments with a so-called hot start, which means that the initial condition for the necessary force imbalance for downslope motion is abruptly imposed.[28] Therefore, the tested material is accumulated behind a flap and released at once when opened. In dam break experiments, three different configurations for the release box are possible. A bed-normal dam with infinite rectangular reservoir upslope, a bed-normal dam with triangular finite reservoir upslope and a vertical dam with a finite triangular reservoir upslope.[29]

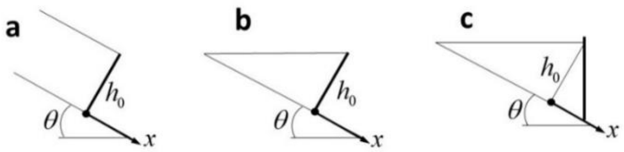

Figure 5: Types of release boxes.
(a) bed- normal dam with infinite, rectangular debris reservoir, (b) bed-normal dam with finite, triangular debris reservoir, (c) vertical dam with finite, triangular debris reservoir.
Source: Iverson and George, 2018, p. 4.

Since the inclination is constant for all configurations it was possible to adapt an existing reservoir with an opening mechanism for the hatch that has been proven in earlier experiments at the IAN. This reservoir is built in form of a vertical dam where a finite mass of granular material can be released. The release box itself is built out of 0.8 cm thick wood with inside dimensions of 0.285 m width, 0.645 m height and 0.145 cm depth and with a 0.125 m by 0.21 m gate. To ensure that the gate opens quickly and the same way in all experiments, an opening mechanism

28 Iverson, Richard M and George, David L (2018), p. 1.

29 Ibid., p. 4.

with a counterweight was implemented. Four different types of surface roughness, ranging from 0 mm to 6 mm height and additionally one macro roughness, which was higher than the maximum flow height, were tested. To build the three different types of rough surfaces, gravel was sieved out and glued with epoxy compound onto plastic plates. The working steps are shown in Figure 6 to Figure 9. The sieves had a mesh size of 1 mm, 2 mm, 4 mm, and 6.3 mm. Therefore, the sieved material for the roughness R1 ranges from ≥ 1 mm to < 2 mm, for the roughness R2 from ≥ 2 mm to < 4 mm and for the roughness R3 ≥ 4 mm to < 6.3 mm. These mesh sizes were chosen because the height of the produced roughness types is then approximately half the mean beat diameter of the tested material for R1, the mean beat diameter for R2 and one and a half of the mean beat diameters for R3. The smooth surface (R0) is the plastic plate without gravel glued on it. The additional macro roughness (RxW) was built out of wooden sticks with a diameter of 5 mm and can be adapted to each surface. Furthermore, it was divided into several individual elements to be able to change the covered area. Also, the wooden sticks were mounted in such a way that the number of sticks and therefore the number of obstacles can be varied easily. The finished surface roughness on the changeable plastic plates is shown in Figure 10 and the macro roughness, which can be adopted to each roughness type, is shown in Figure 11.

Figure 6: Woven wire mesh sieves 1 mm to 4 mm.

Figure 7: Epoxy resin with harder.

Figure 8: Smooth plastic plates (roughness R0).

Figure 9: Sieved material in the buckets and roughness R1 to R3 during curing.

Figure 10: From the left to the right: R3, R2, R1.

Figure 11: Additional macro roughness (R1W).

4.2 Tested material

The influence of pore pressure on the stress changes in soils is a complex process. For an easier understanding and better evaluation of the results, the experiments were undertaken only with dry granular material.[30] The tested material – the Denstone 2000 support balls - consisted of small ceramic beats with an average diameter of 2.8 mm to 4.3 mm. This material was chosen because in the laboratory of the Institute of Mountain Risk Engineering, previous experiments in a rotating drum were undertaken with the same material and therefore the results of the different experiments may be compared for further analysis. An example for the ceramic beats is shown in Figure 12 and the mean beat size and the bulk density are shown in Figure 13 according to the manufacturer's specifications.

Figure 12: Example of the Denstone 2000 support balls.

Source: Datasheet Denstone 2000 Support Balls ©2017 Saint-Gobain NorPro

Physical Properties

Nominal Size		Diameter (mm)		Crush Strength (lb)	Crush Strength (kg)	Crush Strength (N)
mm	in	min	max	min	min	min
3	1/8	2.8	4.3	50	22.7	223

Bulk Density* (kg/m³)		Bulk Density* (lb/ft³)	
min	max	min	max
1281	1378	80	86

Figure 13: Material parameters of the Denstone 2000 support balls.

Source: Datasheet Denstone 2000 Support Balls ©2017 Saint-Gobain NorPro

To also get information about the relative roughness, experiments with three different starting volumes were carried out. The smallest volume had a mass of 3.5 kg, the middle 7.0 kg and the largest volume had a mass of 10.5 kg. These volumes were chosen because first test experiments worked well with 7.0 kg, guaranteeing a release at once according to the height of the hatch. This is also the maximum mass for a triangular shaped reservoir due to the limited size of the release box, illustrated in Figure 14. Furthermore, it was assumed that too large starting volumes would falsify the results due to the limited size of the hatch of the release box. Hence, to get a sufficiently high difference in weight to detect relevant information on relative roughness and achieve equidistant spacing of the volumes, the 7.0 kg were multiplicated with 0.5 and 1.5 to

[30] Hungr, Oldrich (2008), p. 1157.

define the masses of the other volumes. The bulk density after a loose filling was calculated as approximately 850 kg/m3.

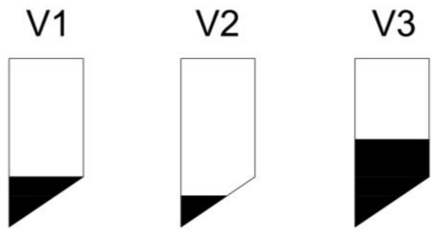

Figure 14: Sketch of the release box with V1, V2 and V3.

To determine the internal static friction angel a coniform pile was deposited on a horizontal plain for several times and of different sizes. The angle of response represents the internal friction angle. The mean angle measured was about 28°.[31] The dynamic internal friction angle is about 4° smaller than the angle of response in the internal static friction angle measurement.[32] To determine the bed friction angle, a small cylindrical container with a diameter of 10 cm was placed on the roughness and filled with the test material. The cylinder was lifted about half the ceramic beat size to make sure the cylinder does not get caught in the roughness. Then the roughness plate was tilted gently with a small agitation in form of a knock on the plate at each step until the cylinder moved down the inclined plate.[33] This worked well for the roughness R1. On the roughness R2 and R3, the cylinder toppled and therefore a measurement was not possible. In order to still have a reference value for the bed friction angle some material was placed on the roughness plate and the plate was tilted until the bottom layer moved down the incline, also with a small agitation each step. The measured bed friction angle for R1 was with both methods about 30°. With the latter mentioned method the bed friction angle for the roughness R2 was about 36° and for the roughness R3 about 39°.

4.3 Technique of measurement

Based on the runout parameters described in chapter 3.3 the runout lengths, flow velocities in the transition zone and flow heights were measured. The measuring instruments used were a ruler for the runout lengths, laser sensors for the flow heights and the mean front velocities and a high-speed camera to obtain information about the velocity profiles. To enable a comparison

31 Pudasaini, Shiva P. and Hutter, Kolumban (2007), p. 400.

32 Hunger, O and Morgenstern, N. R. (1984), p. 419.

33 Pudasaini, Shiva P. and Hutter, Kolumban (2007), p. 400.

of the laser data with the video recordings, the measurement starts of the laser sensors as well as the recording start of the camera were triggered. The trigger signal was sent as a 5 V DC voltage signal through a switch that was closed by opening the hatch.

4.3.1 Measurement of the runout lengths with a ruler

In order to measure the runout length in all experiments the same way, it was necessary to clearly define it first. Thus, the maximum reached distance was defined as where the tested material coated the surface continuously over the whole width of the flume. The distance to an imaginary line, which was at a right angle to the side wall, was measured with a ruler. To avoid the inaccuracies due to different deposit heights and the curved transition zone, the runout lengths were measured back from the end of the runout zone and then deducted from the total length as:

$$L = L_m - L_{max}$$

$L \dots Runout\ length$

$L_m \dots Measured\ length$

$L_{max} \dots Maximum\ length\ of\ the\ surface\ routhness\ plates\text{: } 3.3\ m$

An example is given in Figure 15.

Figure 15: Measuring of the runout length.

Also, the thickness of the deposition in the runout zone was measured. A laser sensor measured at one position and a ruler was used to measure in intervals of 10 cm.

4.3.2 Measurement of flow height and mean front velocity with laser sensors

The flow height is the normal depth of the flowing material measured perpendicularly to the bottom of the flume in contrast to the thickness which is measured vertically.[34] Flow heights were measured with laser sensors at four different positions along the channel: one in the runout zone and three in the measurement zone. All laser sensors were mounted in the centreline of the flume. The three laser sensors in the measurement zone, which is within the last 20 cm of the 34° inclined transition zone, were used to calculate the mean front velocity of the flowing mass in two cross sections via cross correlation of the laser signals. The position of the laser sensors is shown in Figure 16. The model of the laser sensor used is an OADM 20I6480/S14F of the company Baumer with a measuring range from 100 mm to 600 mm.

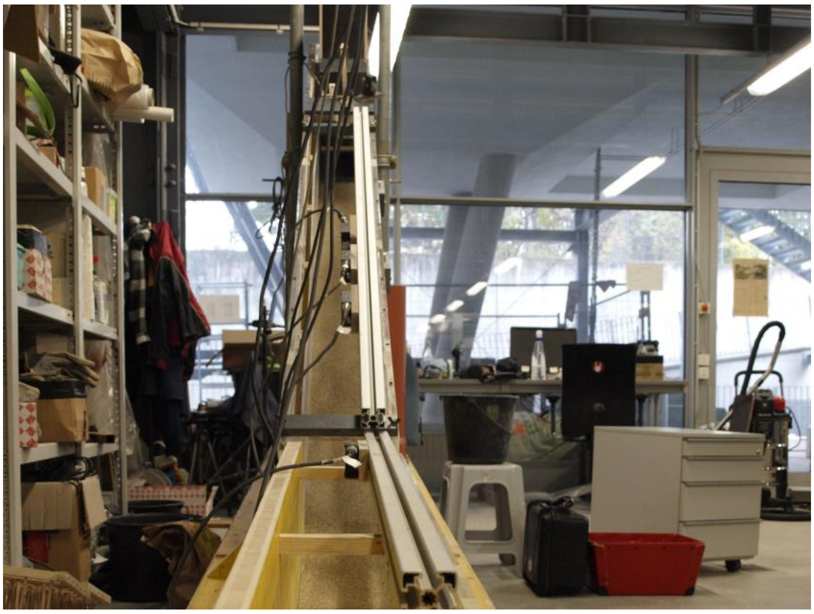

Figure 16: Position of the laser sensors.

The laser sensors were calibrated with three objects of known height in four steps. The steps were 0 mm, 20 mm, 30 mm and 90 mm. With these three objects, a measuring straight line with a linearity deviation between σ = 0.000099 and σ = 0.000140 could be achieved in a measuring range of slightly above 100 mm. The three objects and the calibration in the measurement software "catman" are shown in Figure 17.

[34] Dietrich, William E. et al. (2013), p. 111.

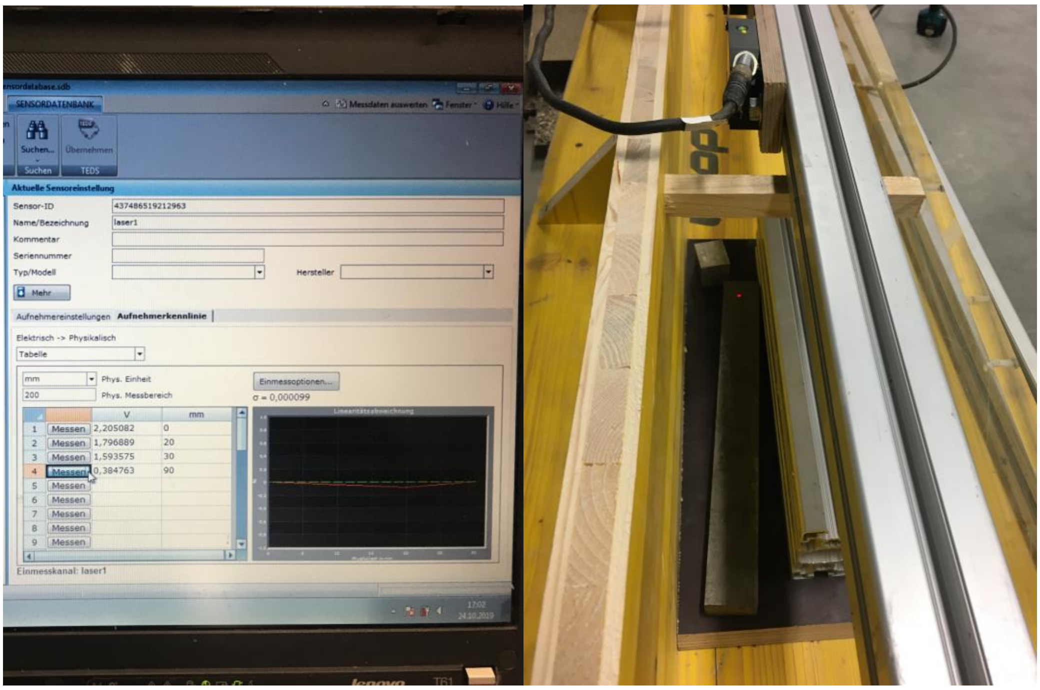

Figure 17: Calibration of the laser sensors.

The measuring frequency used was 2400 Hz. With this frequency the data volume was easy to manage and with this resolution the best results for the cross correlation were achieved. Since the surface roughness does not have the same height at every point all values are measured including the roughness, so the bottom of the flume is the lower end of the roughness. Therefore, the laser sensors were zeroed to the bottom of the surface roughness at each change of the setup, i.e. the surface of the plastic plate. That means, for the real flow height the roughness height must be subtracted. For better understanding, this is shown as a sketch in Figure 18.

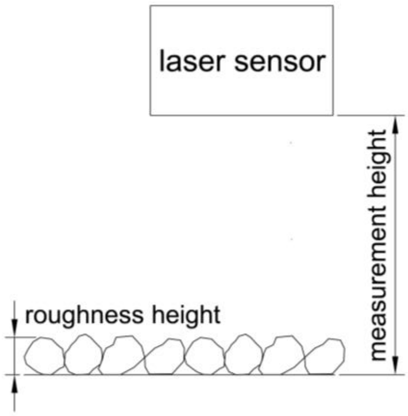

Figure 18: Measured height.

4.3.3 High-speed recordings for the extraction of velocity profiles

To get information about the velocity profiles the experiments were recorded with a high-speed camera CR3000x2 of the company Optronis throughout the transparent side wall. Since this chute was already in use for previous experiments the acrylic glass had many scratches. To guarantee a good image quality it was necessary to polish the glass. This was done with the SONAX scratch remover paste. Now to the technical features of the camera: with a resolution of 1280 by 720 pixel a frame with the size of 20 cm length and 11 cm height could be observed. At this resolution, it was possible to record 1618 images per second and the internal memory of the high-speed camera allowed a recording time of 11.5 seconds. With the chosen frame rate of 1500 images per second and the usage of 75% of the recording memory a recording time of approximately 9 seconds, and therefore the whole flow from release to deposition, could be recorded. Since the reached velocities in the channel were relatively high, the exposure time of the camera had to be set to 1/4000 seconds to get clear and not blurred recordings. To be able to close the aperture as much as possible and thus obtain an image with adequate depth of field, and because of the short exposure time, a very strong illumination was needed. Therefore, a LED light with 1200 lumen was installed. Moreover, the high-speed camera was set up in an angle of 34° to obtain horizontal images. An illustration of the camera setup is shown in Figure 19.

Figure 19: Camera setup with the high-speed camera Optronis CR3000x2 and the illumination Gs Vitec MULTILED QT 12.000 Lm white.

To facilitate the handling of the large amounts of data, the relevant part of the video, i.e. from the arrival of the front in the measurement zone to the end of the tail of the granular avalanche or the last depositions, was cut and saved with the corresponding camera software "TimeBench" after each experiment. For further evaluation, videos in avi format and pictures in bmp format, both in 8-bit and grayscale, were exported with the corresponding camera software. With this setup, high quality pictures with a good image resolution as well as temporal resolution were achieved. An example is shown in Figure 20. The used lens was a NIKON AF Nikkor 35 mm f/2. This lens has a focus length of 35 mm and the angle of view is 62°.

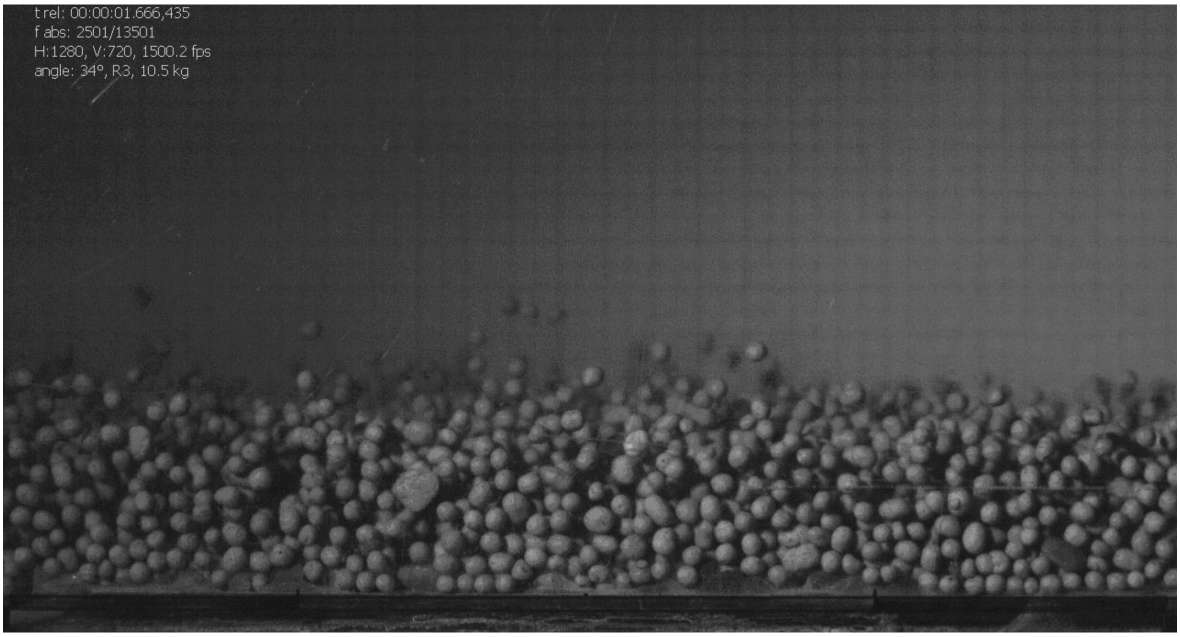

Figure 20: Example picture of the high-speed recordings.

4.4 Experimental procedure

The experiments started with the first roughness out of five. Therefore, the plastic plates with the first roughness (R1) were inserted into the channel and the laser sensors were zeroed to the surface of the plastic plate. In total, five different experimental setups were introduced. All five experimental roughness configurations were tested with three different volumes except R1W. All experiments were repeated three times with each volume. An overview of the different setups can be found in Table 1.

For each experiment the same procedure was applied as follows: at first, the surface was cleaned with a vacuum cleaner and the part of the transparent side wall, throughout which the recordings were done, was cleaned. Then the hatch of the reservoir on the top was closed and fixed with a small flap. The test material was weighed exactly and filled into the reservoir loosely and not compressed. After this, the measurement units for the laser sensors and the high-speed camera were started. The small flap, which held the reservoir hatch closed, was opened manually and at the same time the trigger signal for the measurement recording was sent through a pressure switch. The measurement stopped automatically for the camera when the recording memory was full and for the laser sensors after 10 seconds. Afterwards, photos were taken to document the experiment and the runout length was measured manually with a ruler. Meanwhile, the video recordings and the measurement job of the laser sensors were saved.

4.5 Evaluation

This chapter aims to explain how the recorded data was evaluated. Furthermore, it is described which tools were used for this purpose and which assumptions were made.

4.5.1 Evaluation of the runout lengths

The runout length was measured for each repetition of each experimental setup with its varying starting volumes. Then, the mean value of all three repetitions per experiment was calculated with:

$$L_m = \frac{1}{n} \sum_{n}^{1} L_n$$

$$L_m \ldots Mean\ runout\ length$$

$$n \ldots Number\ of\ repetitions$$

$$L_n \ldots Runout\ lenght\ of\ each\ repetition$$

Hence, it was possible to get information on which boundary condition had the biggest effect on the runout length.

4.5.2 Evaluation of the laser data

Four laser sensors were installed along the channel. Three of them were positioned in the measurement zone and one in the runout zone. To analyse the collected data and handle the many data points with a recording frequency of 2400 Hz, the numerical computing software MATLAB was used. For this purpose, an existing script[35] has been used but amended and extended to fully serve the needs. All four laser sensors were used to obtain information about the flow height over time. For better visualization, the laser signals were smoothed. Then, the laser signals were plotted to get a diagram of the flow height over time of the whole granular mass avalanche. The smoothed laser signal was only used for the diagrams where the measured flow

35 Provided by Roland Kaitna.

heights of all four laser sensors over time were plotted. All further calculations have been done with the raw laser data. Additionally, three of the laser sensors were used to calculate the mean front velocity. Therefore, the cross-correlation function measured the displacement of the two laser signals and thus the lag. With the lag difference and the sampling frequency the time difference of the laser signals could be calculated. With the time difference and the known distance between the laser sensors the velocity was calculated as follows:

$$\Delta t = \frac{lag}{Fs}$$

$$v = \frac{d}{\Delta t}$$

$\Delta t \ldots Time\ difference$
$Fs \ldots Sampling\ frequency$
$d \ldots Distance\ between\ laser\ sensors$
$v \ldots Mean\ velocity\ between\ laser\ sensors$

Apart from this, the first sighting of the experiments showed that there is no dense flow from the front to the tail. Therefore, the laser data was used to find out the range where a dense flow prevails. As the sampling frequency of 2400 Hz generates many measuring points, the laser data was down sampled to 600 Hz for better visualization. Only the laser data of laser two was used for this task because on this position the velocity profiles were extracted. The diagram, which is shown in Figure 21, was created for each experiment to determine the best sequence for analysis. The red lines show the lower and the upper boundary of the chosen time span. Because the front of the flow reached the measurement zone in each experiment from R1 to R3 approximately at the same time, and to make the individual experiments comparable, in each experiment the same range was chosen for analysis. In the experiments with roughness R0 and R1W, another time span was chosen because the mean flow velocity was much faster for the first and much slower for the latter. In the experiments with the smallest starting volume, no dense flow could be detected, but more about that in the chapter Results.

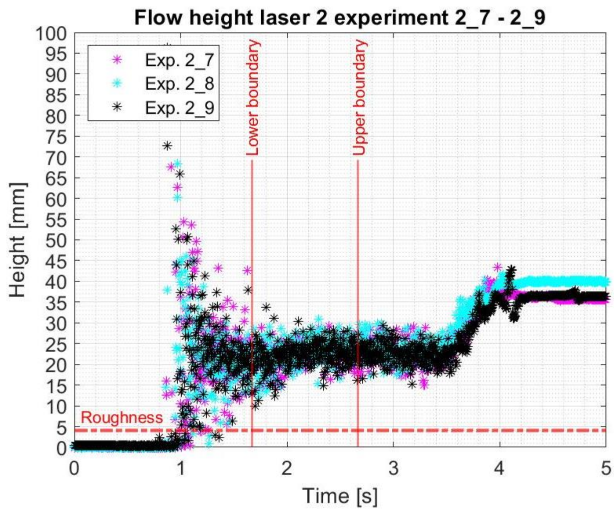

Figure 21: Example of the flow height over time with the biggest volume V3.

Also, in the part of the dense flow, the measured flow heights strongly fluctuate. This may have several reasons. One reason may be that even with a statically flowing body individual grains are distributed on the surface so that an uneven surface occurs. Or, especially on the rougher surfaces, grains are flying in the air due to a collision with other beats, especially within the loosened up flowing front. Moreover, the flowing mass can be divided into a solid layer on the bottom, a liquid layer with a dense flow and a gaseous layer with a dilute flow on the top.[36] This gaseous layer with bouncing beats makes it difficult to measure the flow height accurately. As the measuring range of the laser sensor begins at 100 mm distance from the sensor, it gives unusable values if a ceramic beat gets to close. If this happens, the values are negative or unrealistically high. Therefore, all values below 0 mm and above 100 mm were filtered out. Another reason may be that the laser sensor collects data 2400 times a second. That means that the entire grain is scanned which leads, by a mean beat diameter of 4 mm, to an additional variation of at least 2 mm. As seen in the scatter plot in Figure 21, the measured flow heights scatter in a range of 10 mm even when a dense flow dominates. Hence, the calculated mean flow height did not match the observed flow heights. Consequently, the 0.9 percentile was chosen as the flow height since in comparison with the recorded videos, this value fitted best for all experiments. In Figure 22 a boxplot of the measured flow heights is shown. In this boxplot, the red line is the median and the box is confined with upper limit as 0.75 percentile and the lower limit as 0.25 percentile.

[36] Forterre, Yoël and Pouliquen, Olivier (2008), p. 3.

The whisker length is +/- $2.7*\sigma$. The upper limit for the outliers is defined as $q3 + w \times (q3 - q1)$ and the lower limit as $q1 - w \times (q3 - q1)$.[37] The green crosses are the 0.9 percentile.
It is important to note that the values in the boxplots of the flow height were measured from the surface of the plastic plate for a more accurate measurement, i.e. for the real flow height the roughness height must be subtracted.

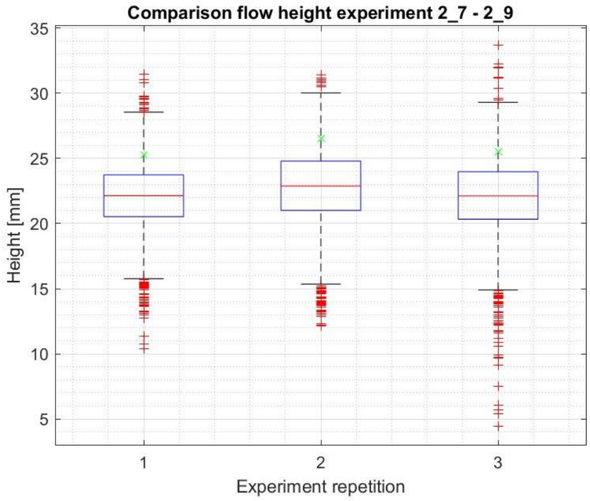

Figure 22: Boxplots of measured flow height in the three repetitions.

4.5.3 Evaluation of the high-speed recordings

In order to obtain more information about the vertical velocity distribution over the entire flow height, the high-speed recordings were evaluated. For this purpose, the MATLAB app PIVlab was used. PIVlab is a graphical user-interface based software programmed in MATLAB. It uses the digital particle image velocimetry (DPIV) technique for analysis and visualization of flows. The analysis process can be divided into three steps. The steps are image pre-processing, image evaluation and post-processing.[38] First of all, for the data input the high-speed recordings were exported from the recording software as single pictures in bmp format with 8-bit in greyscale. When importing the images, the sequencing style can either be selected from image 1-2, 3-4 etc. or 1-2, 2-3, 3-4 etc. For the analysis in this study the latter was used. Subsequently, a region of interest, i.e. the area that shall be analysed, can be selected. After that the image pre-processing can be started. For this step some pre-processing techniques are available with already predefined settings. For all analyses only the contrast limited adaptive histogram equalization

37 MathWorks (2020) (see web sources).

38 Thielicke, William and Stamhuis, Eize J. (2014), p. 1.

(CLAHE) option was used, which enhances the contrast of the image and sufficiently improved the pictures to lead to good results. In the next step, the PIV settings can be selected. Two approaches can be chosen here. The first is direct cross correlation (DCC) and the second is discrete Fourier transform (DFT), which uses a fast Fourier transform. The DCC approach creates more accurate results but has the disadvantage of a higher computational time. The DFT approach is much faster and the lower accuracy can be compensated by running several passes of DFT on the same dataset.[39] Thus, the DFT approach with three passes was chosen. Pass one, with an interrogation area of 64 times 64 pixel, pass two with 32 times 32 pixel, and pass three with 16 times 16 pixel. The interrogation areas overlapped each other by 50%. This size of the interrogation areas was chosen because in the third pass the size of the area is than approximately two thirds of the mean ceramic beat diameter and thus a good compromise between required computing time and high resolution. With these settings a computational time of about 25 minutes for each experiment was achieved with the available hardware. In Figure 23 an example is given how an analysed image pair with the calculated velocity vectors looks like. The distance between the vectors is about 2.5 millimetres.

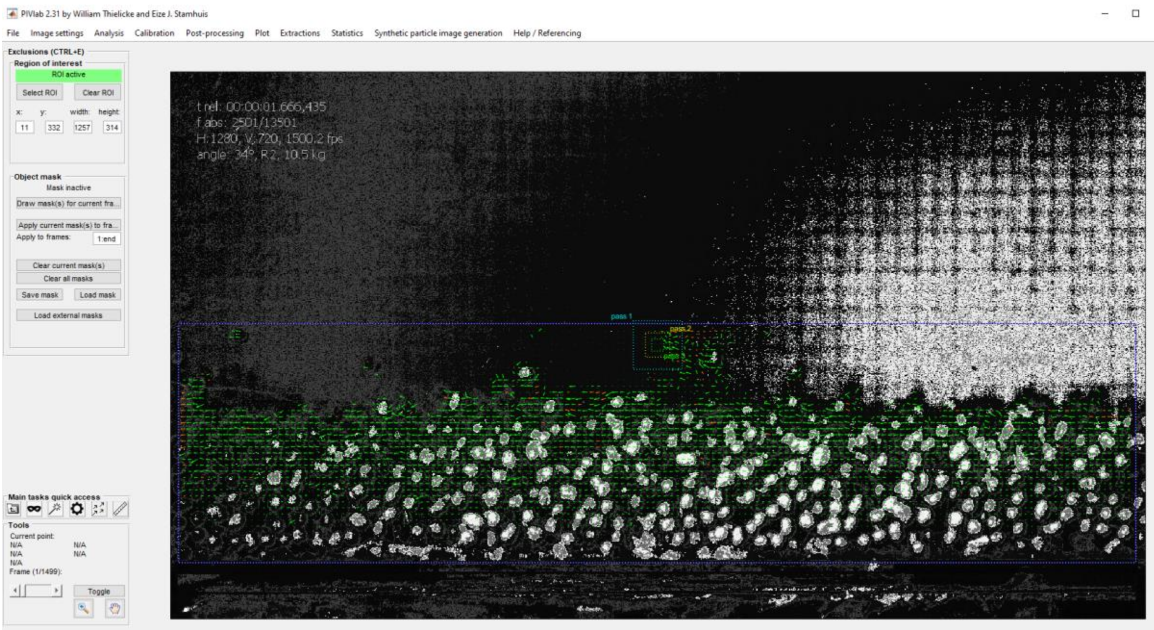

Figure 23: Result of an analysed image pair in PIVlab.

39 Ibid., p. 3.

After the analysis of the images, the calculated velocity vectors had to be calibrated. Therefore, it was important to take a picture of a reference grid with known size after each new installation of the camera. In this image, a reference distance of known size was chosen and with the known time difference between the images enough information was available to calibrate the velocity vectors.

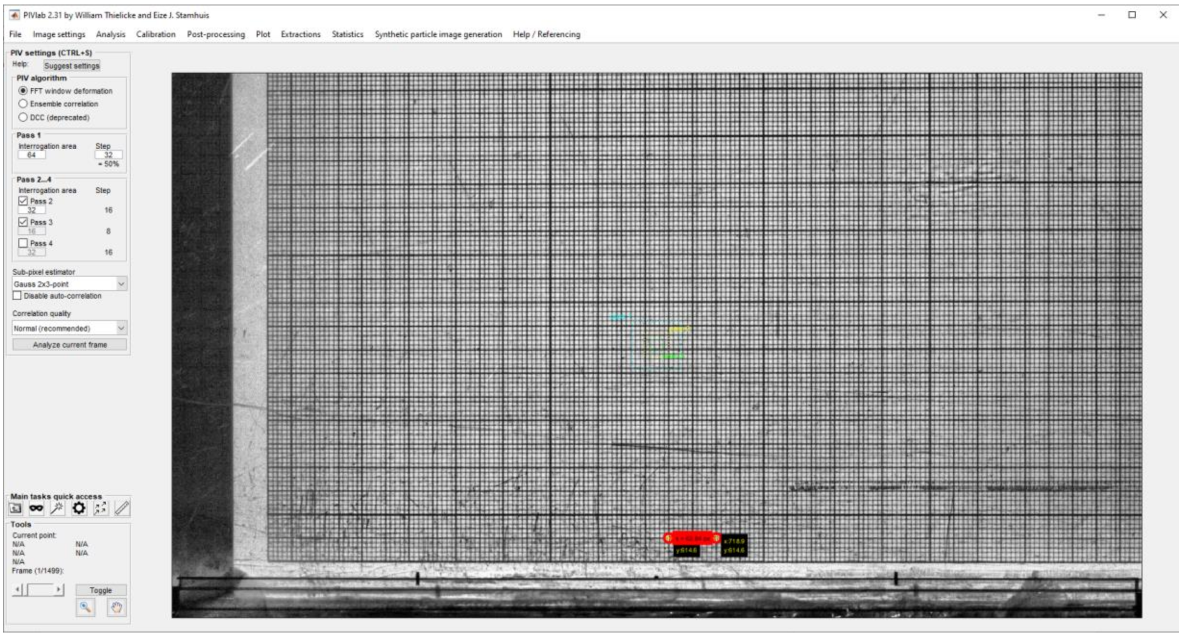

Figure 24: Calibration of the velocity vectors.

Afterwards the second step, namely the post-processing, was conducted. For this purpose, limits of acceptable velocities were defined to filter the outliers. For the velocities in x-direction the upper limit was chosen with the assumption that the particles cannot be faster than in free fall of the height difference which corresponds to about 4 m/s. The lower limit was set with minus 2 m/s. The limits for the velocities in y-direction were set at plus 2 m/s and minus 2 m/s. These limits covered most of the velocity points in the scatter plot and only filtered the outliers with unrealistic values. An example for the scatter plot can be seen in the following Figure 25. The deleted vectors were replaced by interpolated ones.

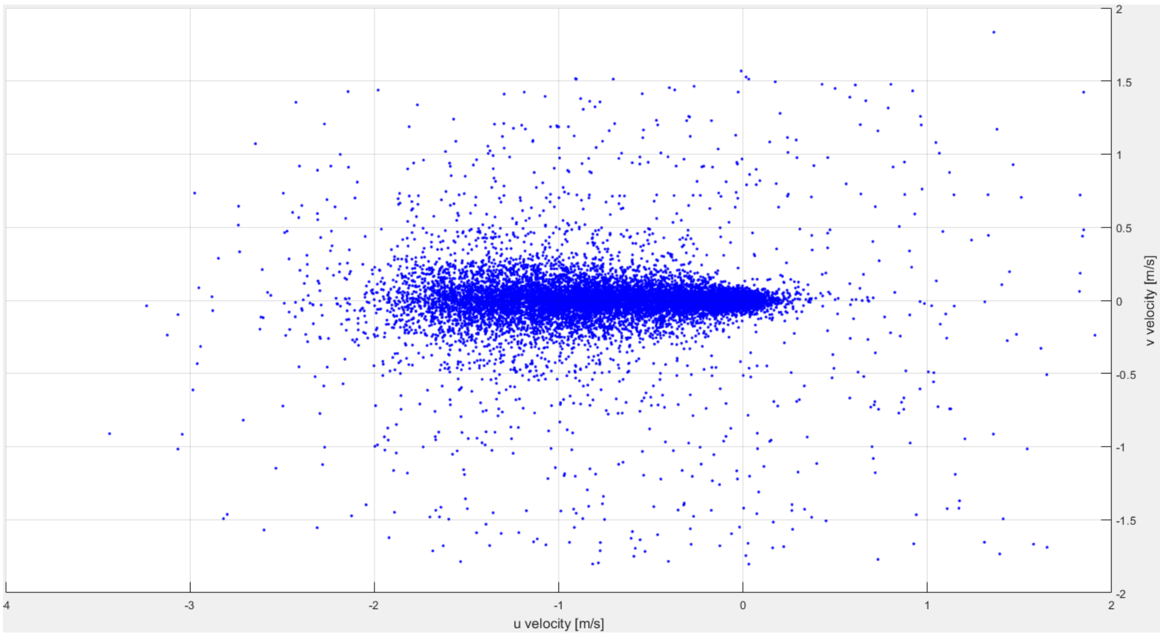

Figure 25: Scatter plot of u- and v-velocities.

After the post-processing was done, the velocities in x-direction had to be extracted for each time step. For the analysis in this study only the velocities in x-direction, i.e. in the direction of flow, are investigated. The position of the extracted velocities was chosen in the middle of the recorded frame. In this position, the laser sensor L2 was located and could be used to get the flow heights. Velocities were extracted from the bottom of the surface roughness, which corresponds to the zero point of the laser sensors, up to a height of 5 centimetres. To get velocity values in a sufficiently high resolution for further evaluation, 1000 velocity values were extracted on this line of 5 centimetres. Thus, a resolution for velocity values in steps of 0.05 millimetres of the flow height was achieved. As mentioned before, velocity values each 2.5 millimetres were calculated, which means that all values between are interpolated velocity values. The extracted velocity values with heights were stored in a text file. In order to be able to further process these, the program MATLAB was used again. Here, it must be noted that a correct naming of the text files is very important. The PIVlab app named the text files when exporting with numbers from one to one thousand five hundred. To import the text files in the correct order in MATLAB the numbering must have the same number of digits. Therefore, it was necessary to rename the text files. For example, because 1500 has four digits, profile_1 had to be renamed to profile_0001. For importing the renamed text files in MATLAB, a pre-programmed script[40] was used. This script was again adapted and further extended to be able to carry out all necessary analyses. For each experiment, all 1500 velocity profiles were imported to MATLAB and stored

40 Provided by Roland Kaitna.

in a three-dimensional array for further processing. In the first step, the profiles were cut at the mean flow depth that means at the 0.9 percentile of the measured height from laser sensor L2. Because the region of interest for the PIV analysis ended exactly at the bottom of the surface roughness, no velocity values were available for the last 2.5 millimetres. This is due to the overlapping of the interrogation areas of 50%. Although this was within the surface roughness, the values of the last 2.5 millimetres were interpolated to obtain velocity information from zero to the maximum flow height. To get information on how the velocity profiles changed with time, the profiles were separated in time steps of 0.2 seconds. In the following, a median profile for the total analysed time span of one second and for each time step of 0.2 seconds was calculated as well as the standard deviation. The median was chosen because it is less sensitive to possible outliers than the mean value.[41] With a plot of the median profile and the standard deviation, as can be seen in Figure 26, the three repetitions could be compared whether they are alike, which is shown in Figure 27.

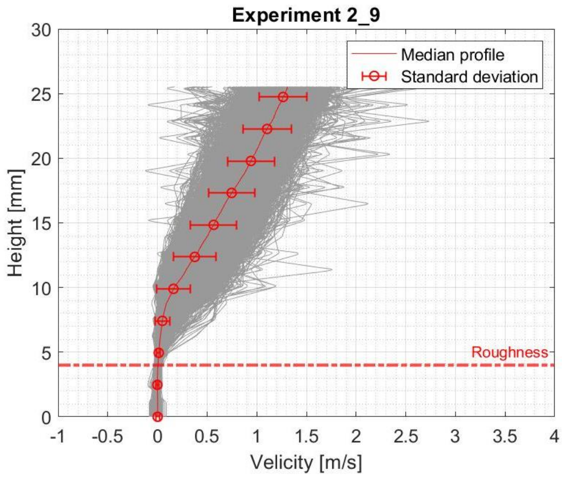

Figure 26: Example for a median profile with standard deviation.

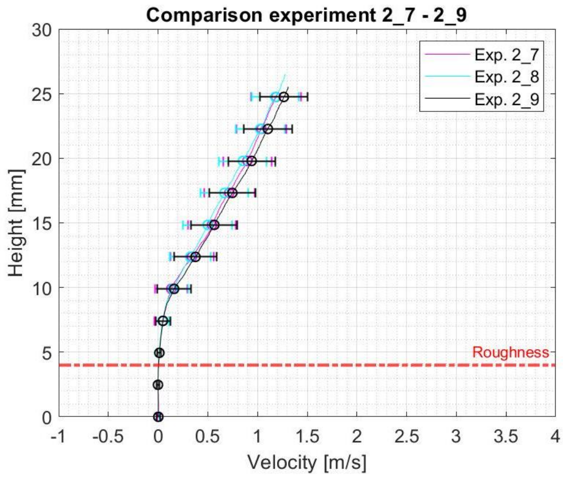

Figure 27: Comparison of the repetitions.

The median profiles of the single time steps like in Figure 28, were used to determine in which period the profiles change the least.

[41] Marinell, Gerhard and Steckel-Berger, Gabriele (2008), p. 33.

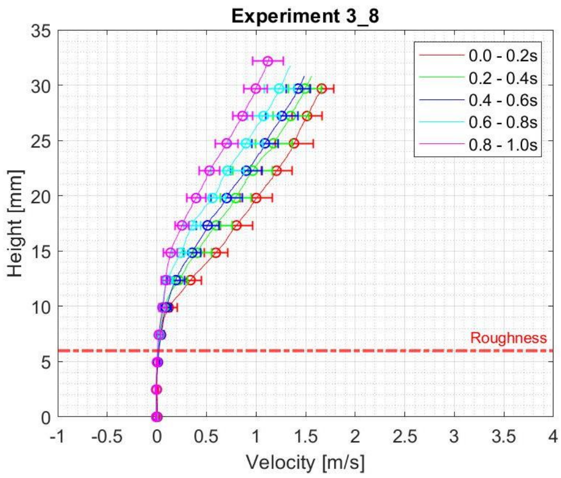

Figure 28: Median profiles for time steps of 0.2 seconds.

This time segment was then used to compare all experiments with each other. In all experiments, the time segment from 0.2 seconds to 0.6 seconds had the most similar profiles. Thus, it could be assumed that this time segment is within the body of the granular avalanche and is most suitable for comparison. Moreover, the slip velocity and the mean velocity for each experiment were calculated from the data obtained via the video analysis. Since the grain size used was between 2.8 and 4.3 millimetres, the slip velocity was defined as the mean velocity between the roughness height and the roughness height plus the mean ceramic beat diameter. For all comparisons of the different setups, the results of the three repetitions were averaged.

5 Results

In this chapter, the results of the evaluation of the laboratory experiments are presented and described. The chapter is divided into three subchapters – one for each research question mentioned at the beginning of this master's thesis.

5.1 The change in runout lengths

Regarding the runout lengths, a clear trend has been identified: for all starting volumes, the runout lengths decreased the higher the surface roughness got (Figure 29). A clear trend could also be seen regarding the starting volume. The higher the starting volume, the longer was the runout length. Here, it is very interesting that the influence of the surface roughness is higher than the influence of the starting volume with the starting volume V1 with a mass of 7 kg and V2 with a mass of 3.5 kg. But with the largest starting volume V3 with a mass of 10.5 kg the pattern changed. The difference in runout lengths between the different types of surface roughness decreased and between the two roughest surfaces the influence of the starting volume is even bigger than the influence of the roughness height. This suggests that the momentum strongly affects the runout length.[42] Furthermore, in the six experiments undertaken with the macro roughness, the runout lengths remained constant with varying starting volumes. It can be assumed that this is due to the fact that the macro roughness limited the discharge. Therefore, the starting volume no longer made a difference if the material could be deposited in the transition zone. Figure 30 and Figure 31 show that the deposition heights on the macro roughness were much higher with larger starting volume but the runout lengths were the same.

42 de Haas, Tjalling et al. (2015), p. 18.

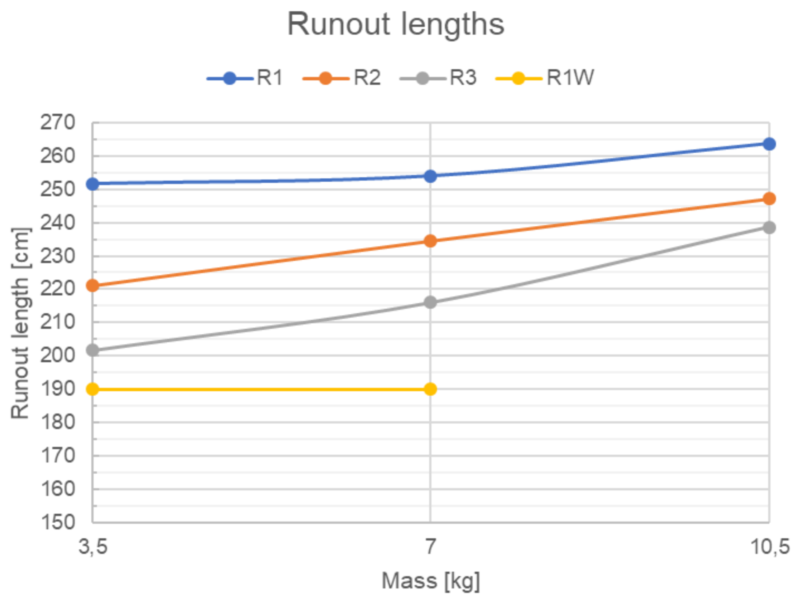

Figure 29: Change of the runout lengths on different roughness variations with different starting volumes. (R1 roughness height 2 mm, R2 4 mm, R3 6 mm, R1W 2 mm with additional macro roughness)

Figure 30: Deposition height on the macro roughness with the starting volume with a mass of 7.0 kg.

Figure 31: Deposition height on the macro roughness with the starting volume with a mass of 3.5 kg.

The following illustrations from Figure 32 to Figure 37 show that the longitudinal profiles of the depositions differed between R1 and R2, but were almost the same between R2 and R3. On the roughness R1, the depositions were much higher but less spread out. On the roughness R2 and R3, the depositions were flatter but extended. The different shape of the depositions may be attributed to the instant deposition of material during the flow on the rougher surfaces.[43] Moreover, on the roughest surface, the depositions in the transition zone were approximately 6 mm higher than on the roughness R2 in the experiments with starting volumes with a mass of 7.0 kg and 10.5 kg. This may be one reason for the shorter runout lengths with increasing roughness.

43 Cheng, Yung Ming et al. (2019), p. 192.

Figure 32: Deposition R1, V1.

Figure 33: Deposition R1, V3.

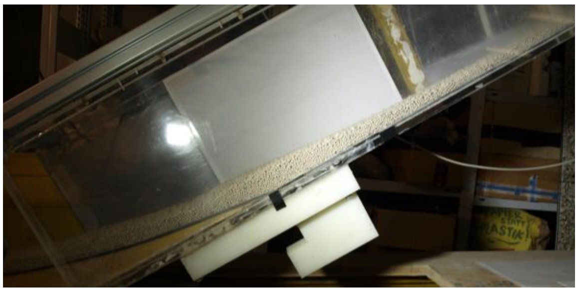

Figure 34: Deposition R2, V1.

Figure 35: Deposition R2, V3.

Figure 36: Deposition R3, V1.

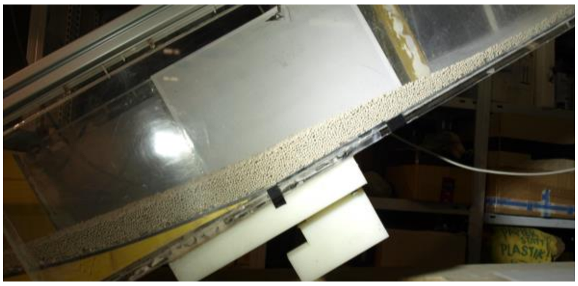

Figure 37: Deposition R3, V3.

5.2 The change in flow velocities

In the following it is explained how the velocities on the bottom of the flume, i.e. the slip velocities, and the mean velocities, calculated with the high-speed recordings, changed with the different setups. Furthermore, the front velocities, calculated with the data obtained from the laser sensors, are discussed. Also, the velocity profiles, which were extracted from the high-speed recordings, are shown.

5.2.1 The change in slip velocities and mean velocities

In the first section it is shown how the different types of surface roughness affected the slip velocity over the analysed time span of one second. Then, the effect of the starting volume is shown and at least the change of the mean velocity for each setup will be presented.

Regarding the different types of surface roughness, the results for the smooth surface R0 showed no change with time in the slip velocity - differing from the surface roughness R1 to R3 where obvious changes were detected. The highest slip velocity occurred on the smooth roughness R0. If you only consider the rough surfaces R1 to R3 an interesting point is that in all experiments the highest slip velocity occurred on the 2 mm roughness R1 and the lowest slip velocity on the 4 mm roughness R2. The highest surface roughness R3, with a height of 6 mm, was in between. This may have been due to the instant deposition of single ceramic beats in the distances between the roughness elements on the roughest surface, which effectively led to a lower roughness height. This statement is illustrated in Figure 38 and is also supported by the video recordings where this effect has been observed.

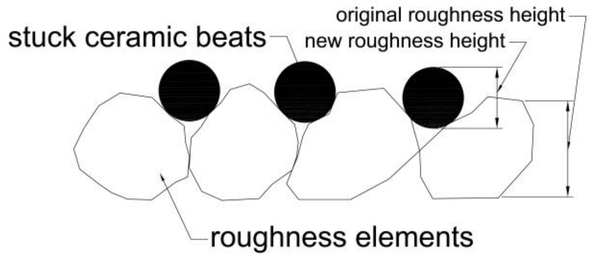

Figure 38: Sketch of decreased roughness due to stuck ceramic beats.

On the roughness R1 with the starting volumes V1 and V2, as well as on the roughness R2 and R3 with the starting volumes V1 and V3, the slip velocity had the highest value in the beginning, then had a steady phase and decreased to the end of the flow. The contrary was observed on the roughness R1 with the starting volume V3 and the roughness R3 with the starting volume V2, where the slip velocity increased again in the end of the analysed time span. As it can be seen in Figure 39 to Figure 41, it should be noted that only two out of nine setups showed this development. With reference to Schaefer and Bugnion (2013) it can be assumed that the slip velocity decreases with time[44], since this pattern has also predominated the experiments of this master's thesis. The slip velocity on the macro roughness R1W is shown separately in Figure 42 because it is another type of roughness. Also here, a decrease with time was detected. It should be noted that in this case the values of the slip velocity must be judged with caution since, due to the limited discharge, it has been more a flow of individual grains than a flow of a mass. Also, the flow height was only about three times the particle size.

44 Schaefer, Marius and Bugnion, Louis (2013), p. 7.

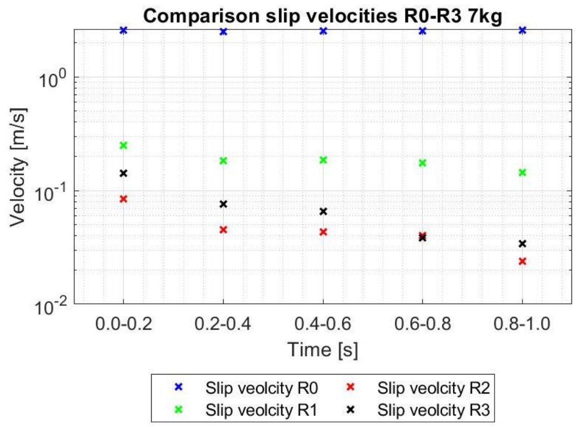

Figure 39: Slip velocities on roughness R0 to R3 with starting volume V1.

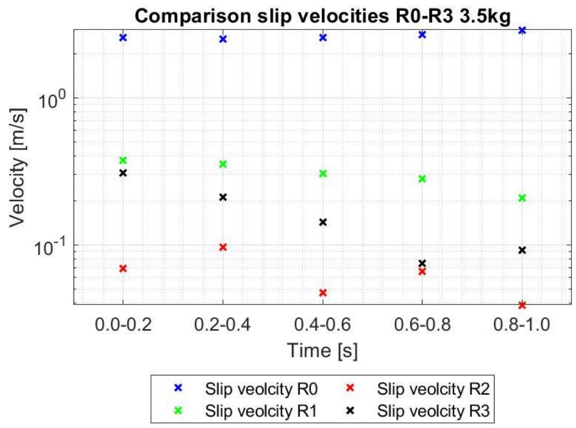

Figure 40: Slip velocities on roughness R0 to R3 with starting volume V2.

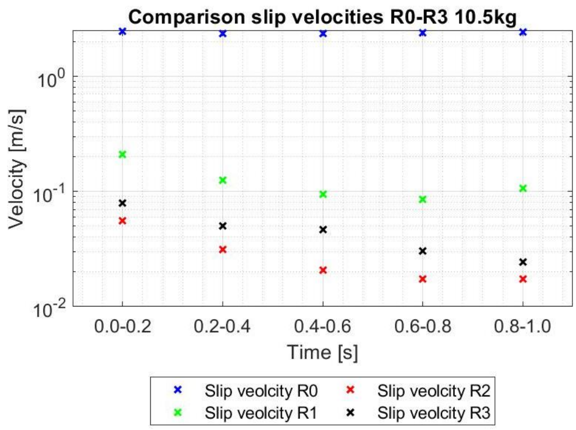

Figure 41: Slip velocities on roughness R0 to R3 with starting volume V3.

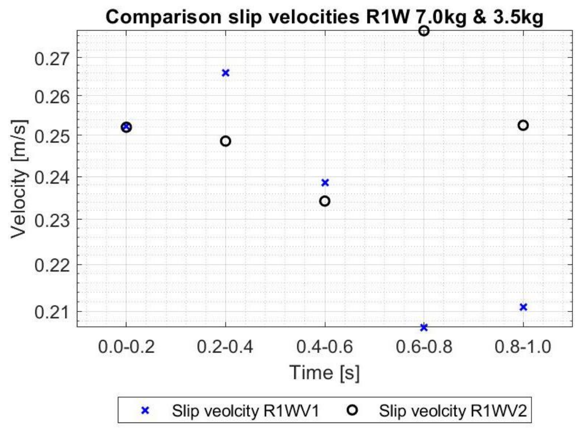

Figure 42: Slip velocities on the roughness R1W with the starting volume V1 and V2.

Regarding the starting volume, it can be said that the higher the starting volume, the lower the slip velocity. One reason for this may have been the higher load on the bottom layer and the therefore increasing friction, explained by the Coulomb friction for the basal shear stress which is dependent on the normal force and therefore the height of the overburden layer.[45] The fact that in all experiments the lowest velocities occurred with the largest starting volume underlines this statement. A good example of this are the experiments on the smooth roughness R0. If you take a look at Figure 43 in combination with the flow heights in Figure 67, it can be seen that the flow height corresponds to the value of the slip velocity, i.e. the higher the flow height was, the lower was the slip velocity. The following diagrams also show that in most of the experiments with a surface roughness > 0, the slip velocity decreased with time as described above. This also corresponds to the velocity profiles where the velocity over the height decreased with time, as could be seen in Figure 28 in chapter 4.5.3.

45 Popov, Valentin L. (2010), p. 134.

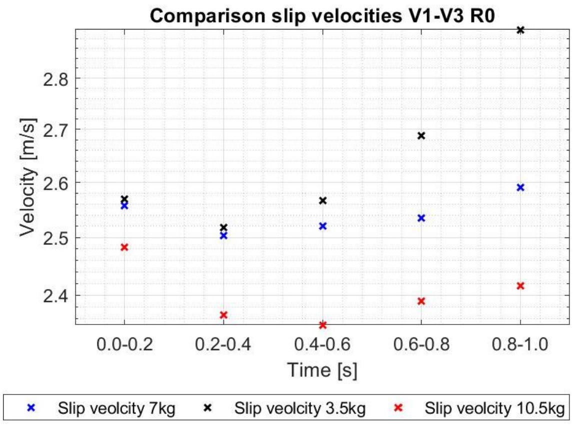

Figure 43: Slip velocities regarding the starting volume on the roughness R0.

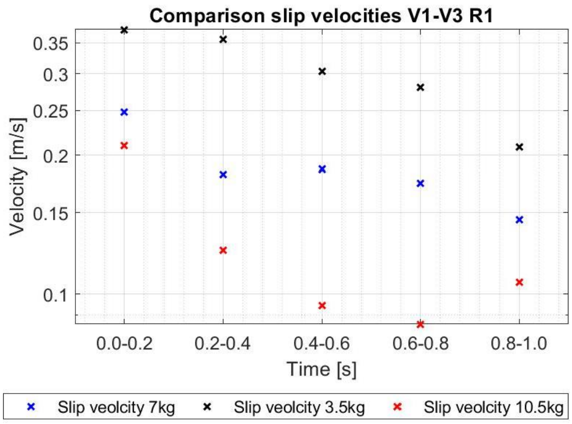

Figure 44: Slip velocities regarding the starting volume on the roughness R1.

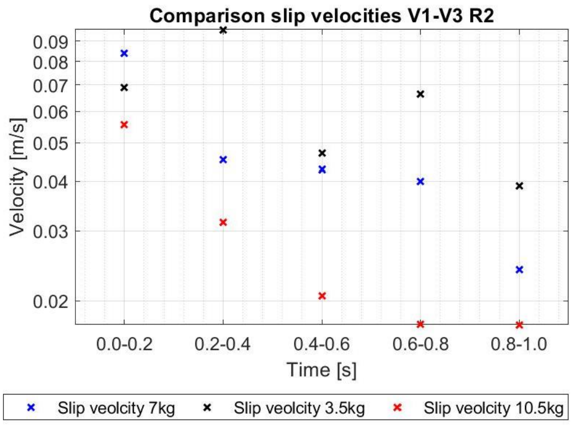

Figure 45: Slip velocities regarding the starting volume on the roughness R2.

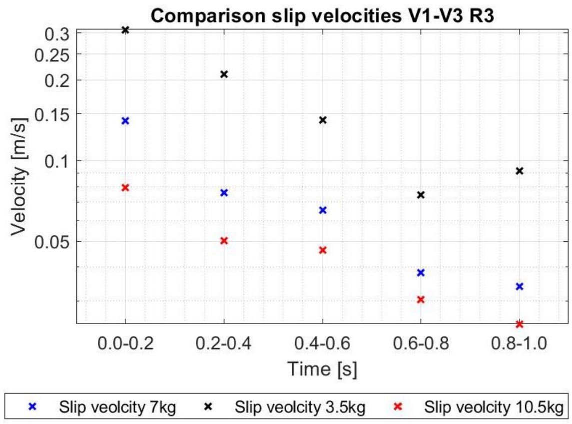

Figure 46: Slip velocities regarding the starting volume on the roughness R3.

The change in mean velocities for the different setups can be seen in Figure 47. The mean velocities on the smooth surface did not change with the starting volume V1 and V2 and were only marginally lower with the starting volume V3. It can be assumed that this is because of the lower slip velocity due to the higher load on the surface. For the roughness R1, the mean velocities with the starting volume V1 were marginally lower compared to the starting volume V3. The same pattern was observed in the experiments with the surface roughness R3. Only in the experiments with the surface roughness R2 the mean velocities decreased marginally with higher starting volume. The mean velocity with the starting volume V2 was much higher because there was no dense flow and the flow was more influenced by particle collisions than by friction on the ground. This could also be seen in the form of the velocity profiles which changed from a linear to a parabolic shape. Also, on the roughness R2 and R3, the mean velocities were the highest with the starting volume V2. Although the profiles here were s-shaped, the shape above the inflection point was again parabolic. Summarising, it can be said that the mean velocity decreased significantly from the experiments with a smooth surface to the experiments with a rough surface, but did not change a lot, or even stayed constant, between the two roughest surfaces. With changing starting volume, a significant difference could only be detected when the flow behaviour changed from a dense to a loose flow. In case of a dense flow the mean velocities were significantly lower than on the same roughness with a loose flow, but this pattern diminished with increasing roughness height. The smallest mean velocities were detected on the macro roughness R1W. On all roughness types, the mean velocity increased only marginally with larger starting volumes or even decreased in the experiments on the roughness R2.

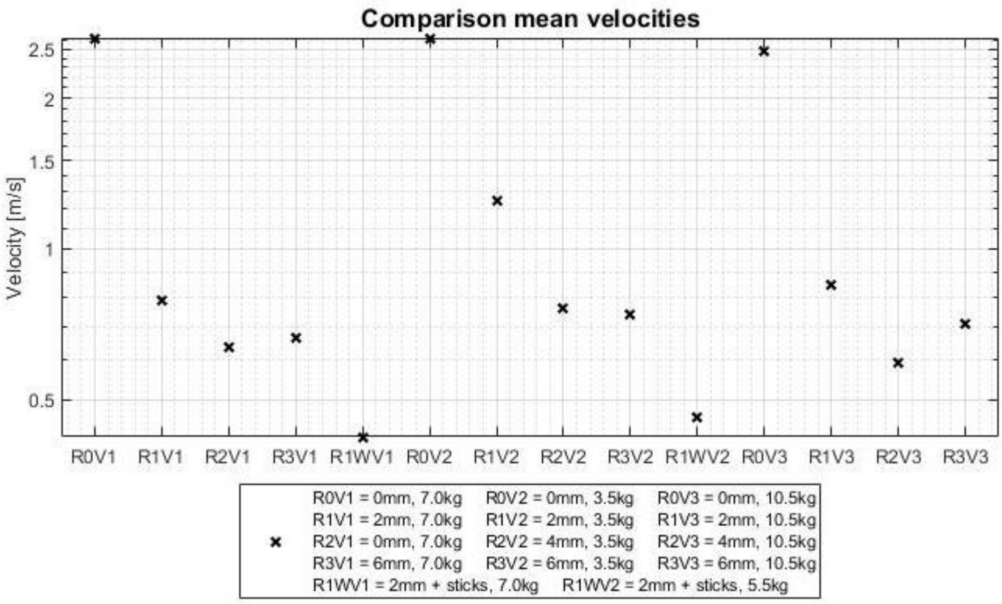

Figure 47: Mean velocities on the different setups.

Due to the before mentioned loose flow, especially in the front, there were also problems with the calculation of the average front velocity between the laser sensors L1, L2 and L3. The low bulk density made it difficult to distinguish the front of the avalanche from single grains that run ahead, leading to large deviations and in some cases even to unrealistic results. On the macro roughness R1W, laser sensor L2 was directly behind a stick and therefore provided unusable data, so that no calculation was possible. As it can be seen in Figure 48, it worked well in the experiments with the smooth surface roughness R0. These experiments have also been used to reference the calculated maximum velocities for the video analysis with PIVlab. In the experiments with the surface roughness R1, R2 and R3, the results were so widely scattered that it was hardly possible to draw conclusions about the actual velocities. However, except of some outliers, especially on the smoother surfaces, the computed values provide data to validate the video analyses.

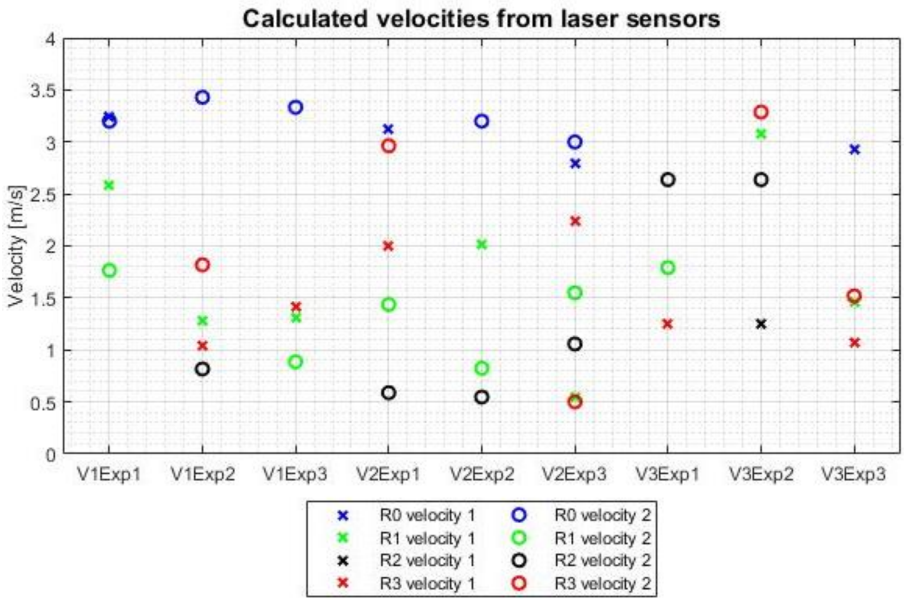

Figure 48: Front velocities calculated from the data obtained by the laser sensors.

5.2.2 The change in velocity profiles

This chapter takes a closer look at the velocity profiles and how they have changed in relation to the changed boundary conditions. In the first section, the effect of variation of the surface roughness is considered as it can be seen in Figure 49 to Figure 51. In the second section, emphasis is given to the variations of the starting volumes, which are represented in Figure 52 to Figure 55. On the smooth surface roughness, the velocities on the bottom of the flume were only slightly lower as on the top. This shows that there was practically no resistance on the flume bottom and therefore hardly any shearing within the flowing mass. The whole mass was gliding as a block on the bottom of the flume because the internal friction due the contact between the grains was higher than the basal friction and the avalanche existed out of only one quasistatic layer.[46] For the surface roughness R1, a linear or concave-up profile, depending on the starting volume, from the bottom to the maximum flow height could be observed. On the surface roughness R1, only with the biggest starting volume V3 an s-shaped velocity profile and therefore an inflection point started to develop. Only on the surface roughness R2 and R3, so on the two roughest surfaces, the velocity profiles were clearly s-shaped and therefore an inflection point could be observed well. After the inflection point, the velocity profiles continued with the same linear or concave-up shape as on the smoother surface roughness R1. This shows that the maximum shear rate occurs inside the flowing mass where a transition from the concave

46 Schneider, D. et al. (2011), p. 76.

to the convex shape occurs.[47] The ceramic beats close to the base slid with a very low slip velocity on the surface roughness, as described in the previous chapter, and the rest of the bottom layer showed a convex shape until the inflection point. This was also observed in the visual evaluation of the high-speed recordings. The maximum velocities were the highest in all experiments with the smooth surface. Between the different roughness types, the highest velocities occurred on the roughness R1, followed by the roughest surface R3. The lowest velocities were observed with the surface roughness R2. This is interesting because also due to the shorter runout lengths, the lowest velocities were expected on the roughest surface.

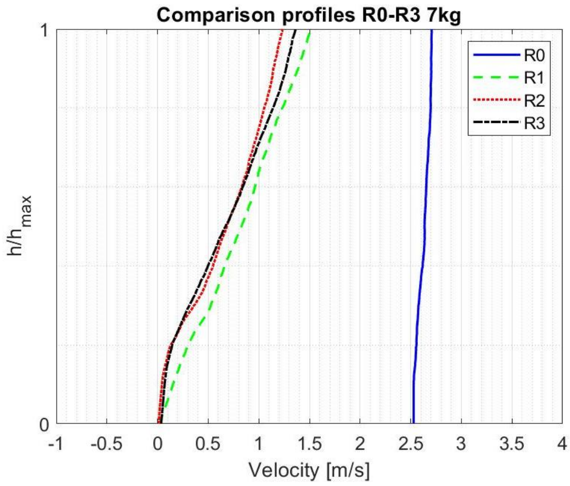

Figure 49: Velocity profiles R0 to R3 with starting volume V1.

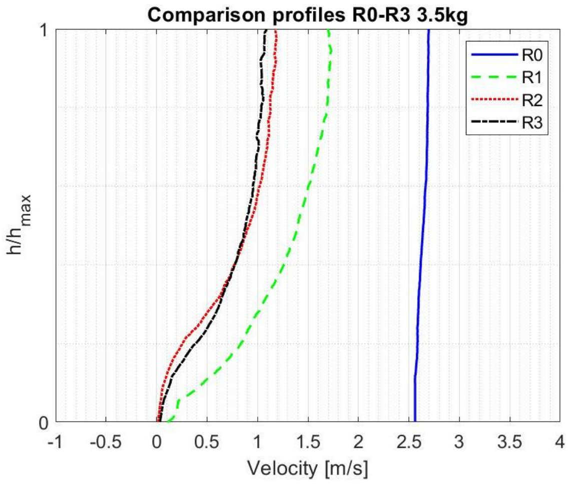

Figure 50: Velocity profiles R0 to R3 with starting volume V2.

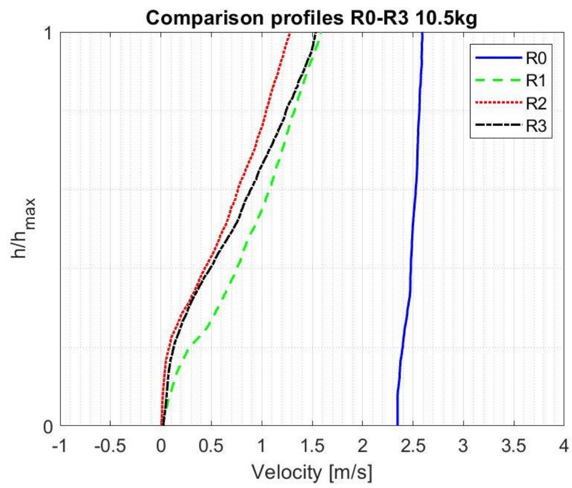

Figure 51: Velocity profiles R0 to R3 with starting volume V3.

47 Armanini, Aronne et al. (2005), p. 290.

Regarding the starting volumes, it is interesting that for the surface roughness R0, the velocities with the biggest volume were slightly slower than with the starting volume V1 and V2 where they were the same. As mentioned earlier, this may have been due to the higher load on the bottom and the therefore increasing friction. For the surface roughness R1 to R3, the shape of the velocity profiles changed with the smallest starting volume V2. With the starting volumes V1 and V3, the velocity profiles were s-shaped or linear, while the velocities increased in the experiments with the starting volume V2 parabolically with height. This was due to the loose flow which was probably dominated by collisions of individual particles. Interesting here is, that for the roughness R1 the velocity profiles with starting volume V1 were linear and no inflection point could be observed. With the starting volume V3 an inflection point occurred. This indicates that with the starting volume V1 the shear rate was constant over the whole depth of the flowing mass and with the starting volume V3 a maximal shear rate occurred inside the flow. Further, it can be assumed that the bigger starting volume led to a higher friction on the flume bottom and so a quasistatic layer on the bottom and a dense flow layer on the top were formed. In Schaefer et al. (2010) it is also mentioned that the inflection point follows the flow depth and therefore a critical value of overburden pressure is suggested.[48] As the flow height was only approximately 3 mm higher and the inflection point was less significant than for the rougher surfaces it is assumed that this critical overburden pressure has just been reached. On the other hand, on the two roughest surfaces an inflection point occurred with all three staring volumes. This indicates that a high load is not obligatory, but rather a sufficiently high friction drag on the flume bottom leads to the formation of an inflection point.

In Figure 52 to Figure 55 it can be seen that the higher starting volume led to slightly higher maximum speeds, except on the surface roughness R0 where the maximum velocity was lower with the largest starting volume V3. The higher maximum velocities fit to the observed longer runout distances with bigger starting volume. However, it must be noted that the runout lengths are clearly different, and the velocity profiles differ only minimally. Furthermore, the runout length for the 6 mm roughness R3 is significantly shorter than for the 4 mm roughness R2, despite faster velocities with the roughest surface R3. Therefore, it is supposed that, in addition to the before discussed change of velocity profiles due to different types of roughness and starting volumes, the runout length is influenced by a complex interplay of these boundary conditions and several more mechanisms like deposition or internal energy dissipation due to particle friction and particle collisions[49].

---

48 Schaefer, Marius et al. (2010), p. 4.

49 cf. Iverson, Richard M. (1997).

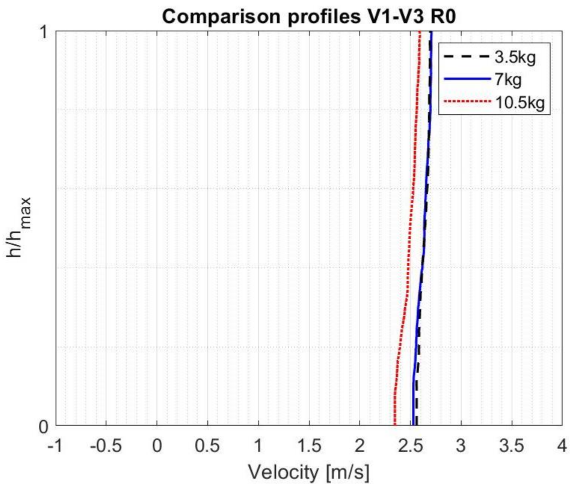

Figure 52: Velocity profiles V1 to V3 on surface roughness R0.

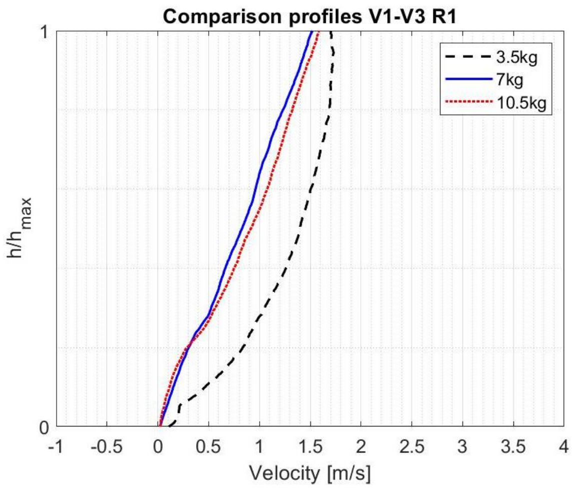

Figure 53: Velocity profiles V1 to V3 on surface roughness R1.

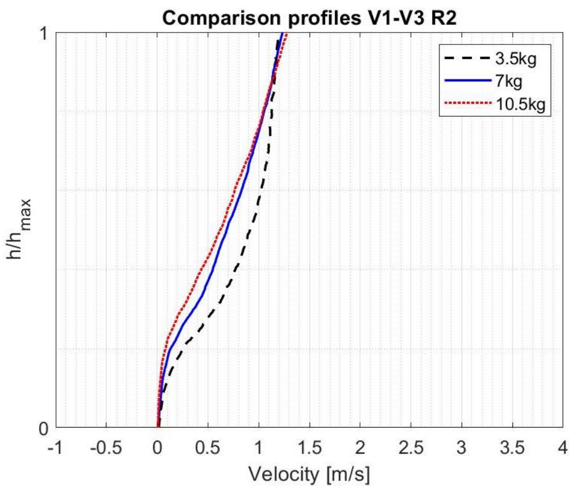

Figure 54: Velocity profiles V1 to V3 on surface roughness R2.

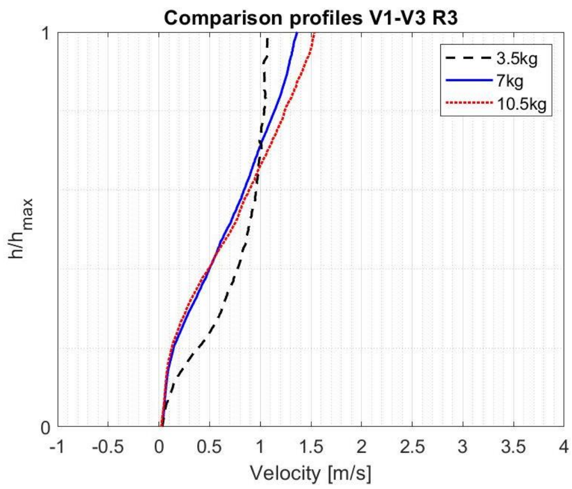

Figure 55: Velocity profiles V1 to V3 on surface roughness R3.

When analysing the change in the velocity profiles over time, the following is noticeable: on the smooth roughness, nothing changed in the time span of the analysed section. For the roughness R1, the flow slowed down for the first 0.4 seconds and then stayed rather constant for the next 0.6 seconds, while the flow height decreased. On the surface roughness R2 and R3 the flow slowed down continuously over the whole analysed second and the flow heights decreased with starting volume V1 and increased with starting V3. The behaviour of increasing flow heights in the analysed period could only be observed in the experiments with the biggest starting volume. In all other experiments the velocities as well as the flow heights decreased over time. This suggests that the analysed time span in the experiments with different volumes might represent different parts of the flow. An example for this phenomenon is given in the following Figure 56 and Figure 57.

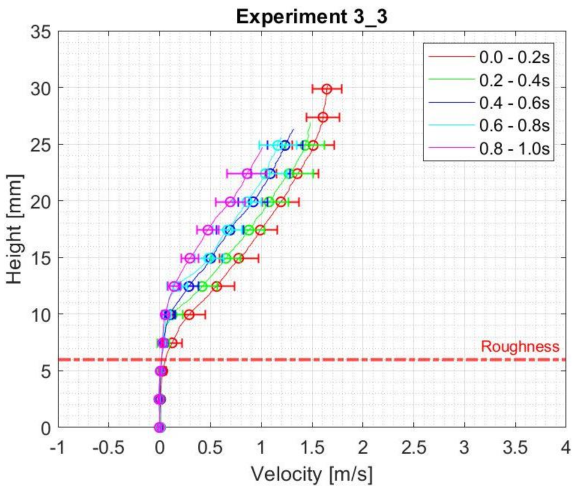

Figure 56: Velocity profiles over time for roughness R2 and starting volume V1.

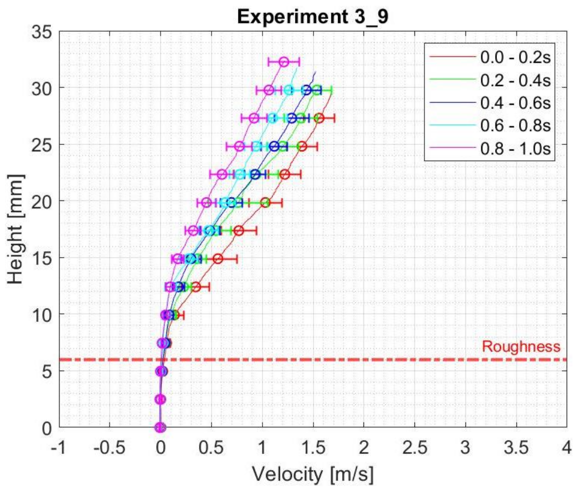

Figure 57: Velocity profiles over time for roughness R2 and starting volume V3.

The results of the macro roughness are shown separately as it is a different form of roughness. As mentioned in the previous chapter, not only the runout lengths remained the same with different starting volumes but also the velocity profiles did not change. As it can be seen in Figure 58, they had the same shape, which confirms the statement of limited discharge in the previous chapter.

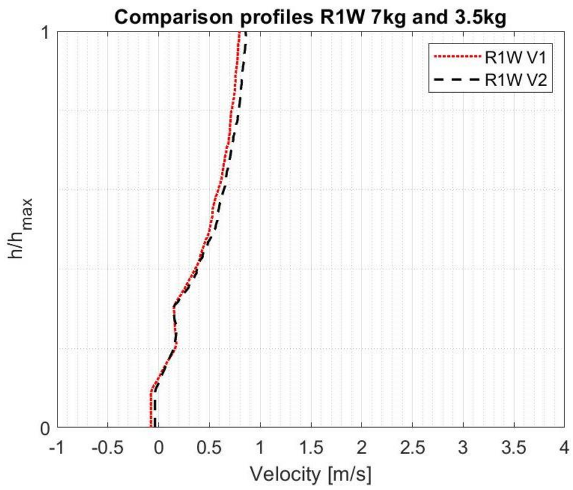

Figure 58: Velocity profiles of the experiments with the macro roughness R1W and starting volumes with a mass of 7.0 kg and 3.5 kg.

5.3 The change in flow heights

In this subchapter it is explained how the flow heights changed regarding the varying boundary conditions. A closer look was taken at the change over the whole avalanche as well as the change in the measurement section where the high-speed recordings were analysed.

5.3.1 The change in flow heights of the entire avalanche

In the diagrams of the measured flow height over time, the same pattern emerged for roughness R1, R2 and R3 with the starting volumes V1 and V3. The flow front exhibits the highest flow height and a small density by volume with single particles flying in the air. Then the flow height decreased, and a visually assessed dense flow set in. Towards the tail of the granular avalanche, the density again loosened up and the flow height increased until it decreased steadily. It is most clearly seen in the experiments with highest starting volume (Figure 59). In contrast Figure 60 plots the experiments with the smallest volume of 3.5 kilograms can be seen. There, a dense flow never set in (Figure 62). Hence, the flow height had its maximum in the front and then decreased steadily. In the experiments with the roughness R0, the maximum flow height was detected shortly after the front arrived and then it decreased steadily.

What can also be seen in the following diagrams is that the higher the roughness, the more of the material was deposited in the curved transition zone. This resulted in the fact that the deposition height, measured by laser sensor L4 in the runout zone, was higher in the cases with smaller roughness height. For example, the experiments with the roughness R0 and the starting volume V3 had the highest measured deposition height, as exhibited in Figure 61. For the macro roughness R1W the smallest flow height was detected. It increased shortly until the front passed and then stayed constant until the deposition started. The flowing material never reached the runout zone.

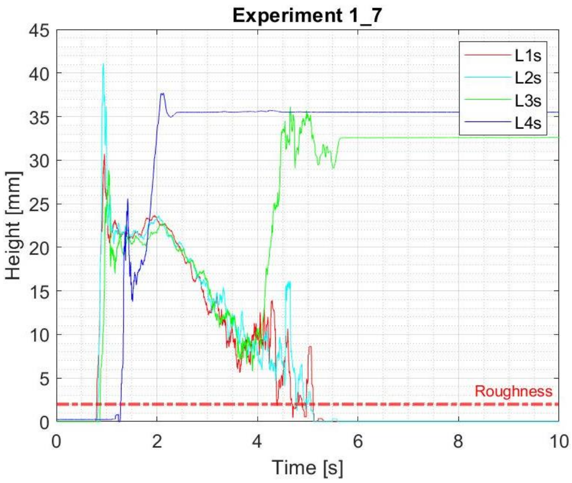

Figure 59: Plot of the smoothed flow height over time. (R1, V1)

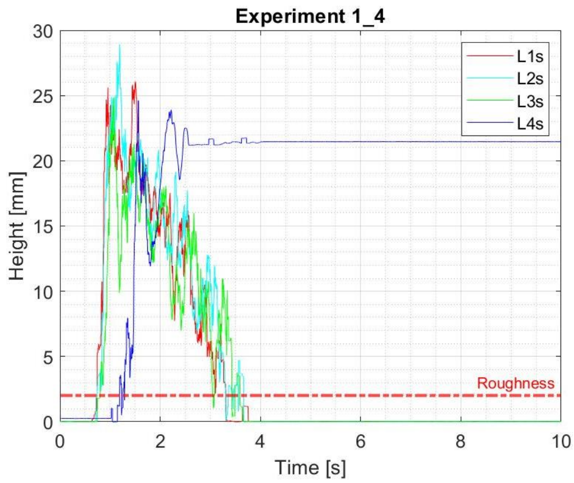

Figure 60: Plot of the smoothed flow height over time. (R1, V2)

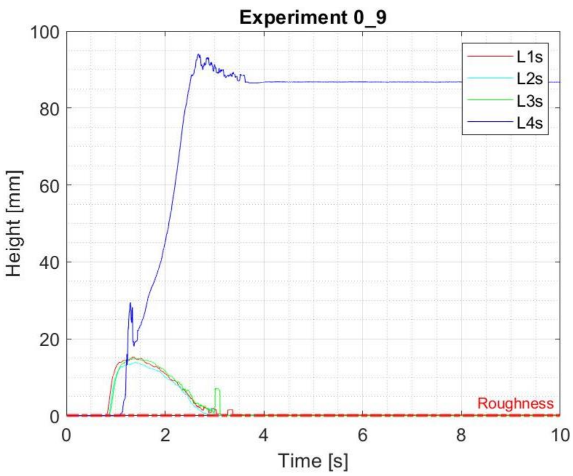

Figure 61: Plot of the smoothed flow height over time. (R0, V3)

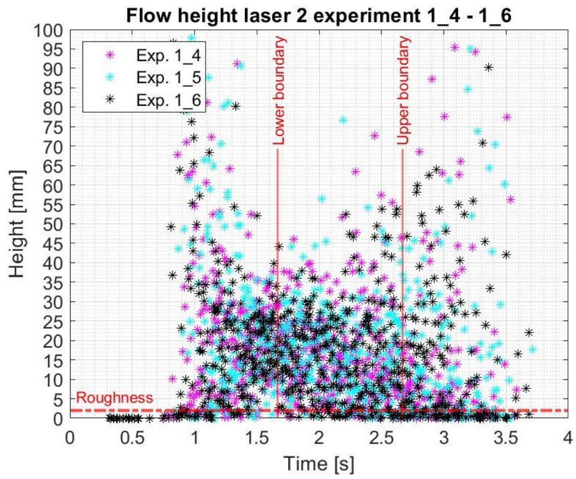

Figure 62: Plot of the measured flow heights over time. (R1, V2)

5.3.2 The change in flow heights within the analysed period

Regarding the starting volume, clear statements can only be made for the starting volumes where a dense flow could be observed, so in the experiments with volume V1 and V3. There it can be said that the flow height increased with larger starting volume. As mentioned before, in the experiments with V2 a dense flow was never observed. Due to the loose flow the flow heights were visually the highest in the high-speed recordings. The values of the 0.9 percentile of the measured flow heights in the experiments with the smallest starting volume were approximately the same as with the biggest starting volume on R2 and R3 and even the highest on R1. However, it must be considered that the measurement inaccuracies are the greatest in the experiments with the smallest starting volume. As the flow was very loose and the laser sensor could not detect a continuous surface, the flow height fluctuated between zero and about 40 millimetres. A comparison of the flow heights can be seen in Figure 63 to Figure 65, using roughness R3 as an example. Therefore, any interpretation of these measurement results should be treated with caution.

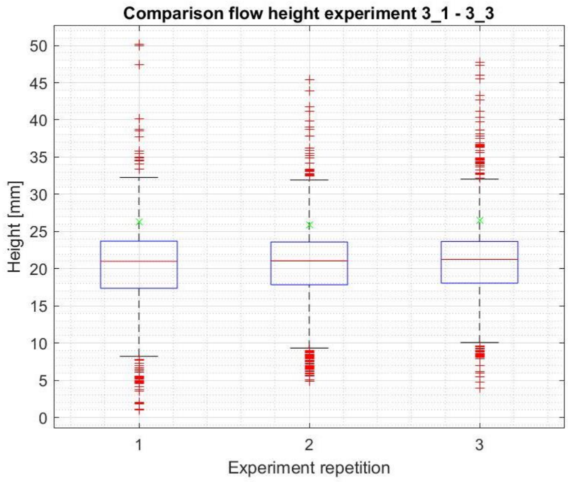

Figure 63: Boxplot of the flow height in the analysed period. (R3, V1)

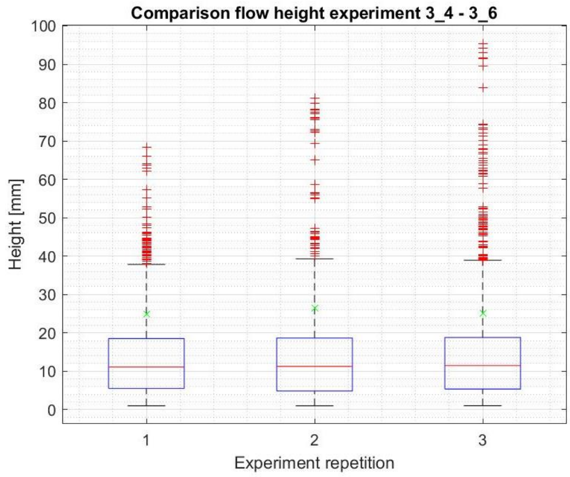

Figure 64: Boxplot of the flow height in the analysed period. (R3, V2)

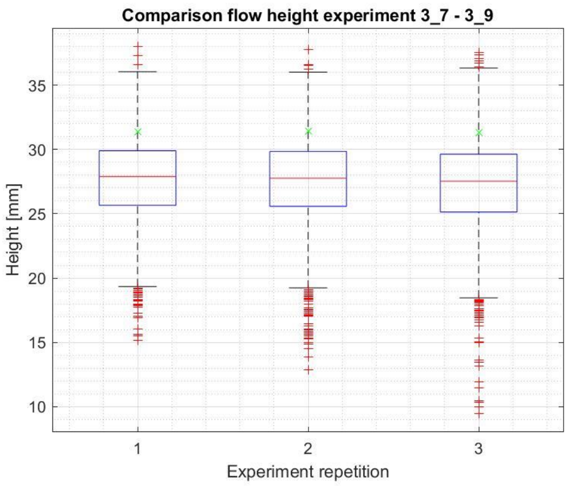

Figure 65: Boxplot of the flow height in the analysed period. (R3, V2)

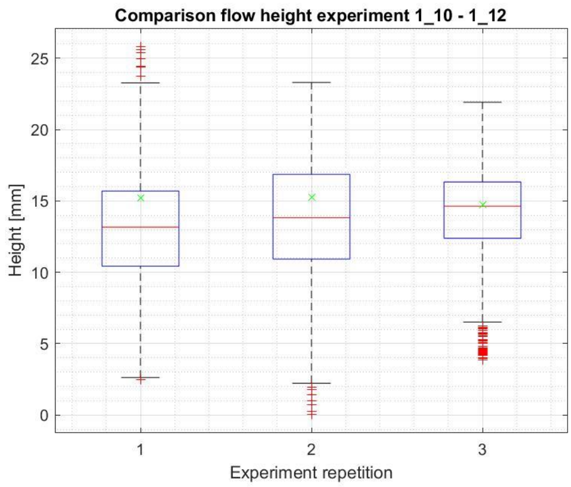

Figure 66: Boxplot of the flow height in the analysed period. (R1W, V1)

Focussing on the different types of surface roughness, no clear trend could be detected except on the macro roughness where the flow height decreased significantly. As illustrated in Figure 67, the flow height increased strongly from the smooth surface to the surfaces with a roughness. Here, it is important to mention that the values in Figure 67 are adjusted regarding the roughness height. Between the three different types of surface roughness, the flow height decreased from R1 to R2 and R1 and R3 had approximately the same flow height in the experiment with the starting volume V1. Only in the experiments with the starting Volume V3 the flow height increased on the roughness R3 and on the roughness R2 the flow height was the smallest again. Nonetheless, with a look at the range of the values and regarding the measurement inaccuracies, neither clear statements could be made nor a clear trend could be detected here.

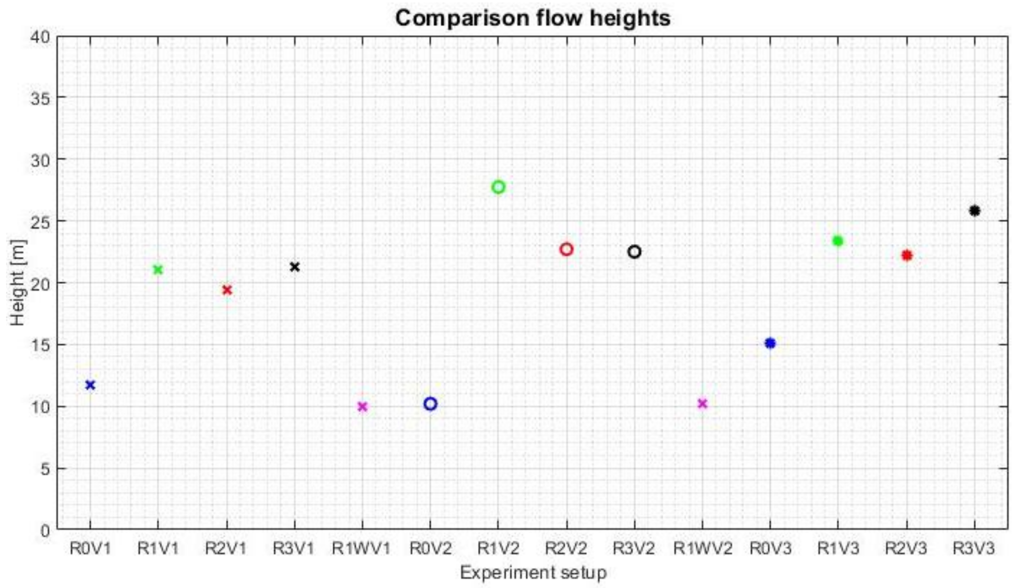

Figure 67: Comparison of the flow height, adjusted regarding the roughness height.

5.3.3 Chézy's coefficient and Strickler coefficient

To also include the flow height via the hydraulic radius and for better illustration of the effect of the roughness height, two roughness coefficients were calculated. For that, the formula according to Brahms-De Chézy and the flow formula according to Gaukler-Manning-Strickler[50], were used.

Brahms-De Chézy formula:[51]

$$v = C * \sqrt{R * I}$$

$v \ldots mean\ velocity\ [m/s]$

$C \ldots Chézy's\ coefficient\ [m^{1/2}/s]$

$R \ldots hydraulic\ radius\ [m]$

$I \ldots flume\ inclination\ [m/m]$

50 Also known as Manning formula.

51 Freimann, Robert (2009), p. 121.

Gaukler-Manning-Strickler formula:[52]

$$v = k_{st} * R^{\frac{2}{3}} * I^{\frac{1}{2}}$$

$v \ldots mean\ velocity\ [m/s]$

$k_{st} \ldots Strickler\ coefficient\ [m^{1/2}/s]$

$R \ldots hydraulic\ radius\ [m]$

$I \ldots flume\ inclination\ [m/m]$

With:

$$k_{st} = C * R^{-\frac{1}{6}}$$

As can be seen in Figure 68 and Figure 69, the coefficients did not change a lot between R2 and R3. This means, at least for these experiments, that increasing the roughness above the grain size makes no difference regarding the mean flow velocities. In reference to chapter 5.2.2, also the velocity profiles did not change. The profiles had the same shape and the inflection point was at the same height. Only the maximum velocities at the surface changed slightly.

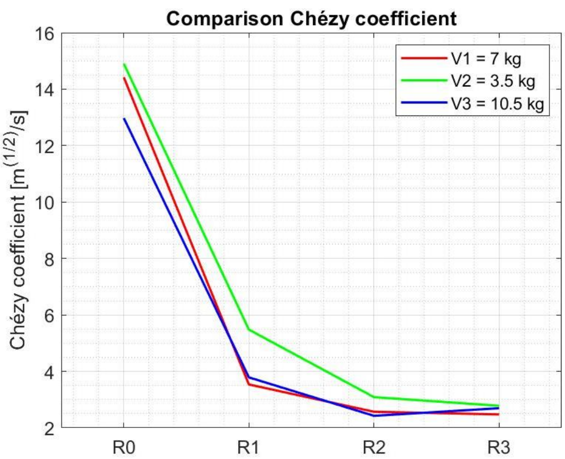

Figure 68: Comparison Chézy coefficient.

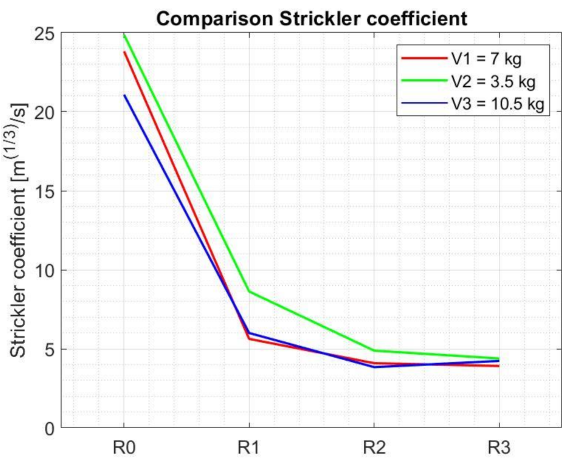

Figure 69: Comparison Strickler coefficient.

52 Ibid., p. 122.

5.3.4 Summary of the results

In order to get a better overview of the results, the most essential outcomes are summarised in this chapter. Table 1 shows a summary of the results.

Table 2: Summary of the results.

	Runout length [cm]	Mean flow height [mm]	Mean Slip velocity [m/s]	Mean velocity [m/s]	Chézy coefficient [$m^{(1/2)}$/s]
R0V1	inf.	11.67	2.5416	2.63	14.90
R1V1	252	21.03	0.1870	0.79	5.90
R2V1	219	19.38	0.0472	0.64	3.66
R3V1	214	21.28	0.0709	0.66	3.54
R1WV1	190	9.92	0.2349	0.4215	1.18
R0V2	inf.	10.19	2.6482	2.64	14.42
R1V2	249	27.74	0.3047	1.24	4.11
R2V2	214	22.70	0.0635	0.76	3.12
R3V2	197	22.51	0.1654	0.74	3.36
R1WV2	190	10.24	0.2529	0.46	1.28
R0V3	inf.	15.13	2.4008	2.49	12.97
R1V3	260	23.33	0.1242	0.85	3,87
R2V3	240	22.20	0.0285	0.59	2.87
R3V3	234	35.82	0.0462	0.71	3.19

As described in the first section of this chapter, the runout distances decreased with higher surface roughness and increased with larger starting volume. The increase of runout distances in the experiments with larger starting volumes is consistent with the higher velocities observed. Since the differences in velocity are very small, it is assumed that the higher mass is more decisive for the runout length. A decrease of the runout distance on the roughest surface occurred despite nearly the same or even higher mean velocities than on roughness R2. Also, the maximum velocities were higher on roughness R3 than on roughness R2. For the runout length, also the deposition in the transition zone may had an essential effect. The depositions in the transition zone were the highest in the experiments with the roughest surface. The mean velocities were the highest on R0, followed from R1 and R3 and the lowest occurred on R2. In order to be able to explain the lower velocities on the roughness R2 than on R3 in the transition zone exactly, further experiments and analyses should be carried out. Nonetheless, it should be noted that the deposition of single beats on the roughest surface, as mentioned before, may have led to a lower absolute roughness height in the later stage of the avalanche. Consequently, the velocities on the roughest surface were higher than on the roughness R2. Moreover, it must be noted that in the analysed time span the flow heights with the starting volume V1 and V2 decreased and increased with the starting volume V3. This indicates that in the experiments with the starting volume V3, the maximum flow height has not yet been reached in the analysed time span. This could have led to a distortion of the results and therefore shows the need to implement analyses over a longer time span. Nevertheless, it can be clearly said that larger starting volumes led to higher flow heights. Regarding roughness height, no significant increase or decrease of the flow heights was observed. Another interesting point is that the velocity profiles only show an inflection point on the two roughest surfaces and an inflection point emerged on R1 with the biggest staring volume V3. On the two roughest surfaces the velocity profiles were also very similar in shape. Hence, the mean velocities in the experiments with the roughness R2 and R3 were approximately the same. Illustrated with the roughness coefficients according to Chézy and Strickler, at a certain point a further increase of the roughness height did not made a difference regarding the velocity profiles.

6 Discussion

To investigate the effects of the surface roughness on dry granular flows, small scale experiments have been carried out. In such experiments, scaling plays an important role but the up-scaling of these experiments to natural gravitational mass flows is problematic. This is due to the fact, that in small scale experiments the ratio of all forces cannot be hold constant with regard to large scale flows.[53] These scaling effect, which become bigger with the scaling factor, can affect the flow velocities or runout lengths significantly.[54] It is also difficult to describe the flow regime because in this type of granular flows the friction between the grains as well as the collisions play an important role.[55] However, the detected changes of the velocity profiles over time point out that this should also be considered for modelling mass movements since these are also known from natural debris flows.[56] Also, the observed change of the shape when regarding the changing boundary conditions should be considered when modelling gravitational mass flows. Since the test channel had a very small width and therefore the possible starting volume was limited, some problems arose, which are described below. As well, the high inclination of the flume may be a problem because the material accelerated continuously on the smooth surface, thus no steady flow was established. [57] However, the high inclination was necessary as below this angle the material would have stopped on the roughest surface. Nevertheless, the high surface roughness led to depositions along the whole channel which may have falsified the results of the runout lengths because on the smaller surface roughness R1 no depositions occurred along the path. Also, the measurement of the runout lengths with the described definition in chapter 4.3.1 leads to inaccuracies, especially on the rougher surfaces. This is due to single roughness elements that stand out of the deposition and therefore the measurement is either falsified or judged rather subjectively. Especially on the highest roughness in combination with a very small deposition height, the definition of a continuous line of ceramic beats can be shifted. With reference to Jop et al. (2005), the friction of the side wall is not negligible. Furthermore, flow characteristics in narrow channels differ from wide channels. Therefore, caution is advised when interpreting results of experiments in narrow channels like in this setup.[58] Moreover, the slip velocities may be much faster in the centre of the flume than

[53] Iverson, Richard M. (2015), p. 19.

[54] Kesseler, Matthew et al. (2018), p. 2145, 2157.

[55] Pouliquen, O. (1999), p. 542.

[56] Nagl, Georg et al. (2019).

[57] Pouliquen, O. (1999), p. 542.

[58] Jop, Pierre et al. (2005), p. 20.

on the side wall where the high-speed recordings were undertaken. This means that the absolute values of the slip velocities must be treated with caution. Nevertheless, the behaviour of the decrease along the observed time may be the same and therefore the side-wall effects are not dominant. [59] In order to verify the velocities in the video recordings, the velocities on the front were measured using laser sensors positioned in the middle of the channel. Unfortunately, comparisons between the velocities measured by laser sensors and those extracted from high-speed recordings were only possible on the smooth surface. On the rougher surfaces, the velocities measured from the laser sensors were scattered widely and therefore many values were unclear. Even on the smooth surface, it can only be said that the velocities are within a realistic range as the rather loose flow of individual grains made it difficult to measure the velocities sufficiently accurate. Moreover, the velocities measured with laser sensors were in the front and the extracted velocities from the video analysis were within the avalanche. Furthermore, the measured flow heights varied in a wide range due to the loose flow on the rougher surfaces, which leads to the next problem. The measurement with the laser sensors, which only measure on a tiny area, led to wide scattered values. Due to the high measurement frequency, the laser sensors scanned the whole surface of single particles. Even here is already an inaccuracy but the bigger problem was the loose flow especially on the rough surfaces with a small starting volume. This loose flow resulted in many values that were measured within the flowing mass and not on the surface. Therefore, an upper percentile of the measured values was chosen for the flow height, which was defined in comparison with the video recordings and best fitted for all experiments. As this may again lead to inaccuracies on individual level, it is recommended to undertake further experiments with larger starting volumes to get a dense flow in each experiment and therefore the possibility to determine the flow height more precisely. Additionally, the experiments with the smallest starting volumes exhibited a different flow behaviour which gave interesting results but made a comparison with the other volumes difficult. So, it is also recommended to conduct further experiments with larger starting volumes to get more information about the influence of the relative roughness. Regarding the changing profile from the head to the tail of the flow, the period analysed should also be extended in further experiments.[60] This also indicates that different phases of the flow were recorded for the different setups in the analysed time span. In order to confirm this, it would be interesting to evaluate the high-speed recordings of this thesis' experiments over the entire period. Unfortunately, this exceeded the scope of this

[59] Schaefer, Marius et al. (2010), p. 8.

[60] Schaefer, Marius and Bugnion, Louis (2013), p. 10.

master's thesis due to the extremely long computation time for the evaluation of the high-speed recordings.

The results of the few experiments with the macro roughness indicate that this roughness had great effects on the runout lengths and velocities of the flowing mass. For further experiments with the macro roughness it is advisable to establish a preceding acceleration path so that a flow can develop before it hits the obstacles. This is recommended because in the experiments conducted for this master's thesis, with placed macro roughness elements directly behind the reservoir, the discharge was limited from beginning and thus the starting volume did not make a difference. Therefore, it seems important to conduct further experiments with different variations, e.g. changing covered area, changing number of sticks etc., of this macro roughness. All the experiments carried out went smoothly but they also revealed some problems and showed possibilities for improvement, as described above.

Nevertheless, the research questions can be answered as follows:

RQ1: How does the surface roughness affect the runout distance of dry granular avalanches?

Based on these experiments, there are clear indications that the runout length of dry granular flows decreases with increasing height of surface roughness.

RQ2: How does the surface roughness affect the velocity profiles?

The experiments in this study showed that the velocity profiles changed regarding to the different surface types but only up to a certain roughness height.

RQ3: How does the surface roughness affect the flow height and does the relative roughness play a role?

In the experiments of this study, no significant change of the flow height regarding surface roughness could be observed. Also, no significant change regarding different ratios from flow height to roughness height could be detected. However, it has been noted in the discussion that further experiments are necessary to clarify this research question in detail.

7 Conclusion

The aim of this master's thesis was to investigate the influence of surface roughness on dry granular gravitational mass flows. For that, laboratory experiments in a small scale were carried out. The measurement methods ranged from very simple to complex. The runout lengths were measured with a ruler, flow depth and front velocities with laser sensors and the velocity profiles were extracted from high-speed recordings. Regarding these measuring techniques and the evaluation methods, there is still room for improvement in order to capture all relevant parameters of such a complex process. Interesting insights could have been gained from these laboratory experiments and regarding the experimental setup important information and improvement suggestions for further experiments could have been collected. Moreover, a good data basis for further evaluation methods or model testing has been generated. The experiments showed clear differences in the runout lengths on different types of surface roughness. Furthermore, a change in the shape of velocity profiles became apparent from a certain height of surface roughness. The velocity profiles on the two roughest surfaces showed an inflection point independent of the starting volume and were pretty much the same but differed from the smoother surface roughness. This indicates that there is a difference in velocity profiles between smooth and rough but no difference between rough and very rough. Besides, velocity profiles changed with different starting volumes, specifically when the density of the flowing mass or the load on the bottom layer changed. Hence, with the smallest starting volume the profiles changed from linear to concave and on the roughness R1 an inflection point occurred with the biggest starting volume. It also could be observed that the velocity profiles changed from head to tail. In these experiments, a significant difference between a smooth and a rough surface on the flow height was observed. To get more information about these effects as well as their influence on the relative roughness, it is necessary and recommended to undertake further experiments with larger starting volumes and on a larger scale. Overall, the results show the importance to continue research to get a better understanding of the flow behaviour of gravitational mass flows at different boundary conditions.

8 List of references

Armanini, Aronne, Capart, Hervé, Fraccarollo, Luigi and Larcher, Michele (2005): Rheological stratification in experimental free-surface flows of granular–liquid mixtures. *In: Journal of Fluid Mechanics*, Volume 532, 10.06.2005, p. 269–319, DOI: 10.1017/S0022112005004283.

BMLFUW (2012): Schutz vor Naturgefahren in Österreich 2002-2011, Bundesministerium für Land- und Forstwirtschaft, Umwelt und Wasserwirtschaft Sektionen Wasser und Forstwesen, 2012, https://www.bmnt.gv.at/dam/jcr:55f12a5a-aa8e-4e16-bb61-b77767412e85/Schutz%20vor%20Naturgefahren%20in%20%C3%96sterreich_2002-2011.pdf.

Calo, Victor M., Collier, Nathan, Gehre, Matthias, Jin, Bangti, Radwan, Hany and Santillana, Mauricio (2013): Gradient-based estimation of Manning's friction coefficient from noisy data. *In: Journal of Computational and Applied Mathematics*, Volume 238, 01.2013, p. 1–13, DOI: 10.1016/j.cam.2012.08.004.

Campbell, C S (1990): Rapid Granular Flows. *In: Journal of Fluid Mechanics*, Volume 22, 1990, p. 57–92.

Cheng, Yung Ming, Fung, Wing Hong Ivan, Li, Liang and Li, Na (2019): Laboratory and field tests and distinct element analysis of dry granular flows and segregation processes. *In: Natural Hazards and Earth System Sciences*, Volume 19, Issue 1, 22.01.2019, p. 181–199, DOI: 10.5194/nhess-19-181-2019.

Dietrich, William E., Bellugi, Dino G., Sklar, Leonard S., Stock, Jonathan D., Heimsath, Arjun M. and Roering, Joshua J. (2013): Geomorphic Transport Laws for Predicting Landscape form and Dynamics, in: Wilcock, Peter R. and Iverson, Richard M. (Ed): *Geophysical Monograph Series*, Washington, D. C, 2013, p. 103–132, ISBN: 978-1-118-66855-9, DOI: 10.1029/135GM09.

Fischer, Jan-Thomas, Kaitna, Roland, Heil, Kilian and Reiweger, Ingrid (2018): The Heat of the Flow: Thermal Equilibrium in Gravitational Mass Flows. *In: Geophysical Research Letters*, Volume 45, Issue 20, 28.10.2018, p. 219–226, DOI: 10.1029/2018GL079585.

Forterre, Yoël and Pouliquen, Olivier (2008): Flows of Dense Granular Media. *In: Annual Review of Fluid Mechanics*, Volume 40, Issue 1, 01.2008, p. 1–24, DOI: 10.1146/annurev.fluid.40.111406.102142.

Freimann, Robert (2009): Hydraulik für Bauingenieure: Grundlagen und Anwendungen ; mit 59 Tabellen, 57 Beispielen, 56 Aufgaben mit Lösungen und einem Verzeichnis englischer Fachbegriffe, München, Fachbuchverl. Leipzig im Hanser Verl, 2009, ISBN: 978-3-446-41054-1.

GDR MiDi (2004): On dense granular flows. *In: The European Physical Journal E*, Volume 14, Issue 4, 08.2004, p. 341–365, DOI: 10.1140/epje/i2003-10153-0.

Gollin, Devis (2017): An investigation on the collisional behaviour of granular flows, University of Sheffield, 2017.

de Haas, Tjalling, Braat, Lisanne, Leuven, Jasper R. F. W., Lokhorst, Ivar R. and Kleinhans, Maarten G. (2015): Effects of debris flow composition on runout, depositional mechanisms, and deposit morphology in laboratory experiments: Experimental Debris Flows. *In: Journal of Geophysical Research: Earth Surface*, Volume 120, Issue 9, 09.2015, p. 1949–1972, DOI: 10.1002/2015JF003525.

Heiser, M., Scheidl, C. and Kaitna, R. (2017): Evaluation concepts to compare observed and simulated deposition areas of mass movements. *In: Computational Geosciences*, Volume 21, Issue 3, 06.2017, p. 335–343, DOI: 10.1007/s10596-016-9609-9.

Hunger, O and Morgenstern, N. R. (1984): High velocity ring shear tests on sand. *In: Géotechnique*, Volume 34, Issue 3, 09.1984, p. 415–421, DOI: 10.1680/geot.1984.34.3.415.

Hungr, Oldrich (1995): A model for the runout analysis of rapid flow slides, debris flows, and avalanches. *In: Canadian Geotechnical Journal*, Volume 32, 01.08.1995, p. 610–623, DOI: 10.1139/t95-063.

Hungr, Oldrich (2008): Simplified models of spreading flow of dry granular material. *In: Canadian Geotechnical Journal*, Volume 45, Issue 8, 08.2008, p. 1156–1168, DOI: 10.1139/T08-059.

Hungr, Oldrich and McDougall, Scott (2009): Two numerical models for landslide dynamic analysis. *In: Computers & Geosciences*, Volume 35, Issue 5, 05.2009, p. 978–992, DOI: 10.1016/j.cageo.2007.12.003.

Iverson, Richard M. (1997): The physics of debris flows. *In: Reviews of Geophysics*, Volume 35, Issue 3, 08.1997, p. 245–296, DOI: 10.1029/97RG00426.

Iverson, Richard M. (2015): Scaling and design of landslide and debris-flow experiments. *In: Geomorphology*, Volume 244, 09.2015, p. 9–20, DOI: 10.1016/j.geomorph.2015.02.033.

Iverson, Richard M and George, David L (2018): Valid debris-flow models must avoid hot starts, 2018, p. 8.

Jop, Pierre, Forterre, Yoël and Pouliquen, Olivier (2005): Crucial role of sidewalls in granular surface flows: consequences for the rheology. *In: Journal of Fluid Mechanics*, Volume 541, Issue 1, 11.10.2005, p. 167, DOI: 10.1017/S0022112005005987.

Kaitna, R., Dietrich, W. E. and Hsu, L. (2014): Surface slopes, velocity profiles and fluid pressure in coarse-grained debris flows saturated with water and mud. *In: Journal of Fluid Mechanics*, Volume 741, 25.02.2014, p. 377–403, DOI: 10.1017/jfm.2013.675.

Kaitna, R., Rickenmann, D. and Schatzmann, M. (2007): Experimental study on rheologic behaviour of debris flow material. *In: Acta Geotechnica*, Volume 2, Issue 2, 17.07.2007, p. 71–85, DOI: 10.1007/s11440-007-0026-z.

Kesseler, Matthew, Heller, Valentin and Turnbull, Barbara (2018): A laboratory-numerical approach for modelling scale effects in dry granular slides. *In: Landslides*, Volume 15, Issue 11, 11.2018, p. 2145–2159, DOI: 10.1007/s10346-018-1023-z.

Limerinos, J.T. (1970): Determination of the manning coefficient from measured bed roughness in natural channels, 1970, https://pubs.er.usgs.gov/publication/wsp1898B, DOI: 10.3133/wsp1898B.

Lorenzini, G. and Mazza, N. (2004): Debris flow: phenomenology and rheological modelling, Southampton ; Boston, WIT, 2004, ISBN: 978-1-85312-802-8.

Marinell, Gerhard and Steckel-Berger, Gabriele (2008): Einführung in die Statistik: anwendungsorientierte Methoden zur Datenauswertung, 2., überarb. und erw. Aufl, München, Oldenbourg, 2008, ISBN: 978-3-486-58713-5.

Mcdougall, Scott (2006): A NEW CONTINUUM DYNAMIC MODEL FOR THE ANALYSIS OF EXTREMELY RAPID LANDSLIDE MOTION ACROSS COMPLEX 3D TERRAIN, University of Toronto, 2006.

Morvan, Hervé, Knight, Donald, Wright, Nigel, Tang, Xiaonan and Crossley, Amanda (2008): The concept of roughness in fluvial hydraulics and its formulation in 1D, 2D and 3D numerical simulation models. *In: Journal of Hydraulic Research*, Volume 46, Issue 2, 03.2008, p. 191–208, DOI: 10.1080/00221686.2008.9521855.

Nagl, Georg, Hübl, Johannes and Kaitna, Roland (2019): Evolution of vertical velocity profiles along a sequence of debris flow surges, Vienna, 07.04.2019.

Nagl, Georg, Hübl, Johannes and Kaitna, Roland (2020): Velocity profiles and basal stresses in natural debris flows. *In: Earth Surface Processes and Landforms*, 05.03.2020, p. esp.4844, DOI: 10.1002/esp.4844.

Pellegrino, Anna and Schippa, Leonardo (2017): Rheological Modeling of Macro Viscous Flows of Granular Suspension of Regular and Irregular Particles. *In: Water*, Volume 10, Issue 1, 27.12.2017, p. 21, DOI: 10.3390/w10010021.

Popov, Valentin L. (2010): Contact mechanics and friction: physical principles and applications, English ed., Heidelberg ; New York, Springer, 2010, ISBN: 978-3-642-10802-0.

Pouliquen, O. (1999): Scaling laws in granular flows down rough inclined planes. *In: Physics of Fluids*, Volume 11, Issue 3, 03.1999, p. 542–548, DOI: 10.1063/1.869928.

Pudasaini, Shiva P. and Hutter, Kolumban (2007): Avalanche dynamics: dynamics of rapid flows of dense granular avalanches, Berlin ; New York, Springer, 2007, ISBN: 978-3-540-32686-1.

Schaefer, Marius and Bugnion, Louis (2013): Velocity profile variations in granular flows with changing boundary conditions: insights from experiments. *In: Physics of Fluids*, Volume 25, Issue 6, 06.2013, p. 063303, DOI: 10.1063/1.4810973.

Schaefer, Marius, Bugnion, Louis, Kern, Martin and Bartelt, Perry (2010): Position dependent velocity profiles in granular avalanches. *In: Granular Matter*, Volume 12, Issue 3, 05.2010, p. 327–336, DOI: 10.1007/s10035-010-0179-6.

Schneider, D., Kaitna, R., Dietrich, W.E., Hsu, L., Huggel, C. and McArdell, B.W. (2011): Frictional behavior of granular gravel–ice mixtures in vertically rotating drum experiments and implications for rock–ice avalanches. *In: Cold Regions Science and Technology*, Volume 69, Issue 1, 10.2011, p. 70–90, DOI: 10.1016/j.coldregions.2011.07.001.

Thielicke, William and Stamhuis, Eize J. (2014): PIVlab – Towards User-friendly, Affordable and Accurate Digital Particle Image Velocimetry in MATLAB. *In: Journal of Open Research Software*, Volume 2, 16.10.2014, p. 10, DOI: 10.5334/jors.bl.

Web sources:

MathWorks (2020): Box plot - MATLAB boxplot - MathWorks Deutschland, 2020, accessed 29.01.2020, https://de.mathworks.com/help/stats/boxplot.html.

VVO Versicherungsverband Österreich (2018): Naturkatastrophen: Auswirkungen werden in Österreich stark unterschätzt, ots.at, 15.06.2018, accessed 07.02.2020, https://www.ots.at/presseaussendung/OTS_20180615_OTS0118/naturkatastrophen-auswirkungen-werden-in-oesterreich-stark-unterschaetzt-bild.

Wildbach- und Lawinenverbauung und Schutzwaldpolitik (Abteilung III/4) (2019): Salzburg: Millionenprojekt zum Schutz vor Muren und Hochwasser im Glemmtal, bmlrt.gv.at, 14.10.2019, accessed 07.02.2020, https://www.bmlrt.gv.at/forst/wildbach-lawinenverbauung/aktuelles-dienststellen-fachabteilung/glemmtal_saalach.html.

WSL - Institut für Schnee- und Lawinenforschung SLF (2020): RAMMS - Rapid Mass MovementS: Background Information, 19.03.2020, accessed 19.03.2020, https://ramms.slf.ch/ramms/index.php?option=com_content&view=article&id=57&Itemid=74#friction%20models.

9 Appendix

In the following, the results of each experiment are presented.

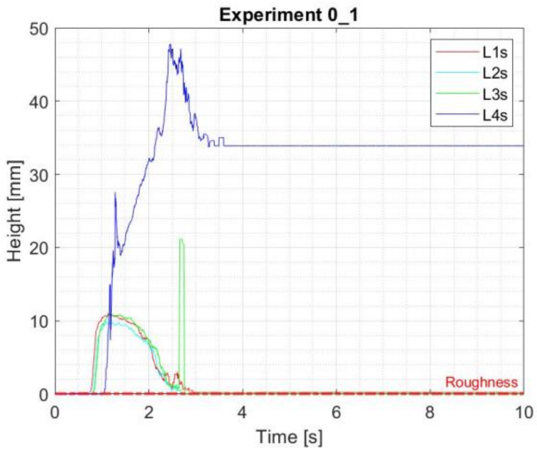

Figure A 1: Smoothed laser signals experiment R0 V1 repetition 1.

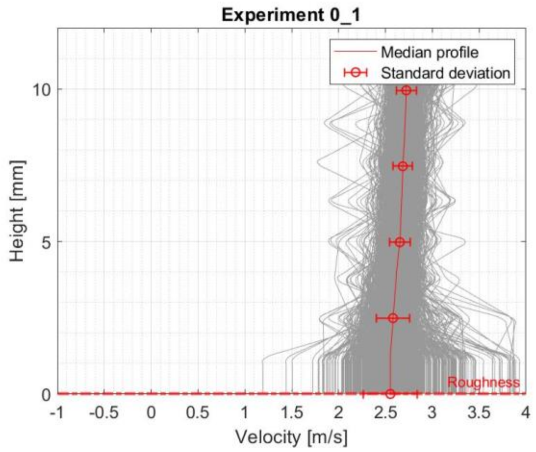

Figure A 2: Median profile R0 V1 repetition 1.

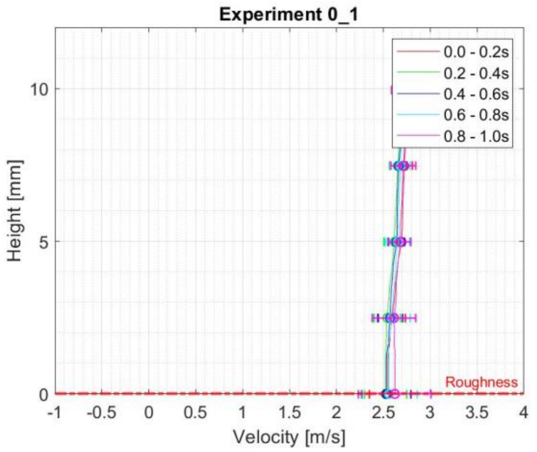

Figure A 3: Profiles over time R0 V1 repetition 1.

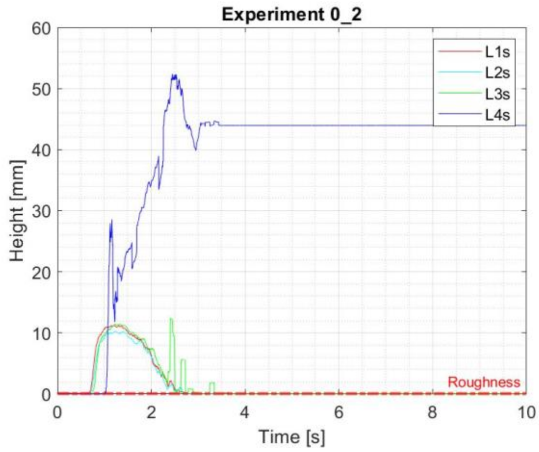

Figure A 4: Smoothed laser signals experiment R0 V1 repetition 2.

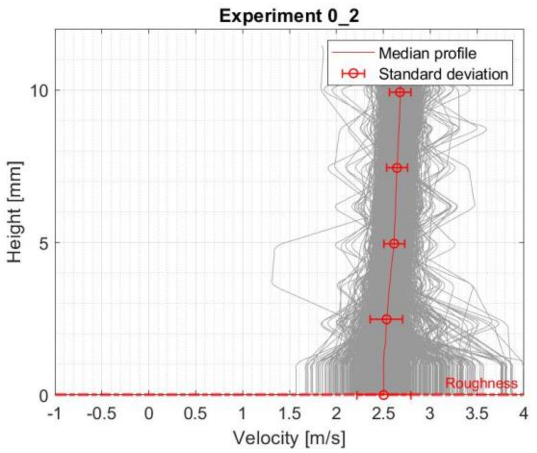

Figure A 5: Median profile R0 V1 repetition 2.

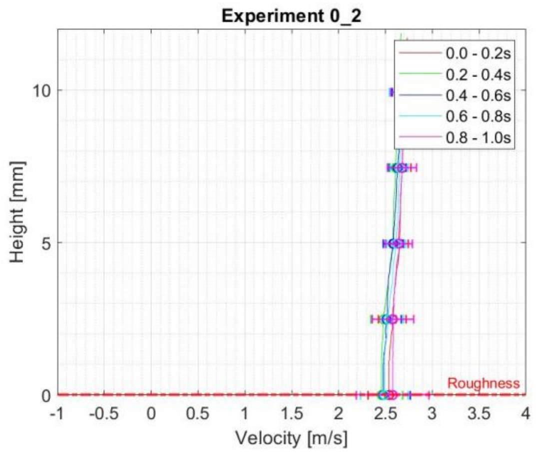

Figure A 6: Profiles over time R0 V1 repetition 2.

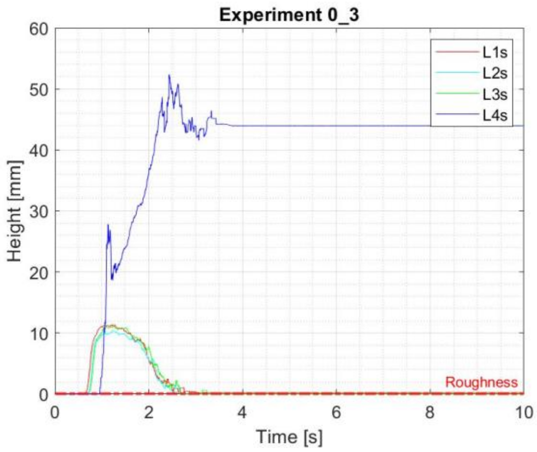

Figure A 7: Smoothed laser signals experiment R0 V1 repetition 3.

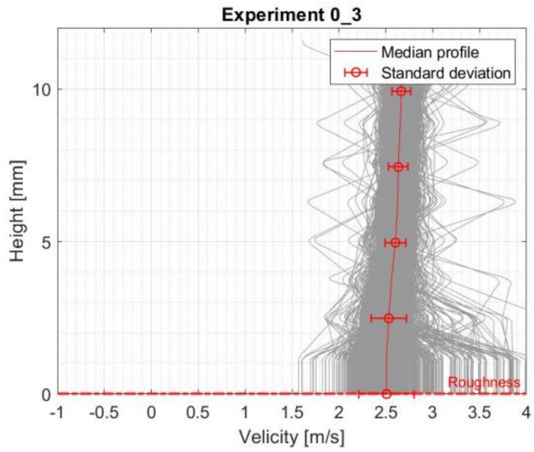

Figure A 8: Median profile R0 V1 repetition 3.

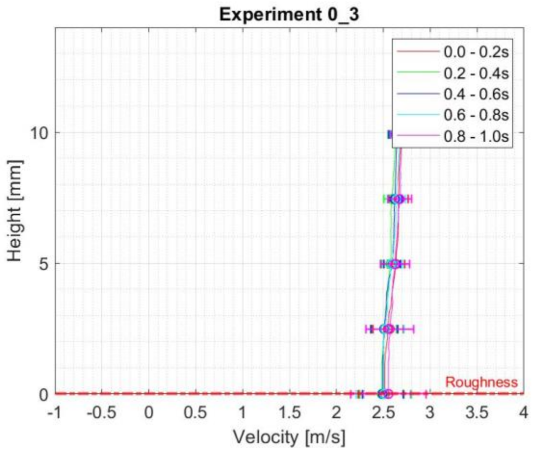

Figure A 9: Profiles over time R0 V1 repetition 3.

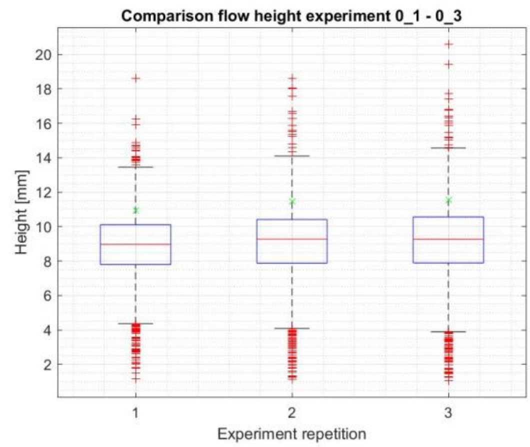

Figure A 10: Comparison boxplot flow heights R0 V1 repetition 1-3.

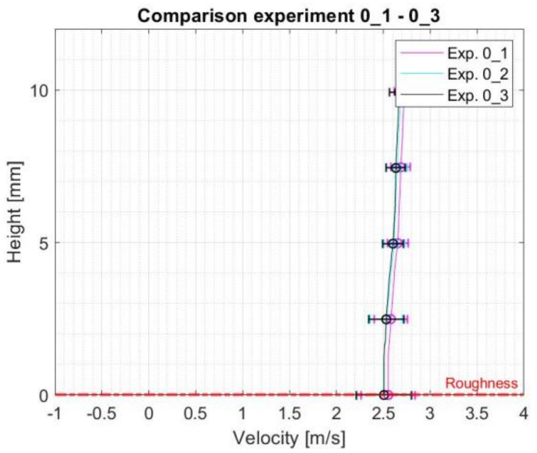

Figure A 11: Comparison profiles R0 V1 repetition 1-3.

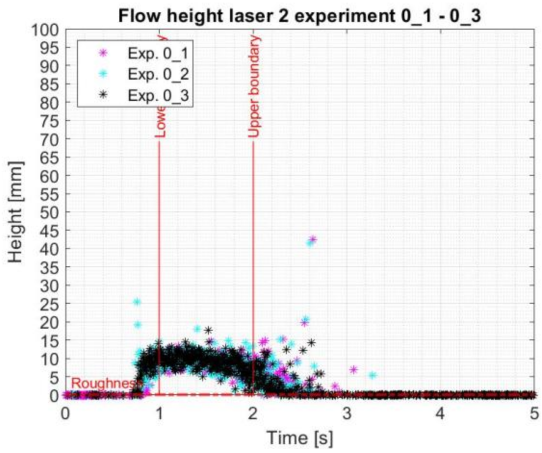

Figure A 12: Analysed section R0 V1 repetition 1-3.

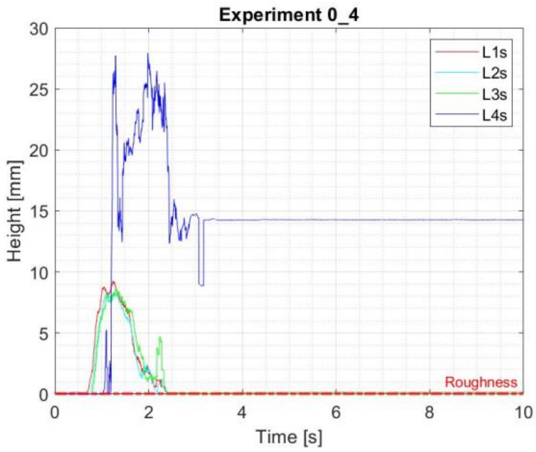

Figure A 13: Smoothed laser signals experiment R0 V2 repetition 1.

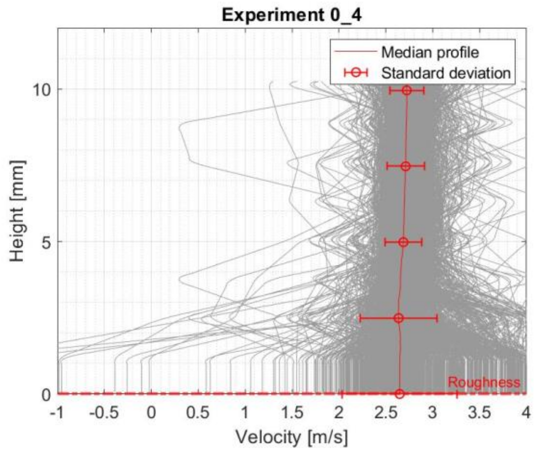

Figure A 14: Median profile R0 V2 repetition 1.

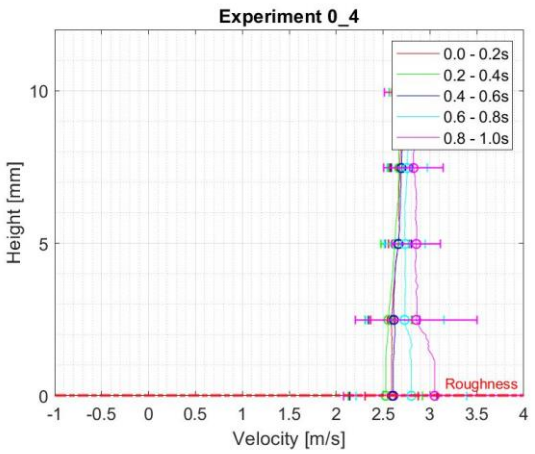

Figure A 15: Profiles over time R0 V2 repetition 1.

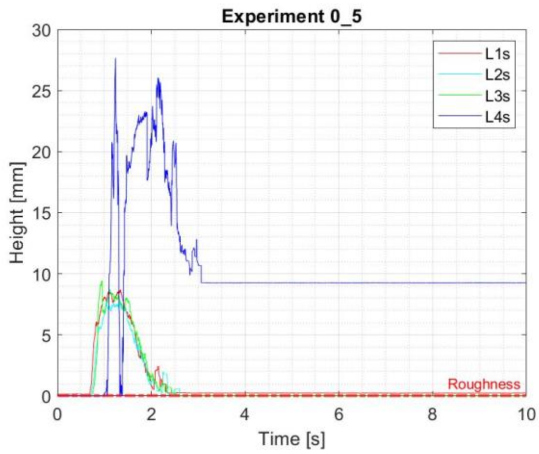

Figure A 16: Smoothed laser signals experiment R0 V2 repetition 2.

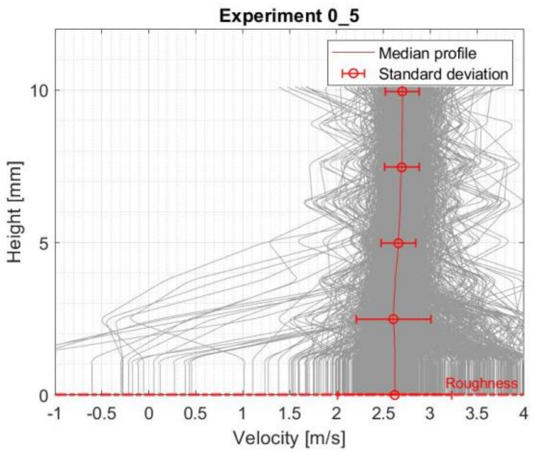

Figure A 17: Median profile R0 V2 repetition 2.

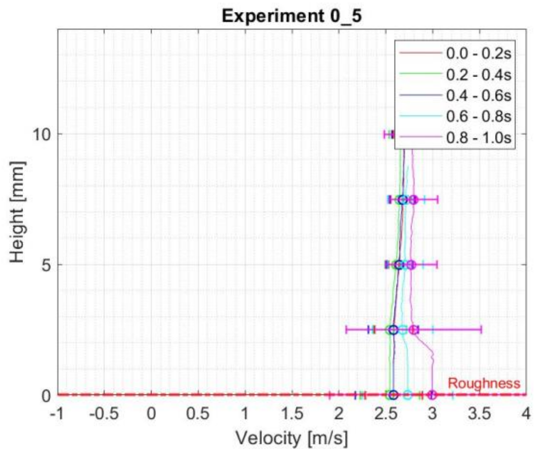

Figure A 18: Profiles over time R0 V2 repetition 2.

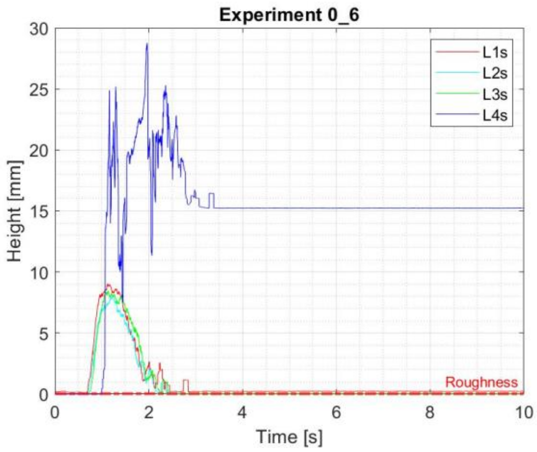

Figure A 19: Smoothed laser signals experiment R0 V2 repetition 3.

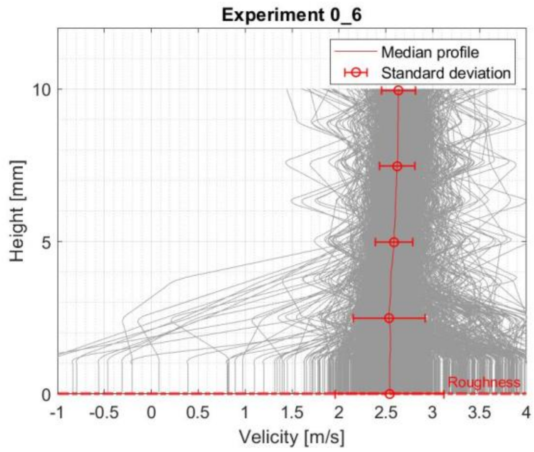

Figure A 20: Median profile R0 V2 repetition 3.

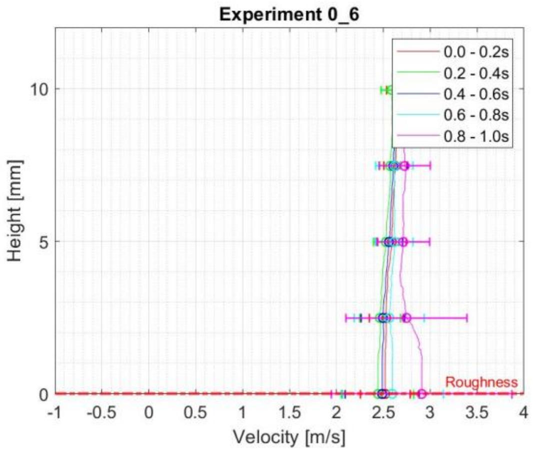

Figure A 21: Profiles over time R0 V2 repetition 3.

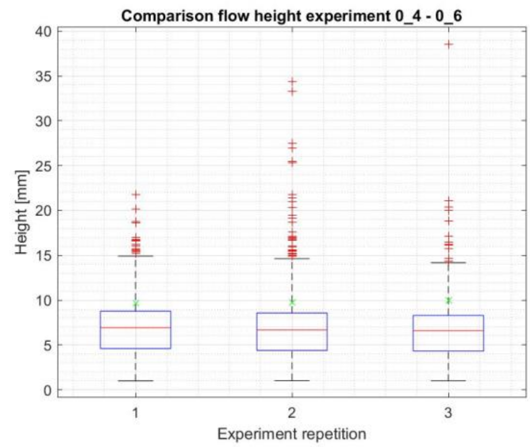

Figure A 22: Comparison boxplot flow heights R0 V2 repetition 1-3.

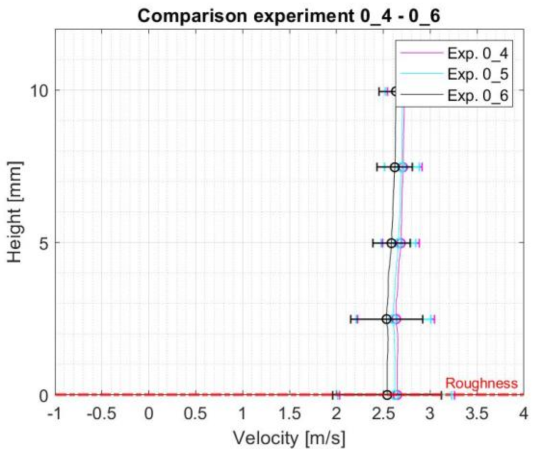

Figure A 23: Comparison profiles R0 V2 repetition 1-3.

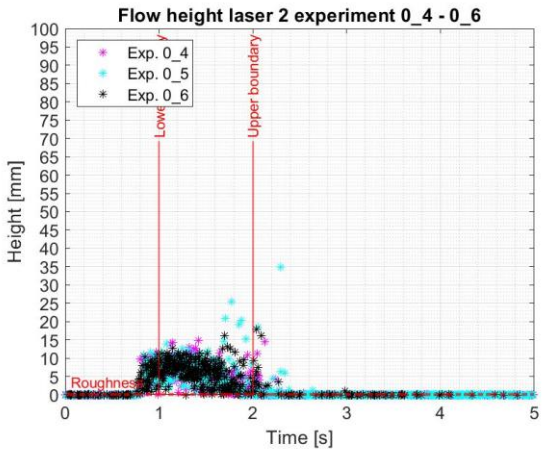

Figure A 24: Analysed section R0 V2 repetition 1-3.

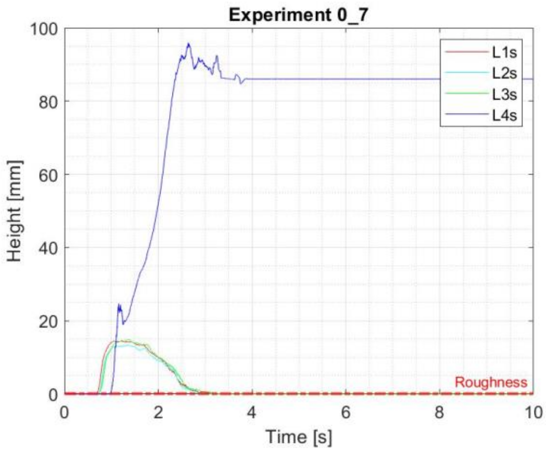

Figure A 25: Smoothed laser signals experiment R0 V3 repetition 1.

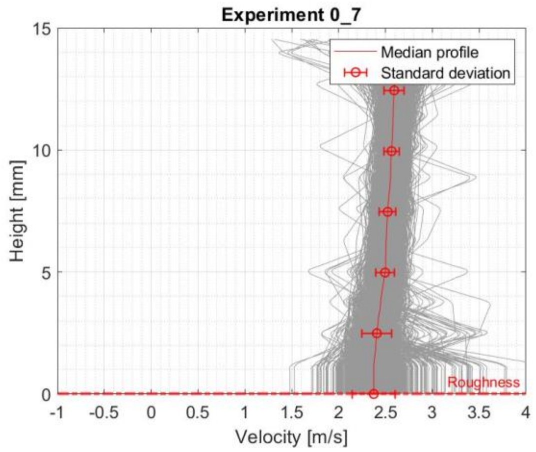

Figure A 26: Median profile R0 V3 repetition 1.

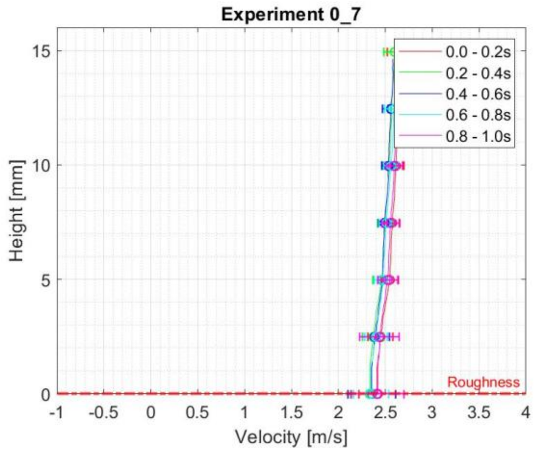

Figure A 27: Profiles over time R0 V3 repetition 1.

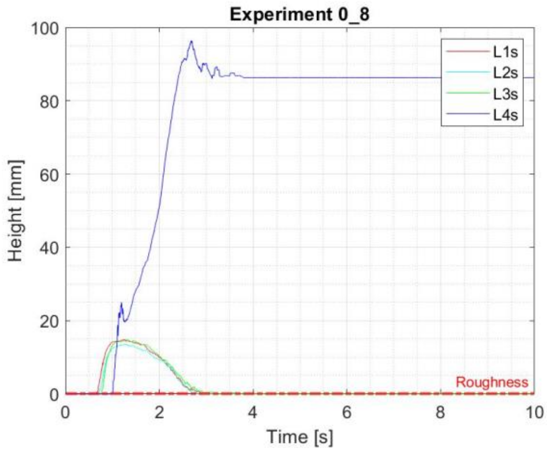

Figure A 28: Smoothed laser signals experiment R0 V3 repetition 2.

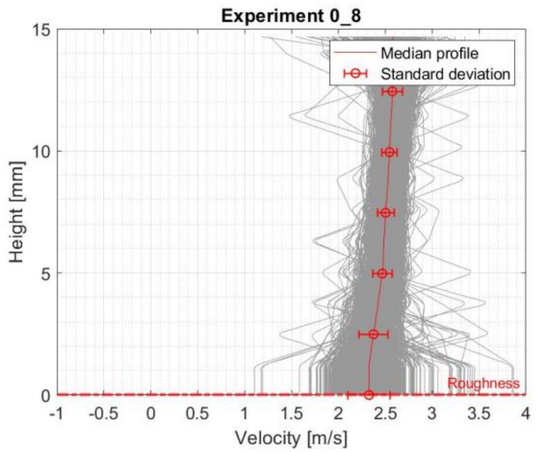

Figure A 29: Median profile R0 V3 repetition 2.

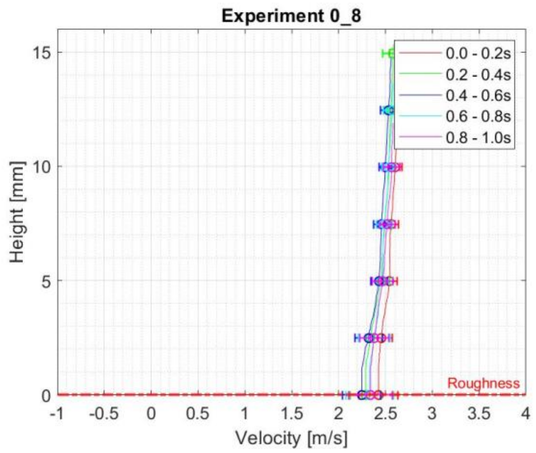

Figure A 30: Profiles over time R0 V3 repetition 2.

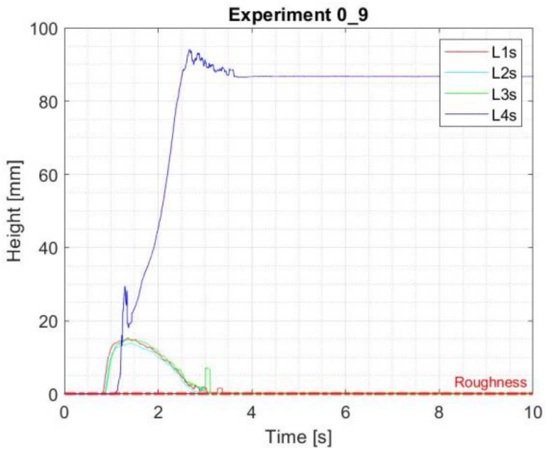

Figure A 31: Smoothed laser signals experiment R0 V3 repetition 3.

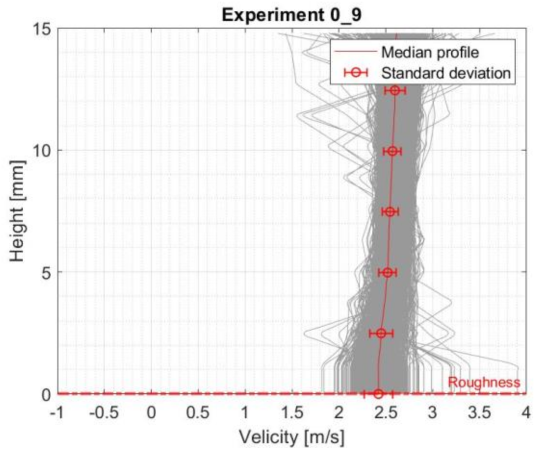

Figure A 32: Median profile R0 V3 repetition 3.

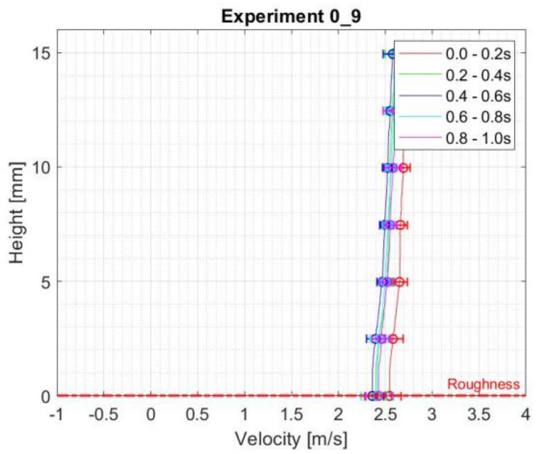

Figure A 33: Profiles over time R0 V3 repetition 3.

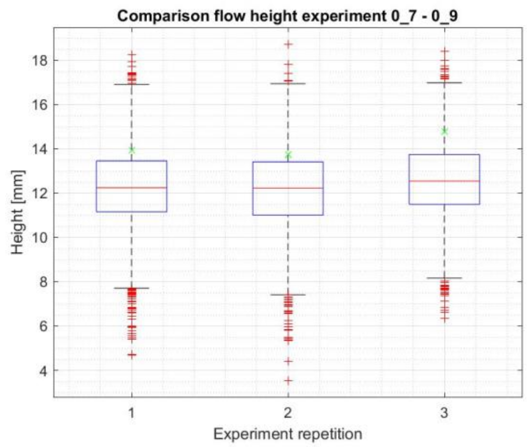

Figure A 34: Comparison boxplot flow heights R0 V3 repetition 1-3.

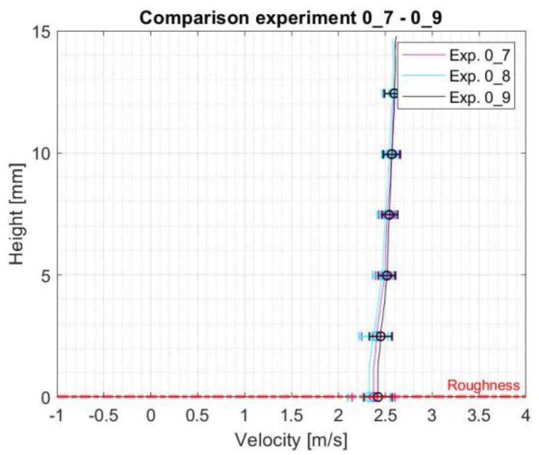

Figure A 35: Comparison profiles R0 V3 repetition 1-3.

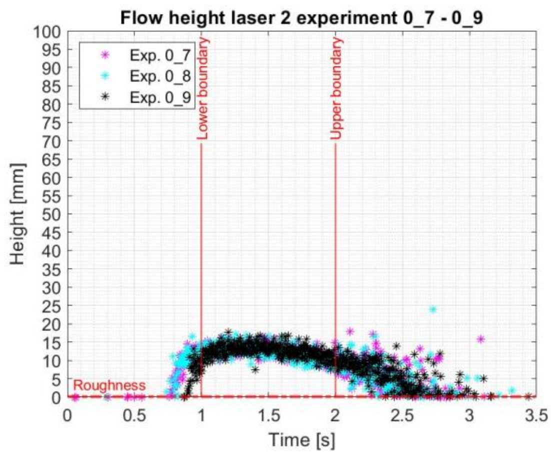

Figure A 36: Analysed section R0 V3 repetition 1-3.

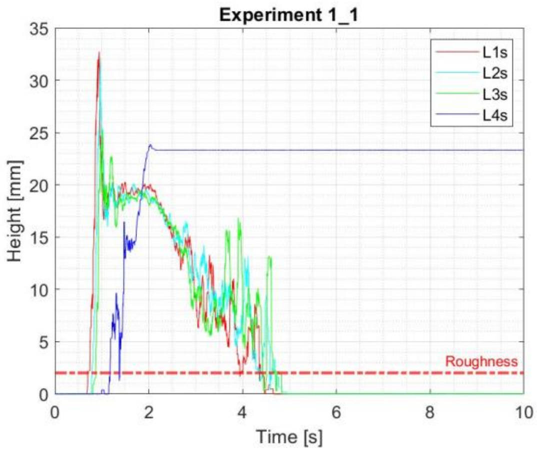

Figure A 37: Smoothed laser signals experiment R1 V1 repetition 1.

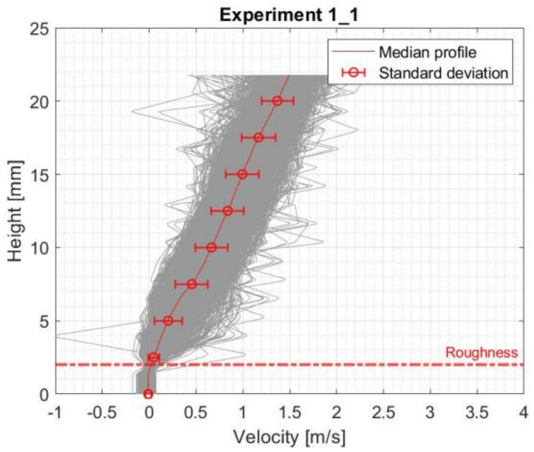

Figure A 38: Median profile R1 V1 repetition 1.

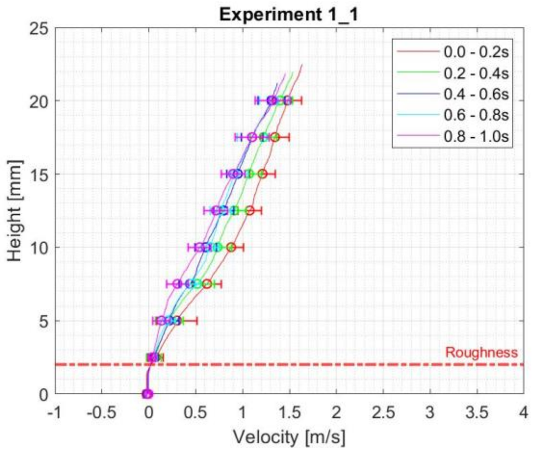

Figure A 39: Profiles over time R1 V1 repetition 1.

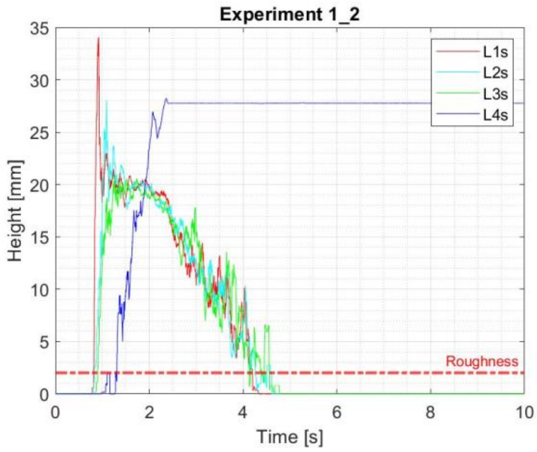

Figure A 40: Smoothed laser signals experiment R1 V1 repetition 2.

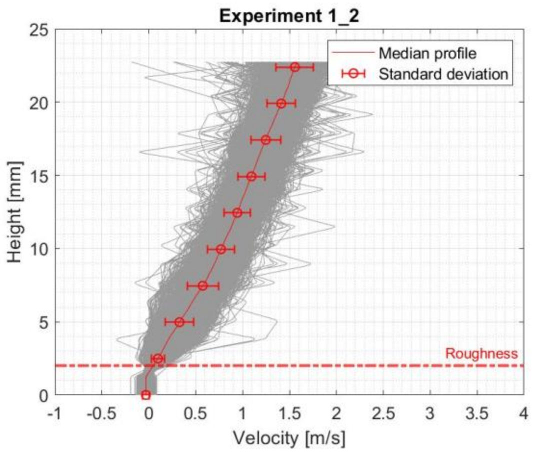

Figure A 41: Median profile R1 V1 repetition 2.

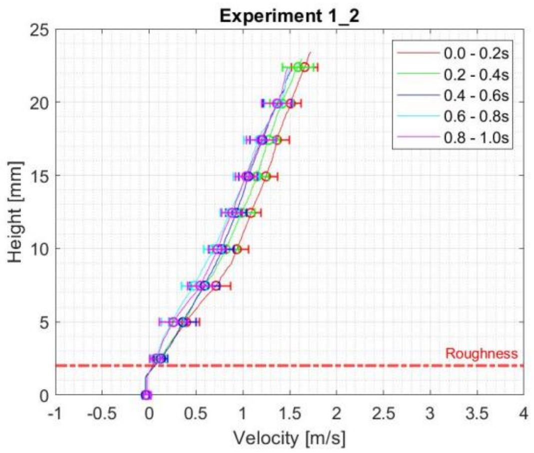

Figure A 42: Profiles over time R1 V1 repetition 2.

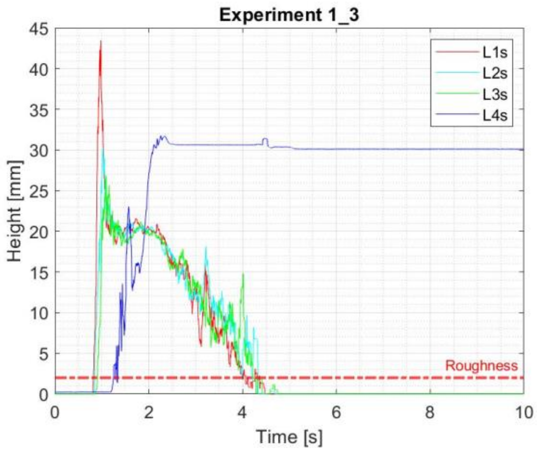

Figure A 43: Smoothed laser signals experiment R1 V1 repetition 3.

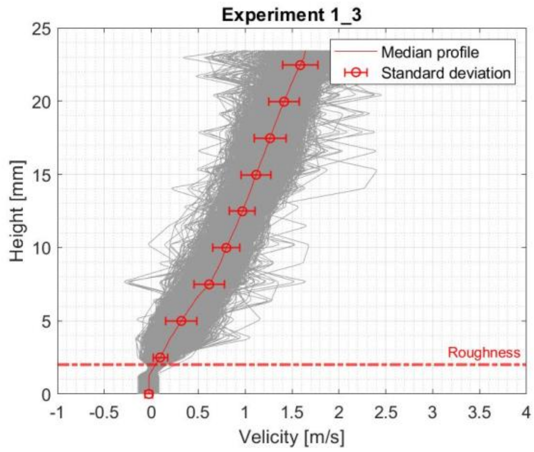

Figure A 44: Median profile R1 V1 repetition 3.

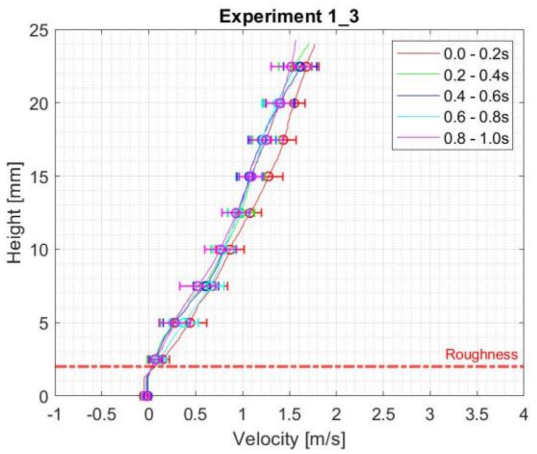

Figure A 45: Profiles over time R1 V1 repetition 3.

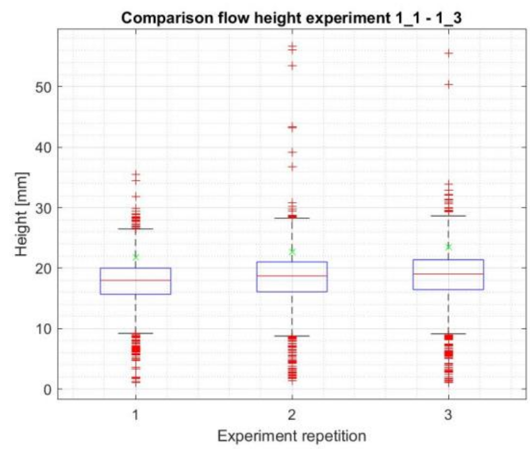

Figure A 46: Comparison boxplot flow heights R1 V1 repetition 1-3.

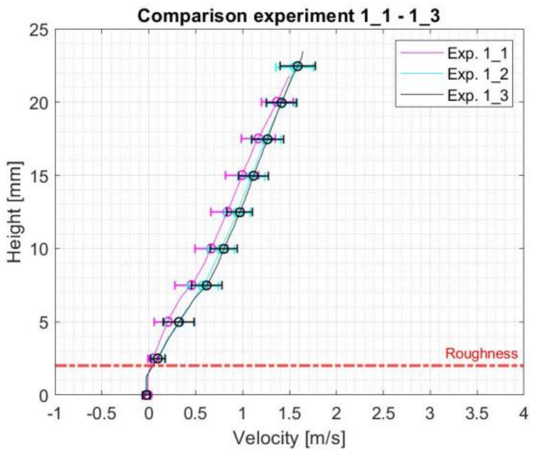

Figure A 47: Comparison profiles R1 V1 repetition 1-3.

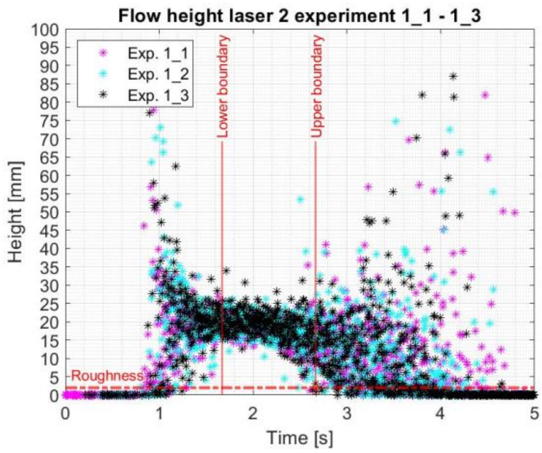

Figure A 48: Analysed section R1 V1 repetition 1-3.

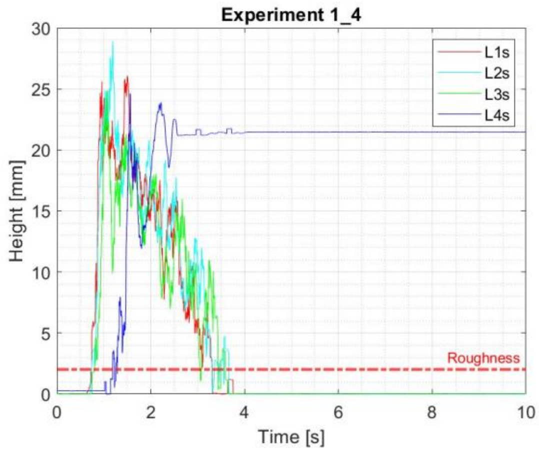

Figure A 49: Smoothed laser signals experiment R1 V2 repetition 1.

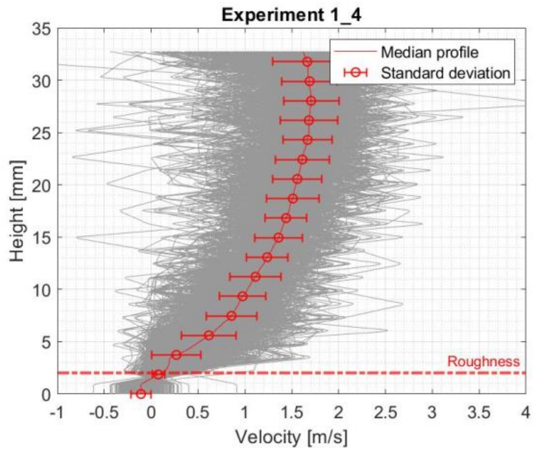

Figure A 50: Median profile R1 V2 repetition 1.

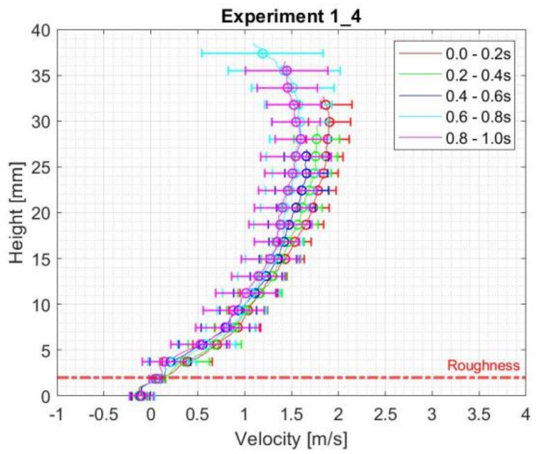

Figure A 51: Profiles over time R1 V2 repetition 1.

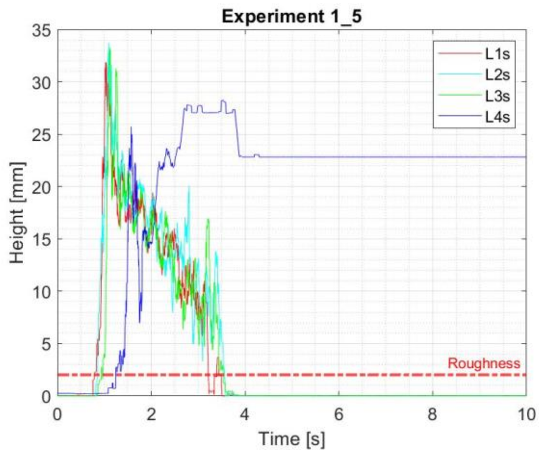

Figure A 52: Smoothed laser signals experiment R1 V2 repetition 2.

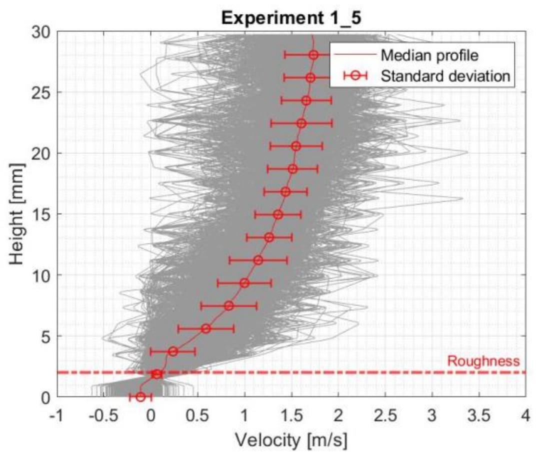

Figure A 53: Median profile R1 V2 repetition 2.

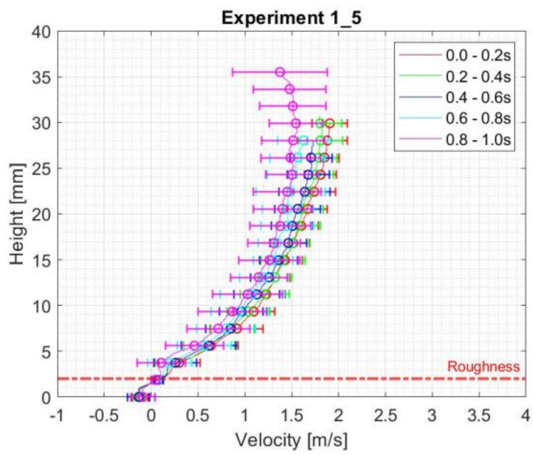

Figure A 54: Profiles over time R1 V2 repetition 2.

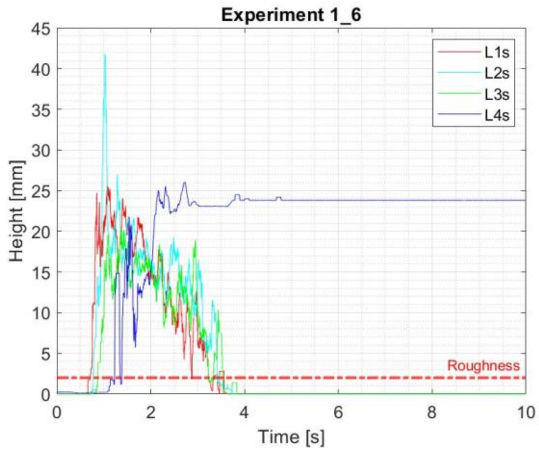

Figure A 55: Smoothed laser signals experiment R1 V2 repetition 3.

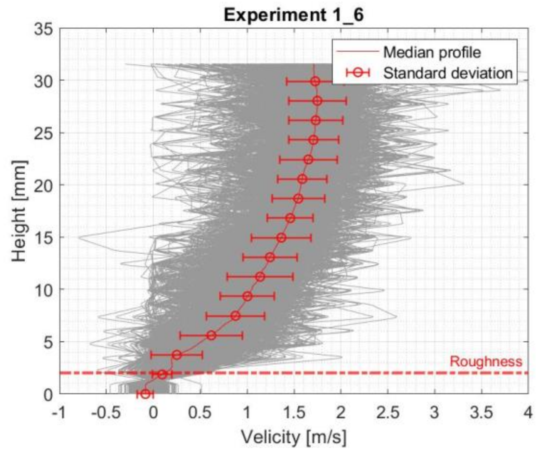

Figure A 56: Median profile R1 V2 repetition 3.

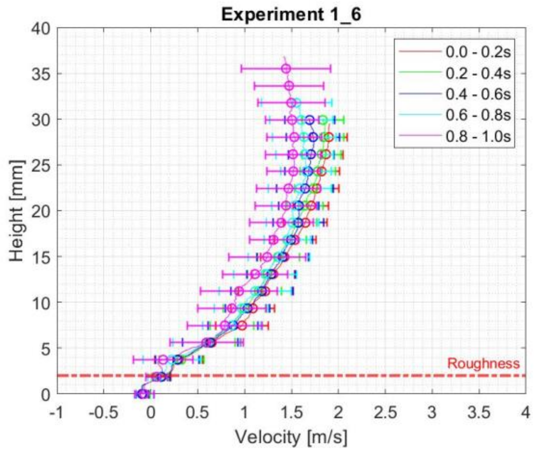

Figure A 57: Profiles over time R1 V2 repetition 3.

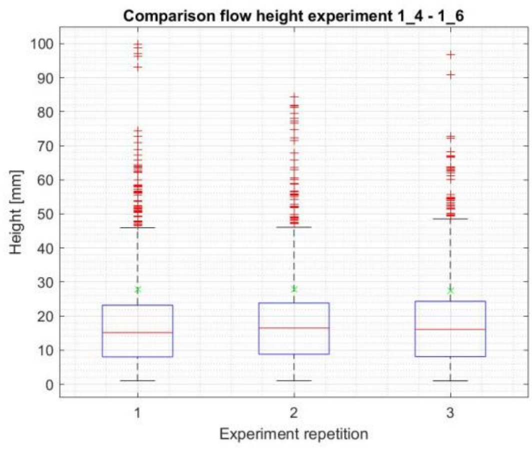

Figure A 58: Comparison boxplot flow heights R1 V2 repetition 1-3.

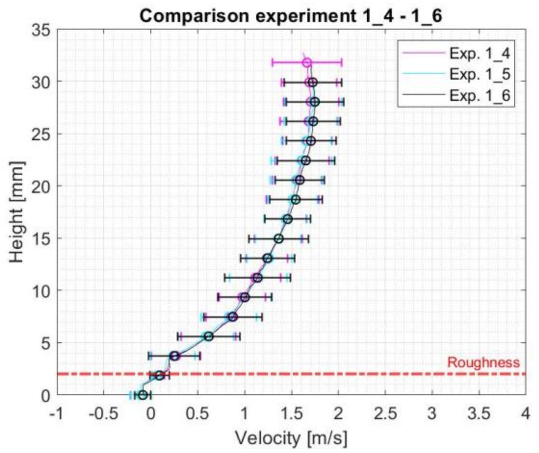

Figure A 59: Comparison profiles R1 V2 repetition 1-3.

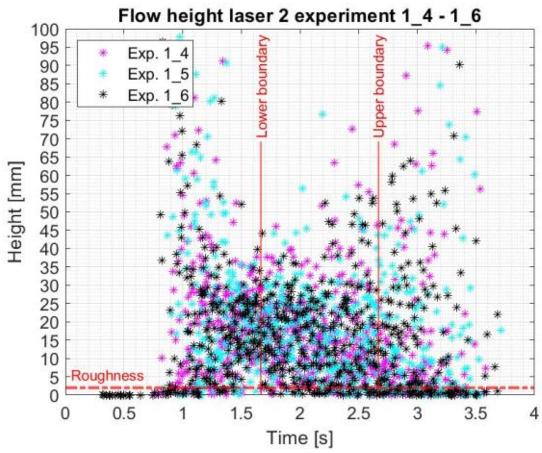

Figure A 60: Analysed section R1 V2 repetition 1-3.

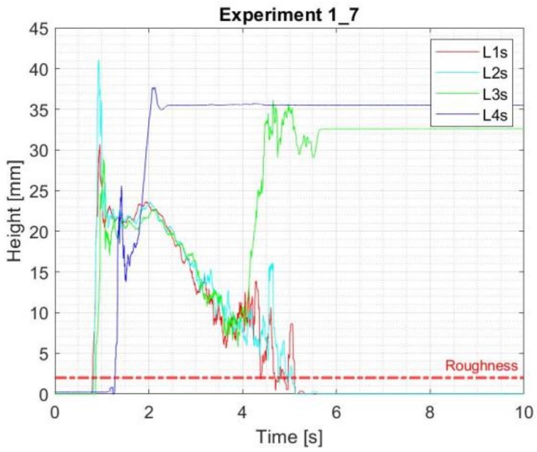

Figure A 61: Smoothed laser signals experiment R1 V3 repetition 1.

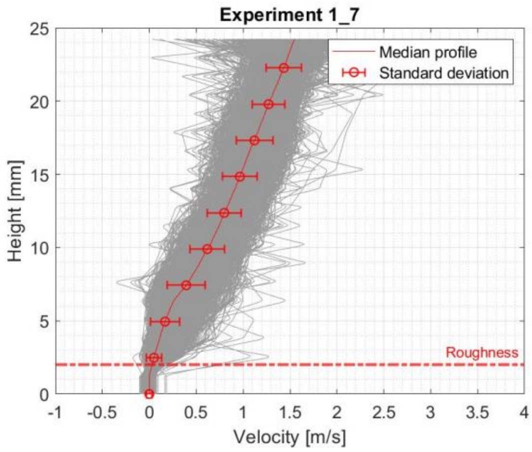

Figure A 62: Median profile R1 V3 repetition 1.

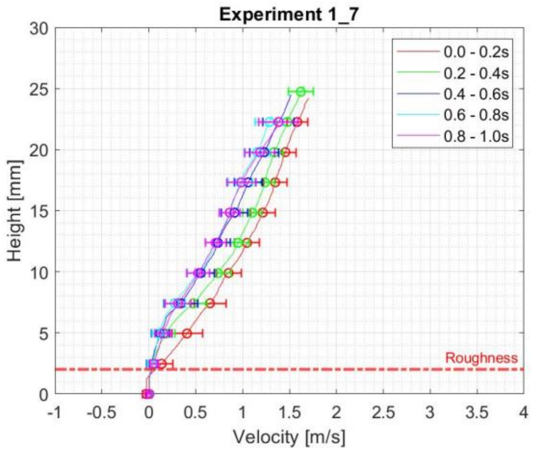

Figure A 63: Profiles over time R1 V3 repetition 1.

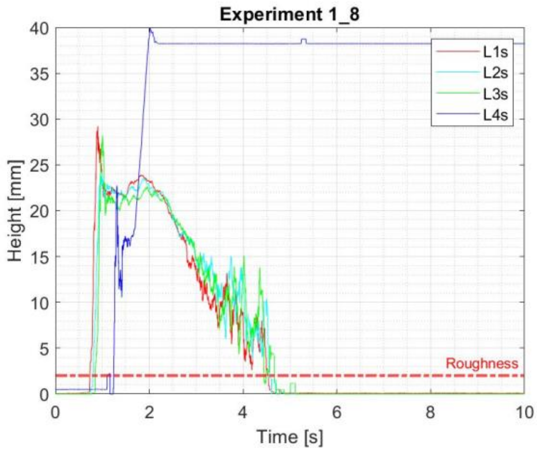

Figure A 64: Smoothed laser signals experiment R1 V3 repetition 2.

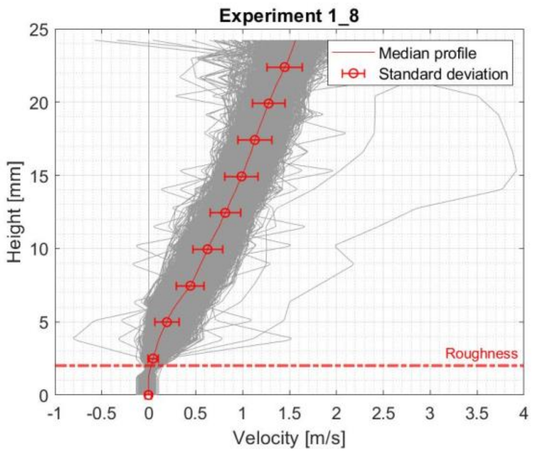

Figure A 65: Median profile R1 V3 repetition 2.

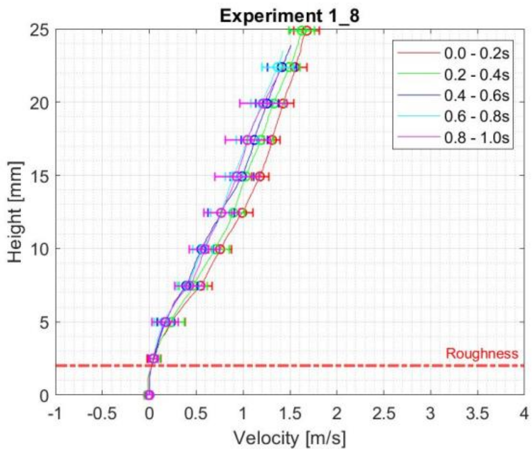

Figure A 66: Profiles over time R1 V3 repetition 2.

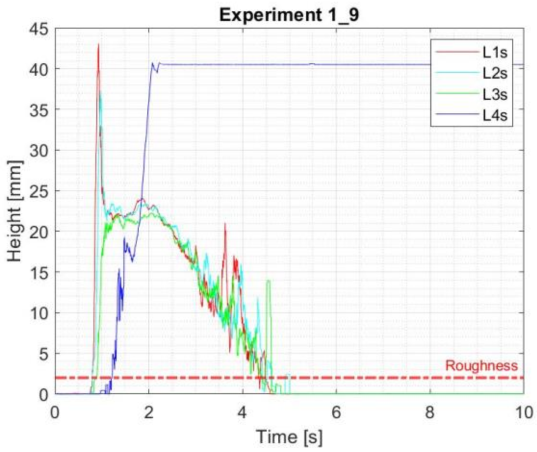

Figure A 67: Smoothed laser signals experiment R1 V3 repetition 3. (excluded from evaluation due to video failure)

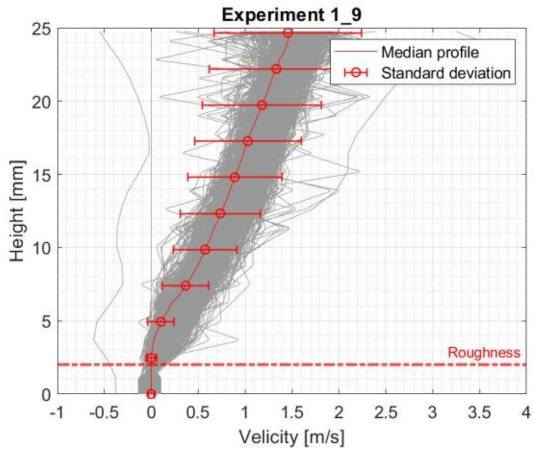

Figure A 68: Median profile R1 V3 repetition 3. (excluded from evaluation due to video failure)

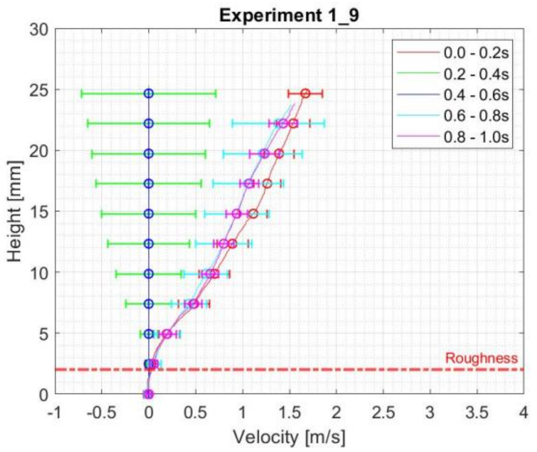

Figure A 69: Profiles over time R1 V3 repetition 3. (excluded from evaluation due to video failure)

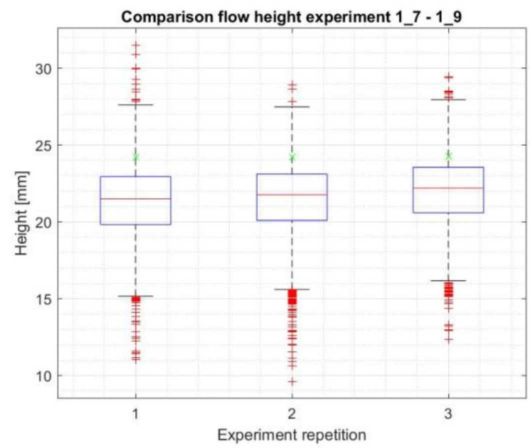

Figure A 70: Comparison boxplot flow heights R1 V3 repetition 1-3.

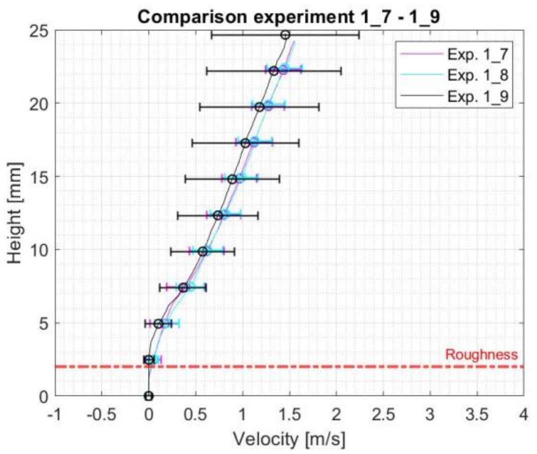

Figure A 71: Comparison profiles R1 V3repetition 1-3.

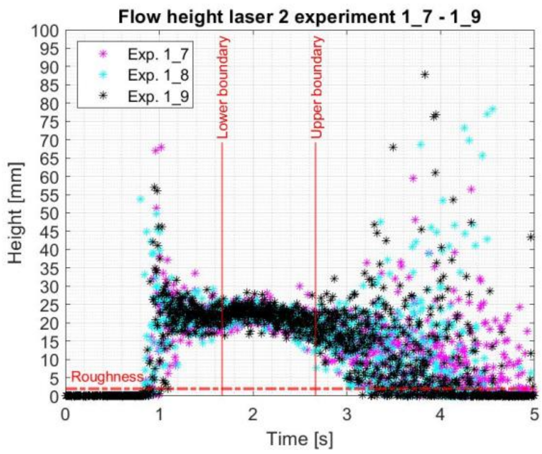

Figure A 72: Analysed section R1 V3 repetition 1-3.

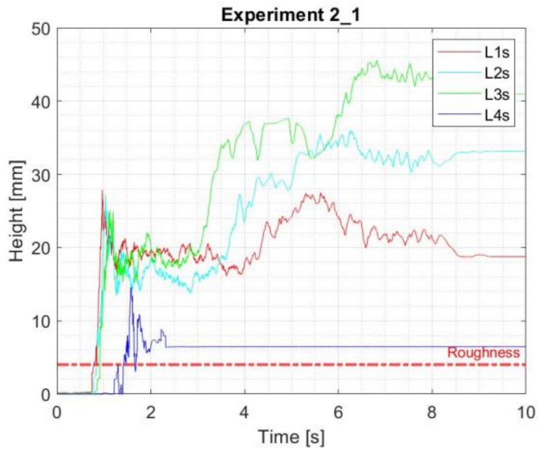

Figure A 73: Smoothed laser signals experiment R2 V1 repetition 1.

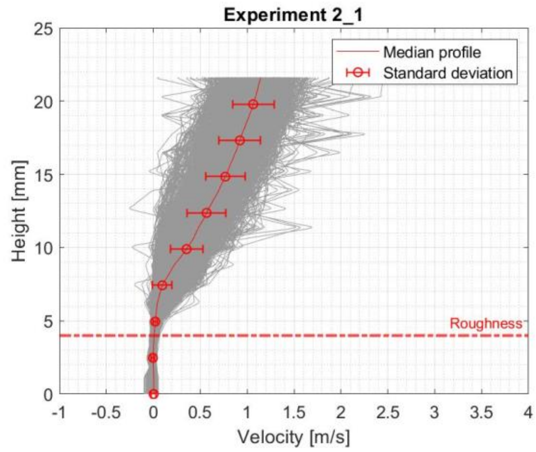

Figure A 74: Median profile R2 V1 repetition 1.

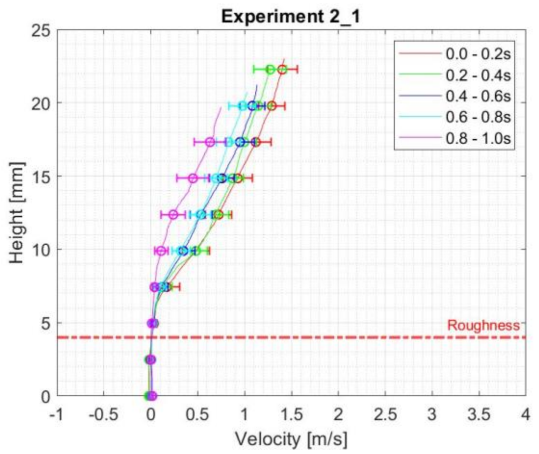

Figure A 75: Profiles over time R2 V1 repetition 1.

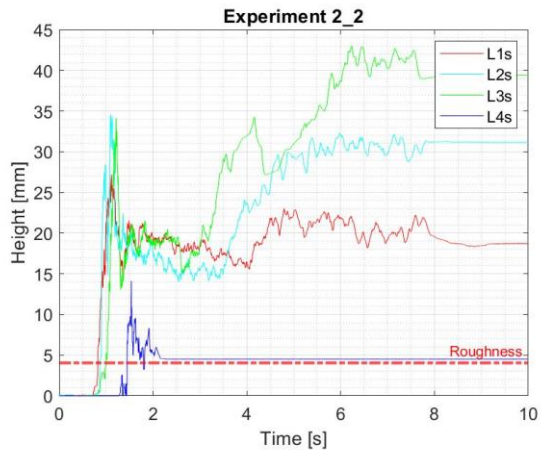

Figure A 76: Smoothed laser signals experiment R2 V1 repetition 2.

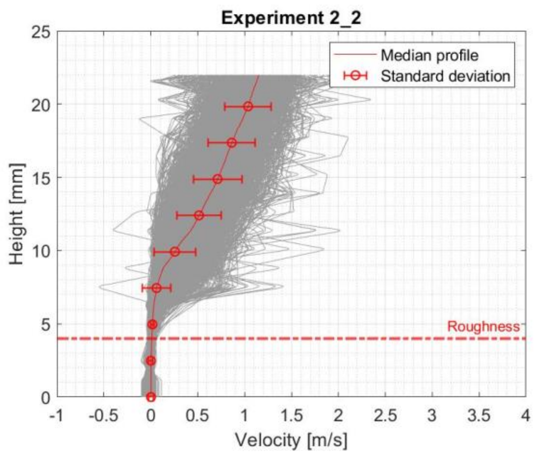

Figure A 77: Median profile R2 V1 repetition 2.

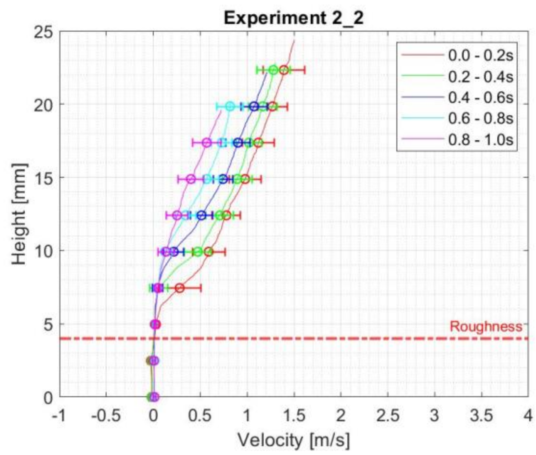

Figure A 78: Profiles over time R2 V1 repetition 2.

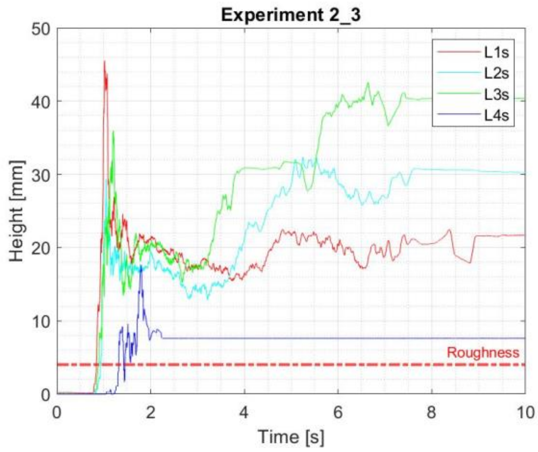

Figure A 79: Smoothed laser signals experiment R2 V1 repetition 3.

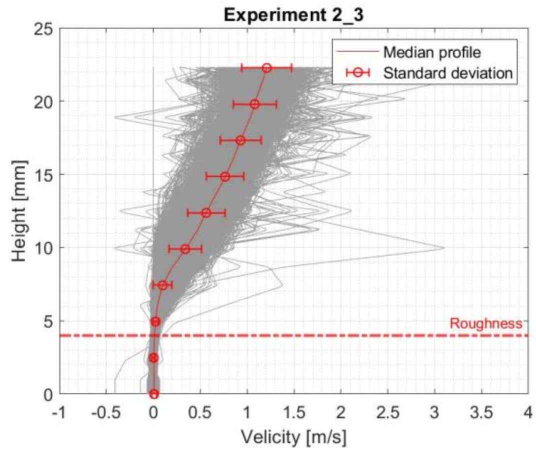

Figure A 80: Median profile R2 V1 repetition 3.

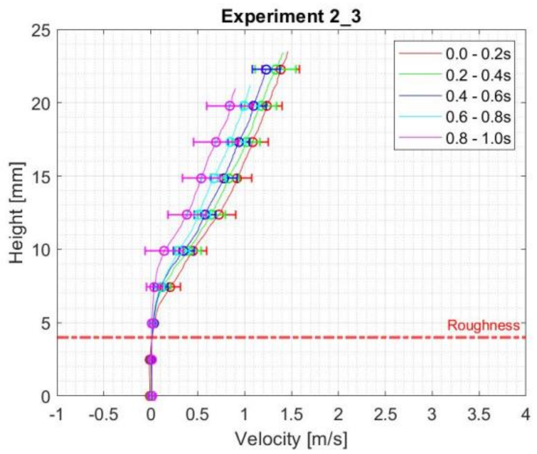

Figure A 81: Profiles over time R2 V1 repetition 3.

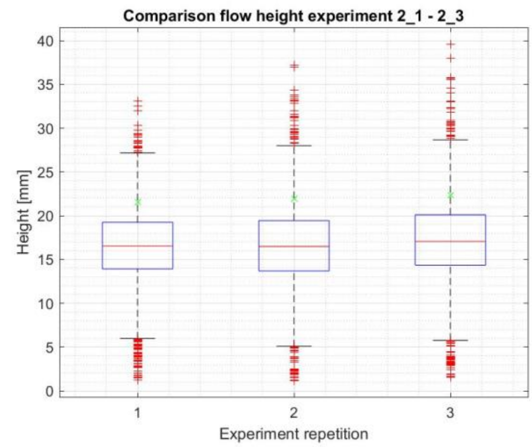

Figure A 82: Comparison boxplot flow heights R2 V1 repetition 1-3.

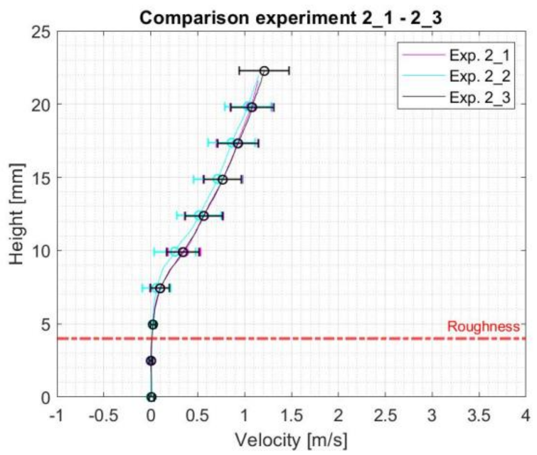

Figure A 83: Comparison profiles R2 V1 repetition 1-3.

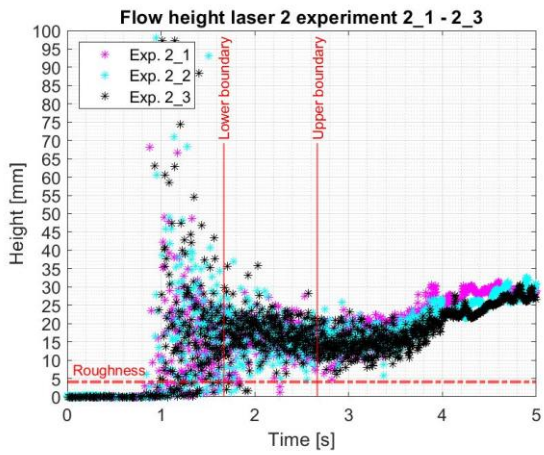

Figure A 84: Analysed section R2 V1 repetition 1-3.

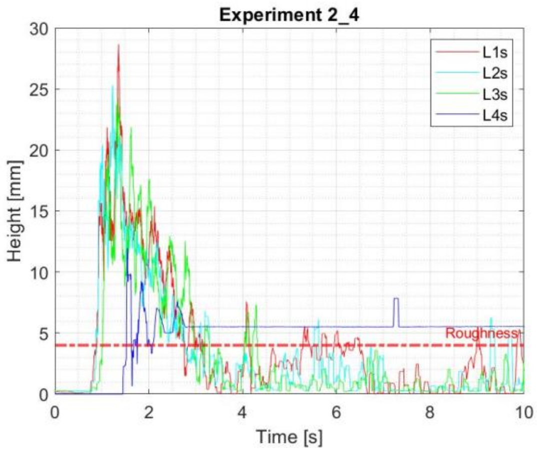

Figure A 85: Smoothed laser signals experiment R2 V2 repetition 1.

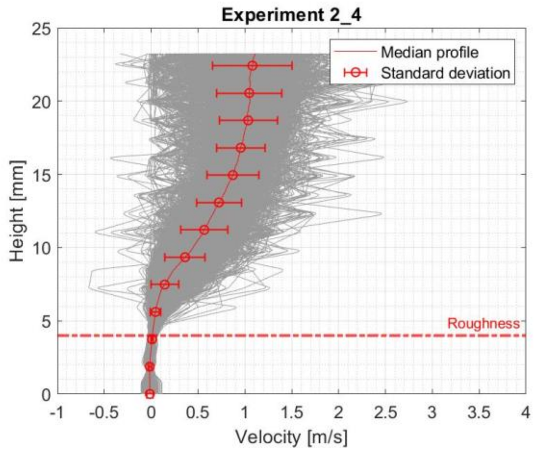

Figure A 86: Median profile R2 V2 repetition 1.

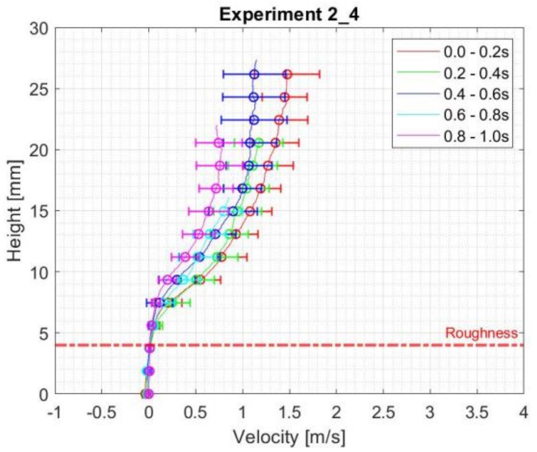

Figure A 87: Profiles over time R2 V2 repetition 1.

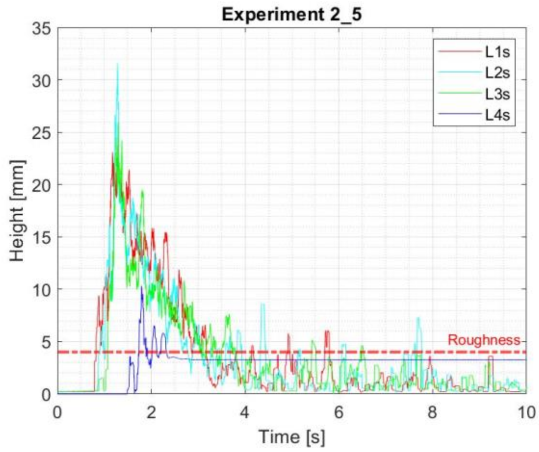

Figure A 88: Smoothed laser signals experiment R2 V2 repetition 2.

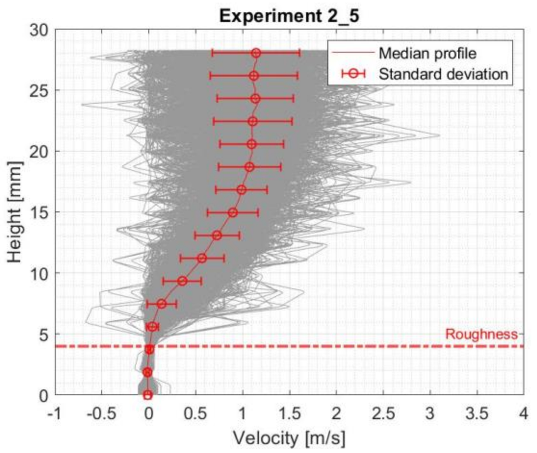

Figure A 89: Median profile R2 V2 repetition 2.

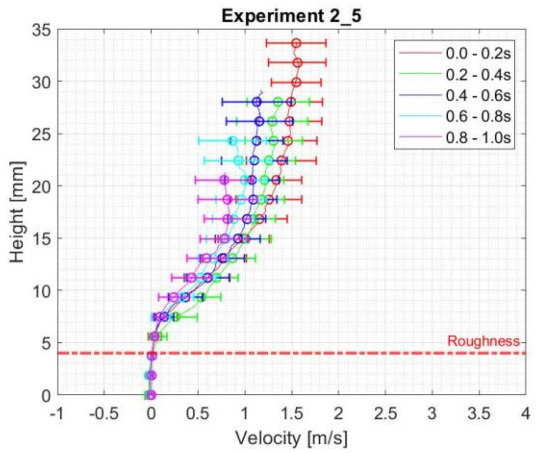

Figure A 90: Profiles over time R2 V2 repetition 2.

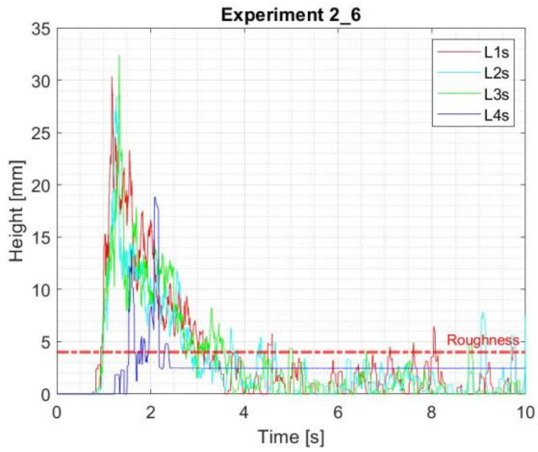

Figure A 91: Smoothed laser signals experiment R2 V2 repetition 3.

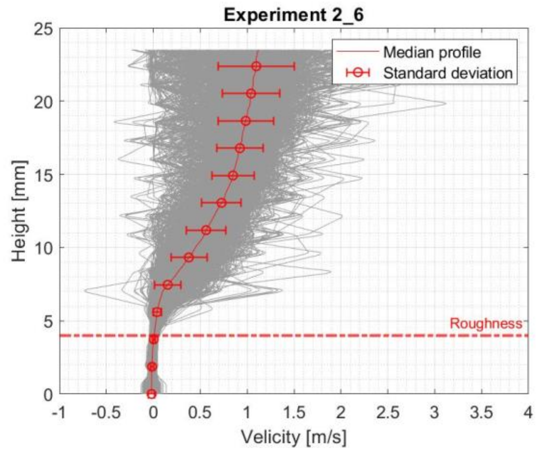

Figure A 92: Median profile R2 V2 repetition 3.

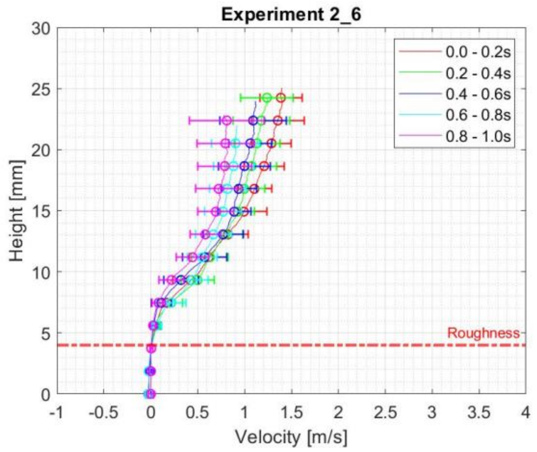

Figure A 93: Profiles over time R2 V2 repetition 3.

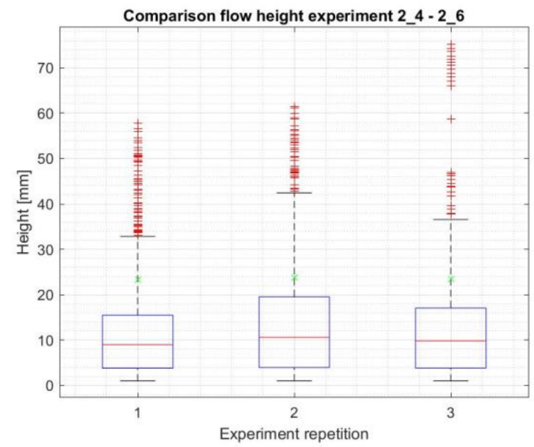

Figure A 94: Comparison boxplot flow heights R2 V2 repetition 1-3.

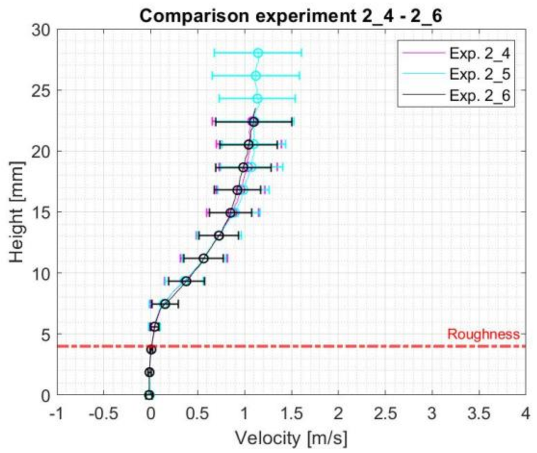

Figure A 95: Comparison profiles R2 V2 repetition 1-3.

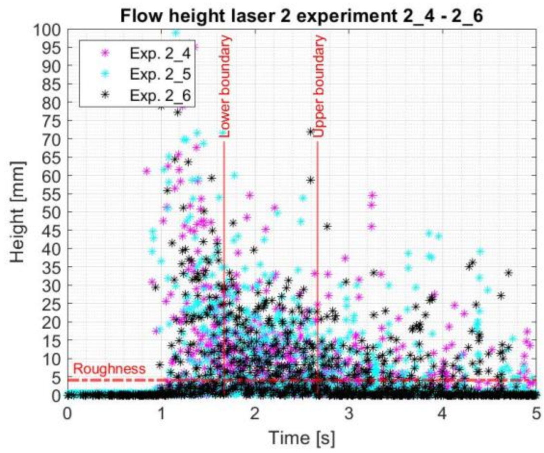

Figure A 96: Analysed section R2 V2 repetition 1-3.

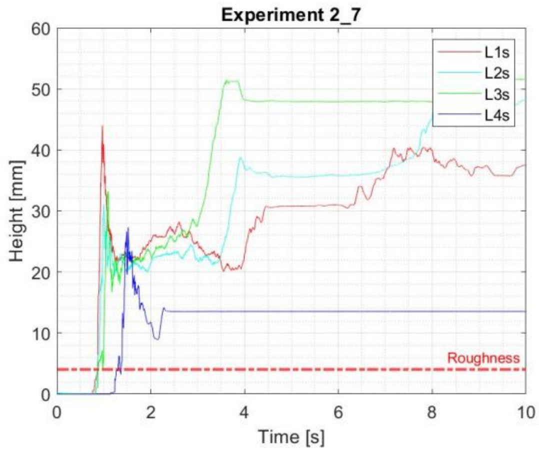

Figure A 97: Smoothed laser signals experiment R2 V3 repetition 1.

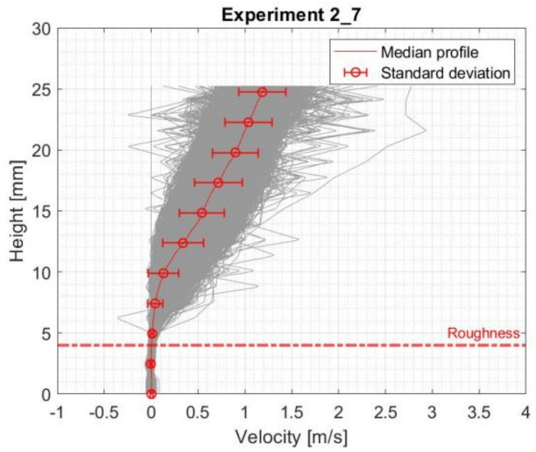

Figure A 98: Median profile R2 V3 repetition 1.

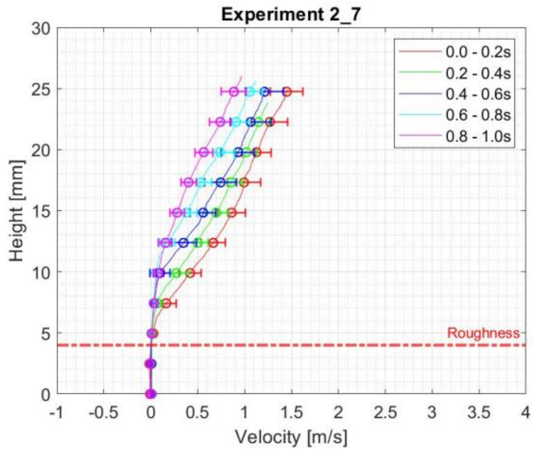

Figure A 99: Profiles over time R2 V3 repetition 1.

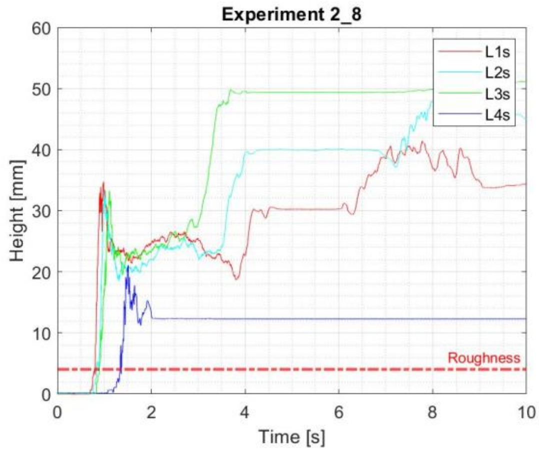

Figure A 100: Smoothed laser signals experiment R2 V3 repetition 2.

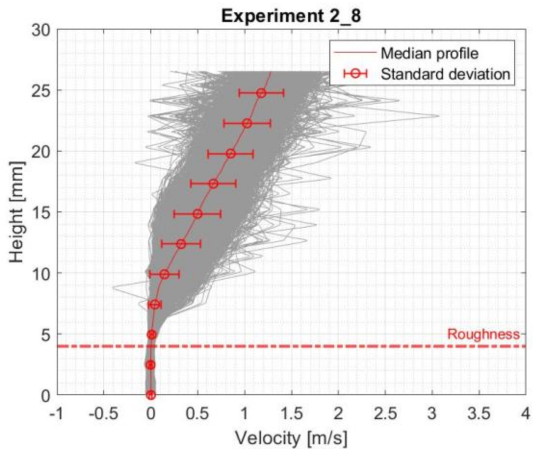

Figure A 101: Median profile R2 V3 repetition 2.

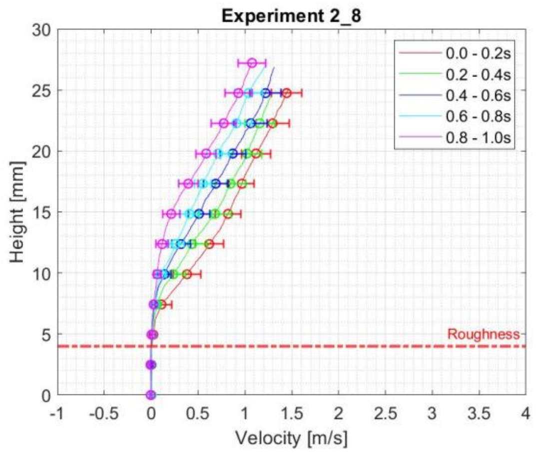

Figure A 102: Profiles over time R2 V3 repetition 2.

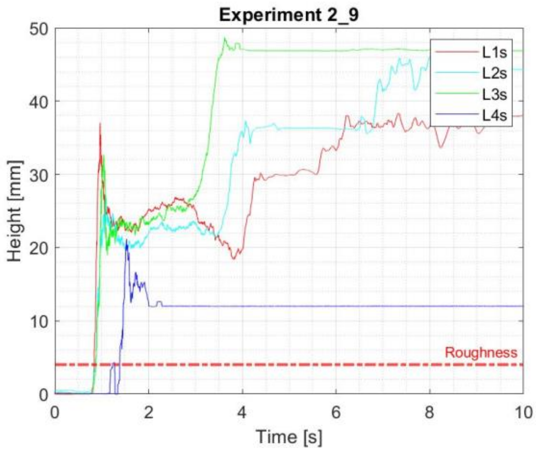

Figure A 103: Smoothed laser signals experiment R2 V3 repetition 3.

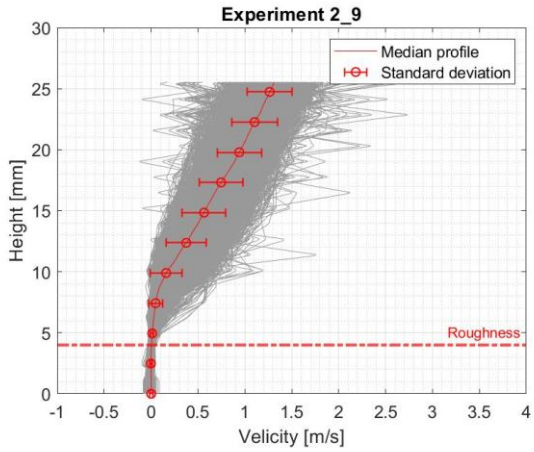

Figure A 104: Median profile R2 V3 repetition 3.

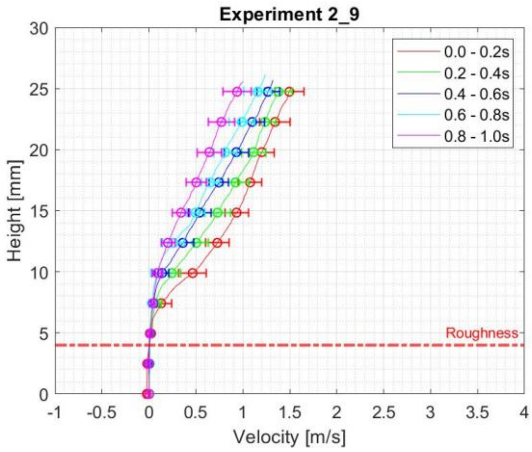

Figure A 105: Profiles over time R2 V3 repetition 3.

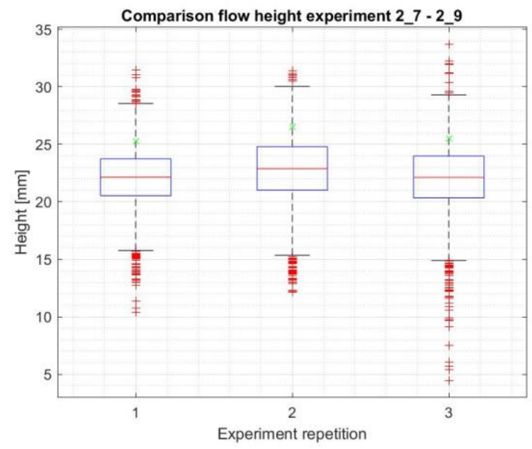

Figure A 106: Comparison boxplot flow heights R2 V3 repetition 1-3.

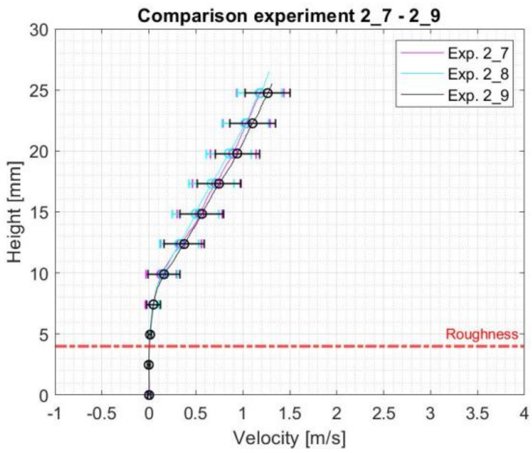

Figure A 107: Comparison profiles R2 V3 repetition 1-3.

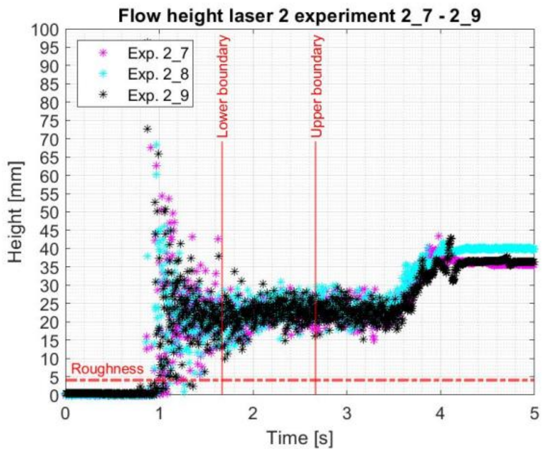

Figure A 108: Analysed section R2 V3 repetition 1-3.

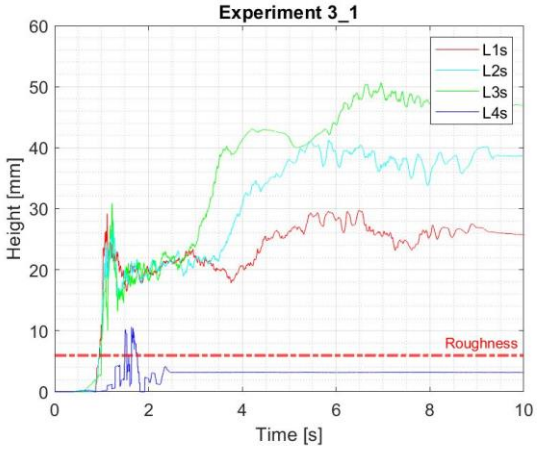

Figure A 109: Smoothed laser signals experiment R3 V1 repetition 1.

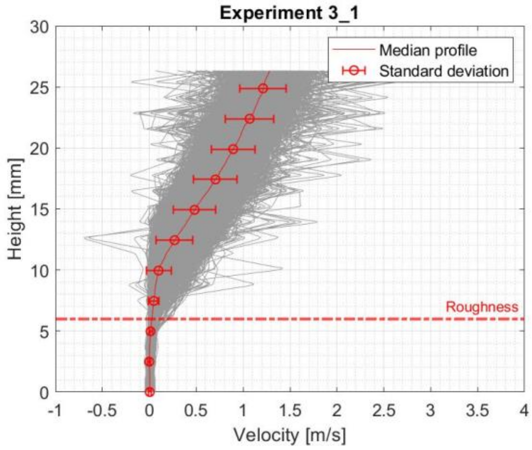

Figure A 110: Median profile R3 V1 repetition 1.

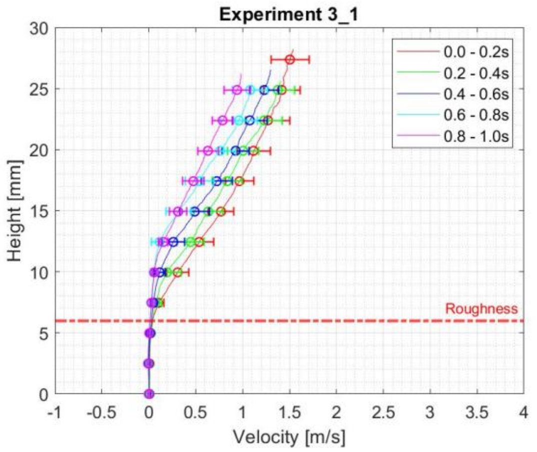

Figure A 111: Profiles over time R3 V1 repetition 1.

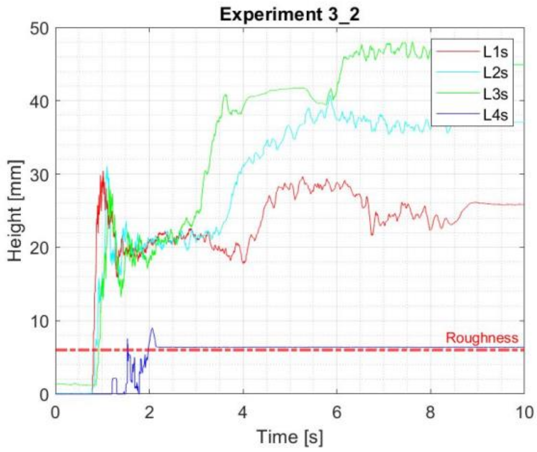

Figure A 112: Smoothed laser signals experiment R3 V1 repetition 2.

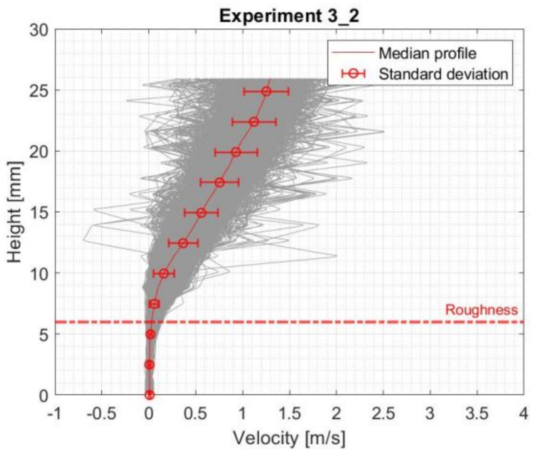

Figure A 113: Median profile R3 V1 repetition 2.

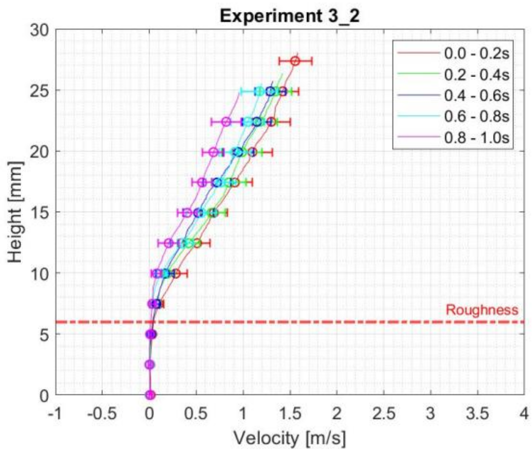

Figure A 114: Profiles over time R3 V1 repetition 2.

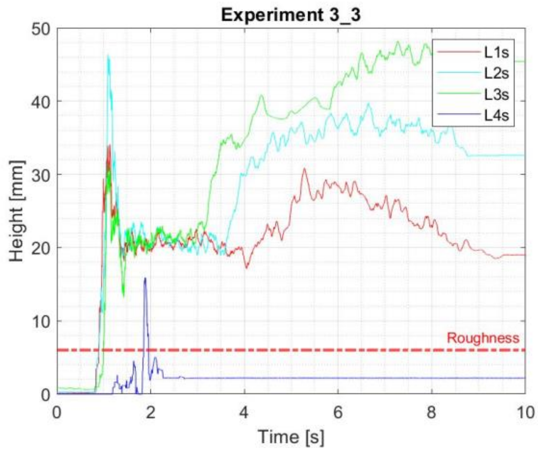

Figure A 115: Smoothed laser signals experiment R3 V1 repetition 3.

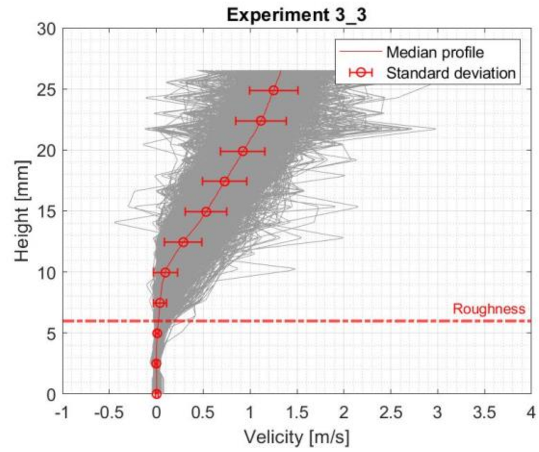

Figure A 116: Median profile R3 V1 repetition 3.

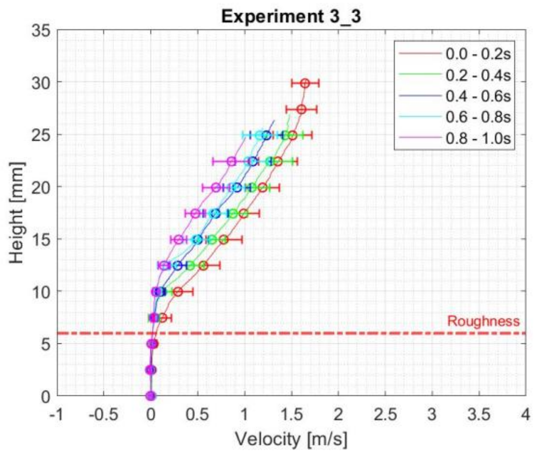

Figure A 117: Profiles over time R3 V1 repetition 3.

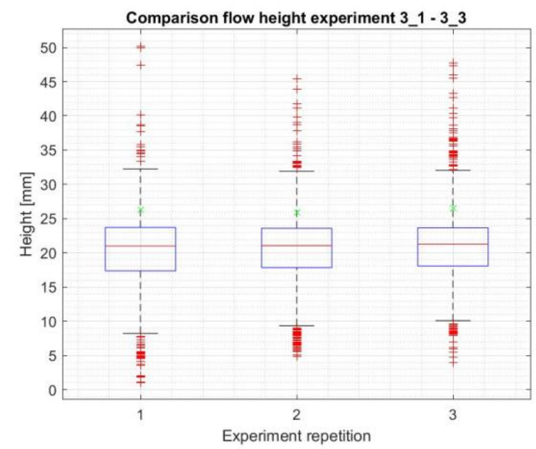

Figure A 118: Comparison boxplot flow heights R3 V1 repetition 1-3.

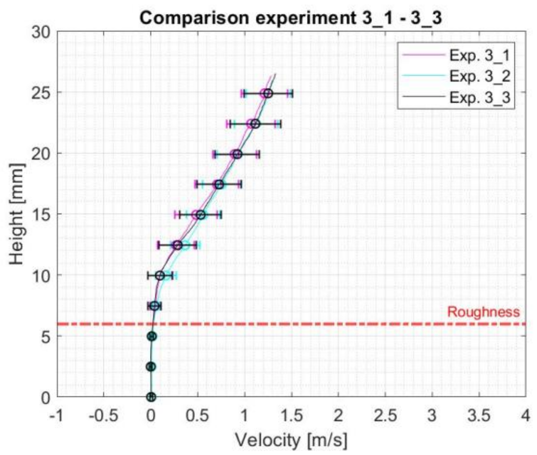

Figure A 119: Comparison profiles R3 V1 repetition 1-3.

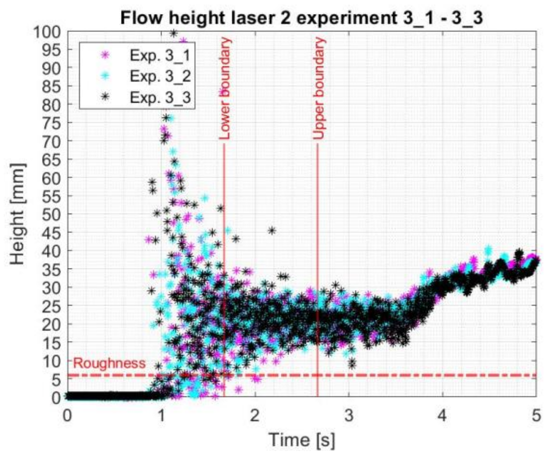

Figure A 120: Analysed section R3 V1 repetition 1-3.

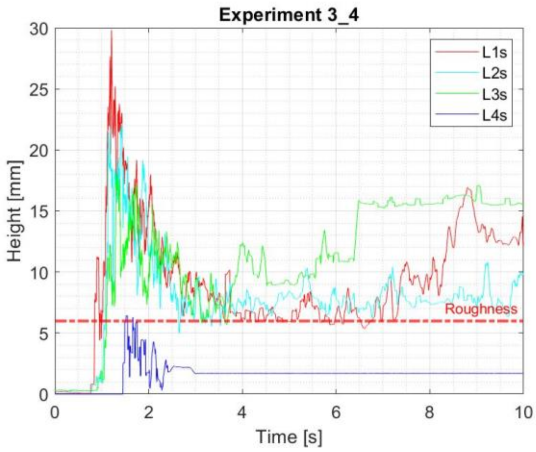

Figure A 121: Smoothed laser signals experiment R3 V2 repetition 1.

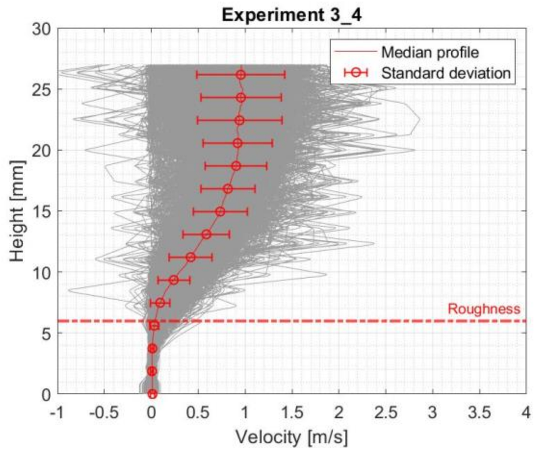

Figure A 122: Median profile R3 V2 repetition 1.

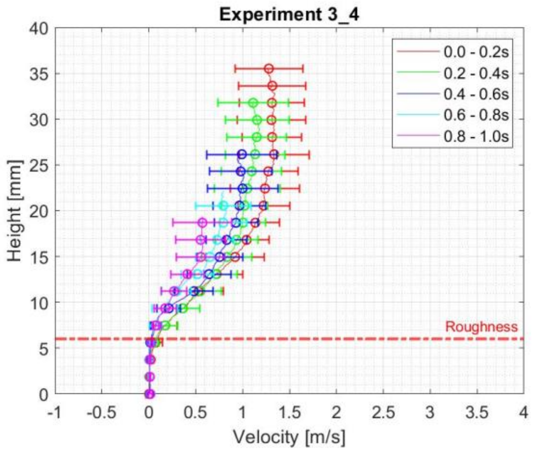

Figure A 123: Profiles over time R3 V2 repetition 1.

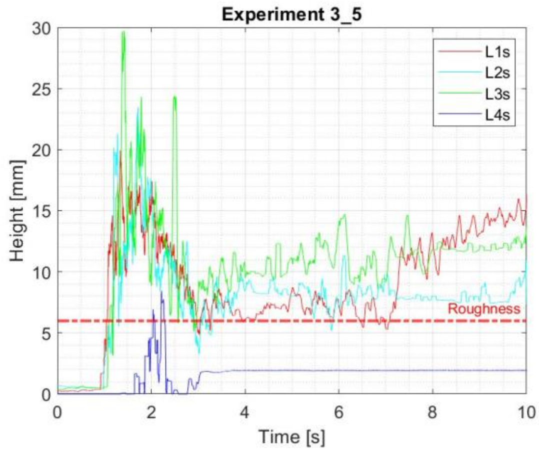

Figure A 124: Smoothed laser signals experiment R3 V2 repetition 2.

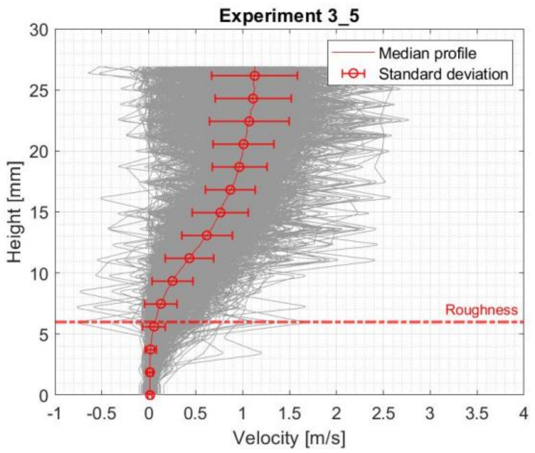

Figure A 125: Median profile R3 V2 repetition 2.

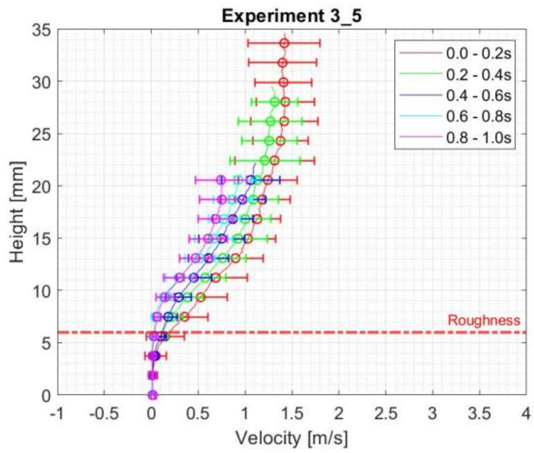

Figure A 126: Profiles over time R3 V2 repetition 2.

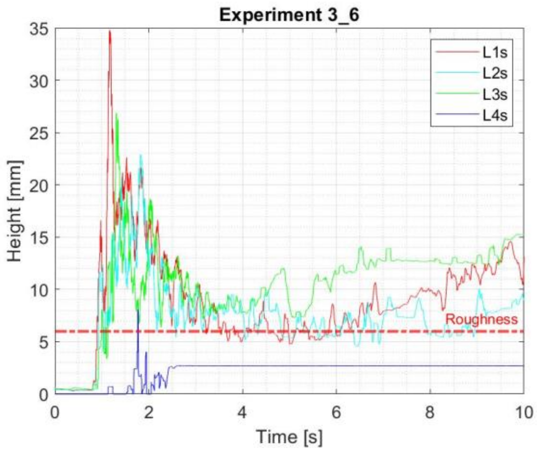

Figure A 127: Smoothed laser signals experiment R3 V2 repetition 3.

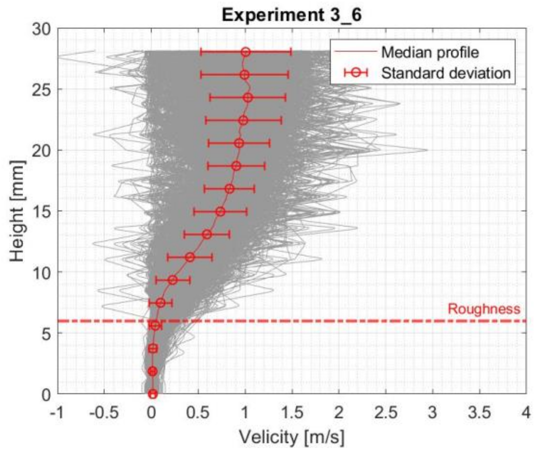

Figure A 128: Median profile R3 V2 repetition 3.

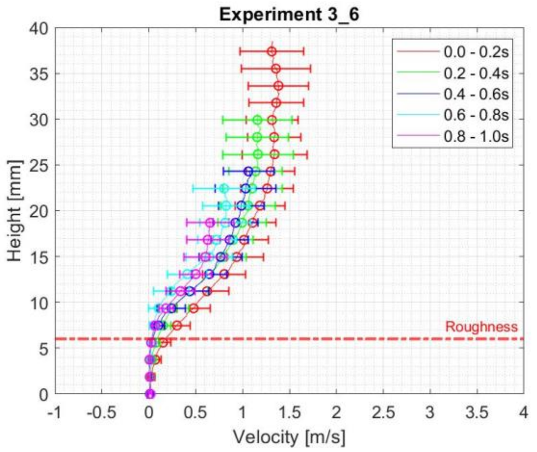

Figure A 129: Profiles over time R3 V2 repetition 3.

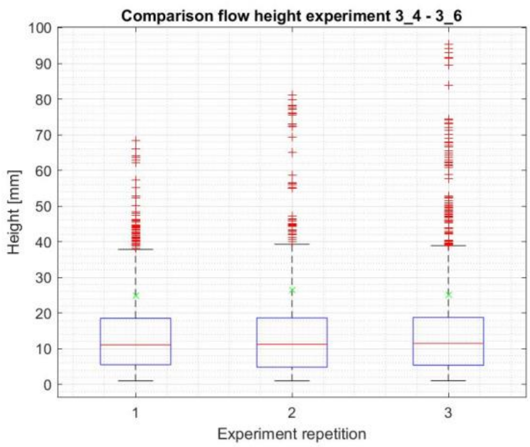

Figure A 130: Comparison boxplot flow heights R3 V2 repetition 1-3.

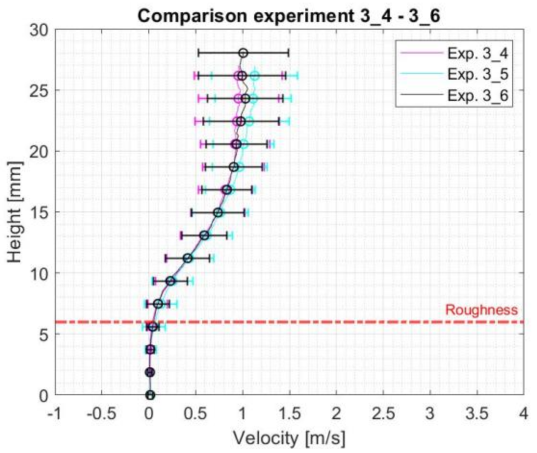

Figure A 131: Comparison profiles R3 V2 repetition 1-3.

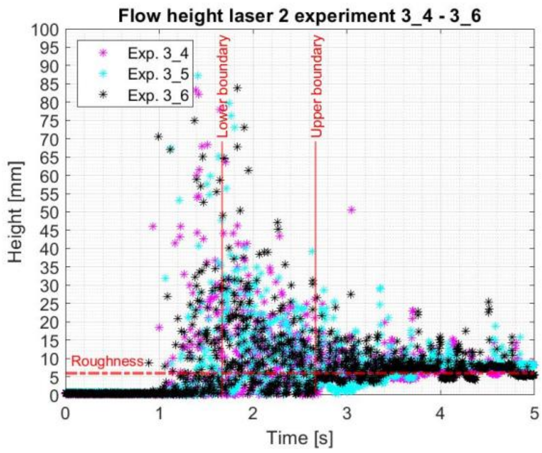

Figure A 132: Analysed section R3 V2 repetition 1-3.

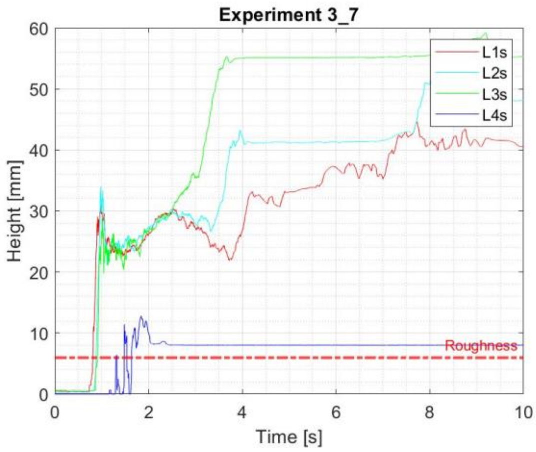

Figure A 133: Smoothed laser signals experiment R3 V3 repetition 1.

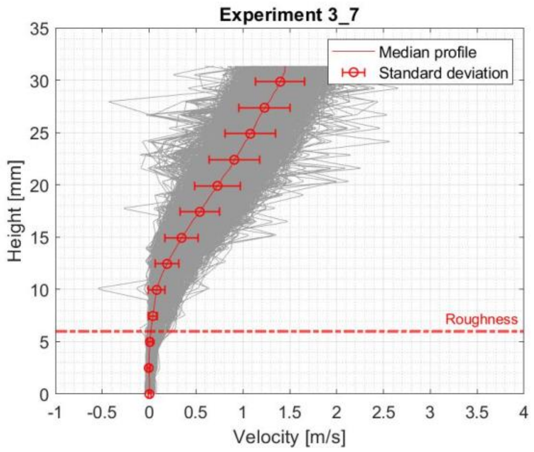

Figure A 134: Median profile R3 V3 repetition 1.

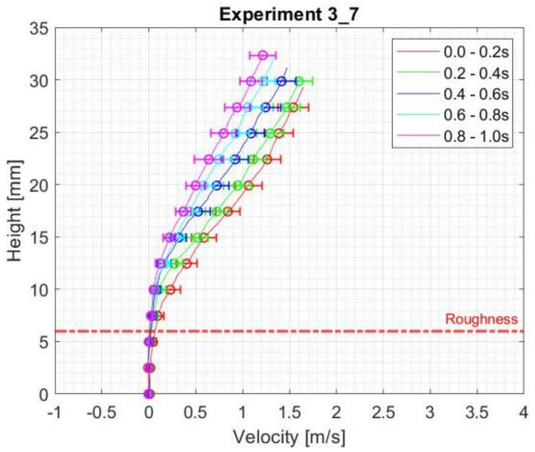

Figure A 135: Profiles over time R3 V3 repetition 1.

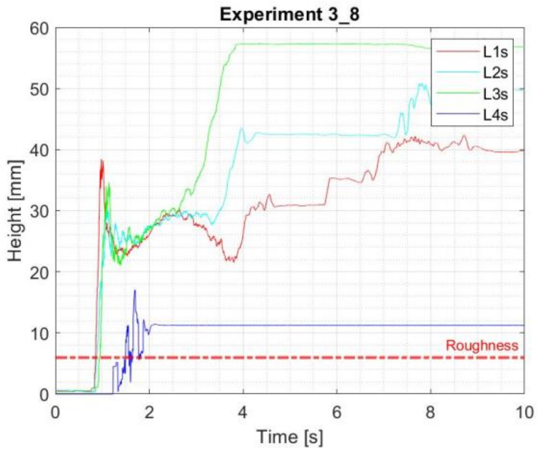

Figure A 136: Smoothed laser signals experiment R3 V3 repetition 2.

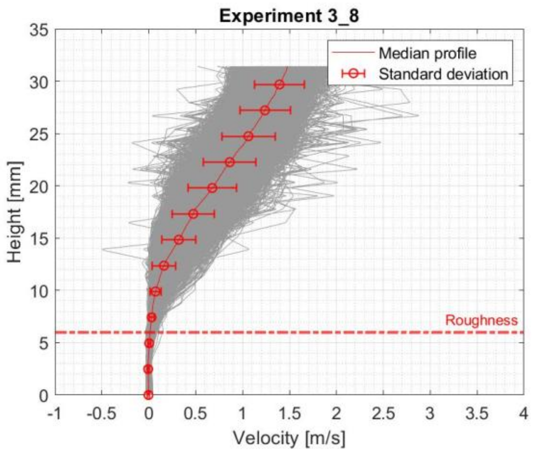

Figure A 137: Median profile R3 V3 repetition 2.

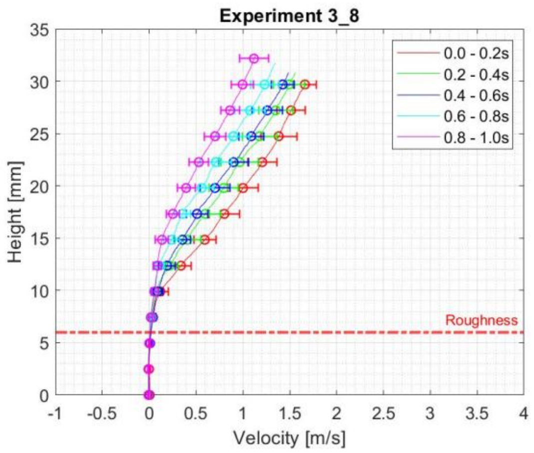

Figure A 138: Profiles over time R3 V3 repetition 2.

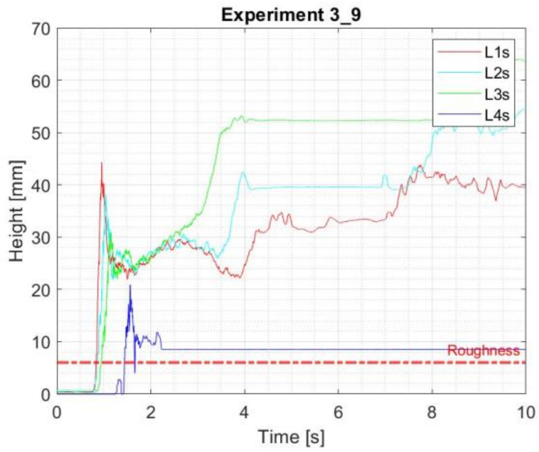

Figure A 139: Smoothed laser signals experiment R3 V3 repetition 3.

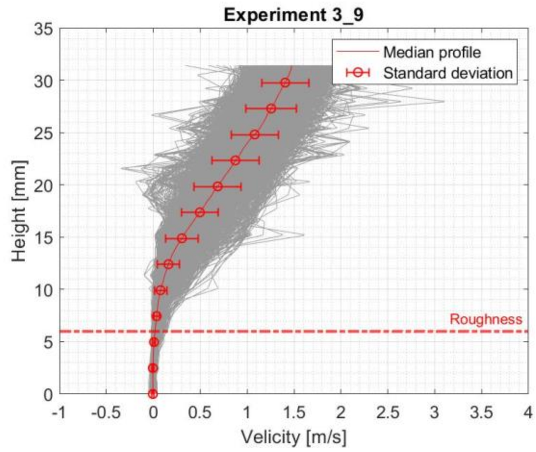

Figure A 140: Median profile R3 V3 repetition 3.

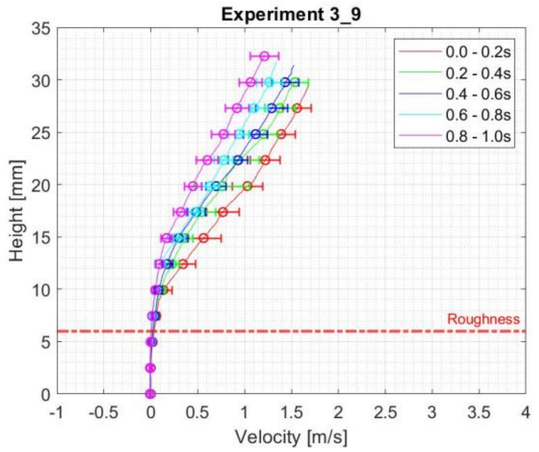

Figure A 141: Profiles over time R3 V3 repetition 3.

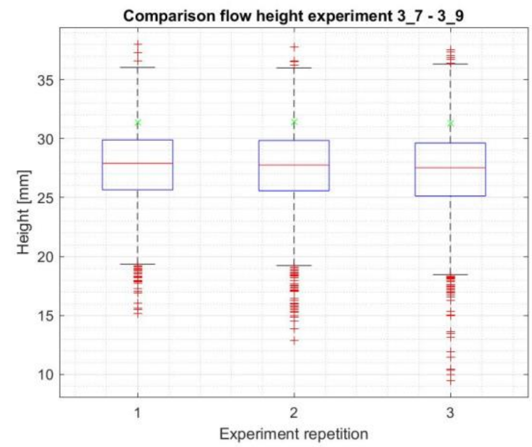

Figure A 142: Comparison boxplot flow heights R3 V3 repetition 1-3.

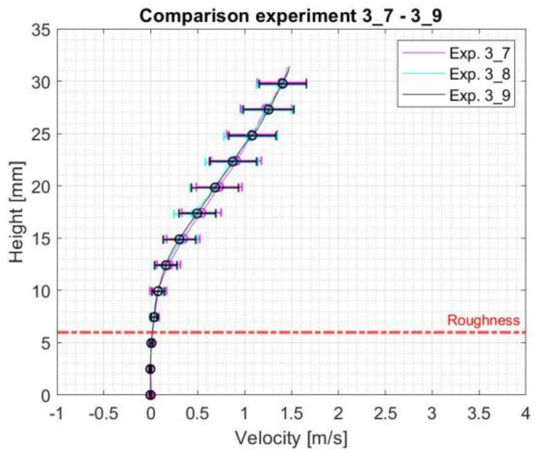

Figure A 143: Comparison profiles R3 V3 repetition 1-3.

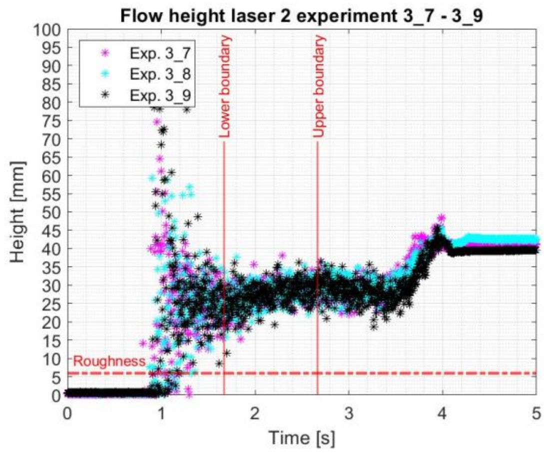

Figure A 144: Analysed section R3 V3 repetition 1-3.

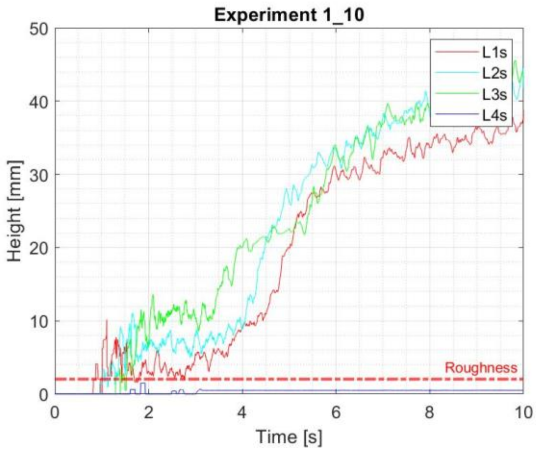

Figure A 145: Smoothed laser signals experiment R1W V1 repetition 1.

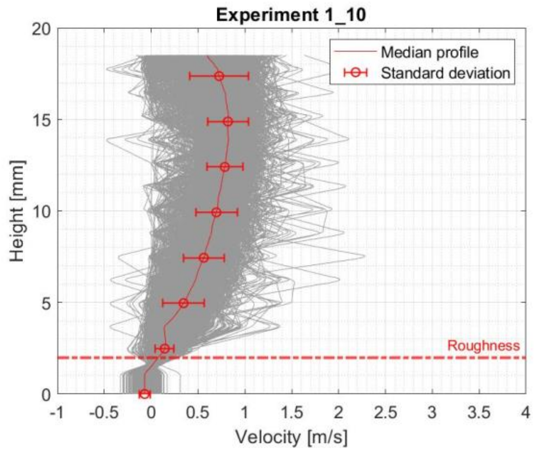

Figure A 146: Median profile R1W V1 repetition 1.

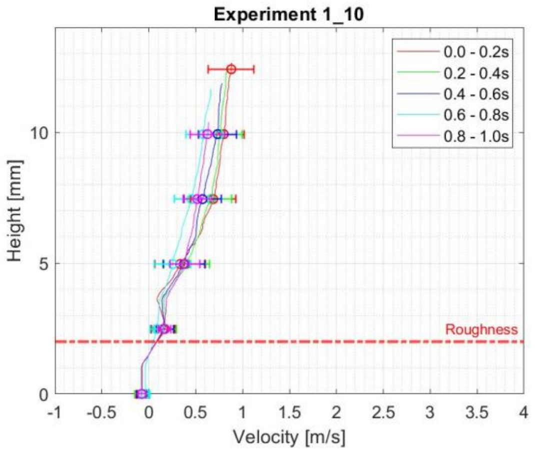

Figure A 147: Profiles over time R1W V1 repetition 1.

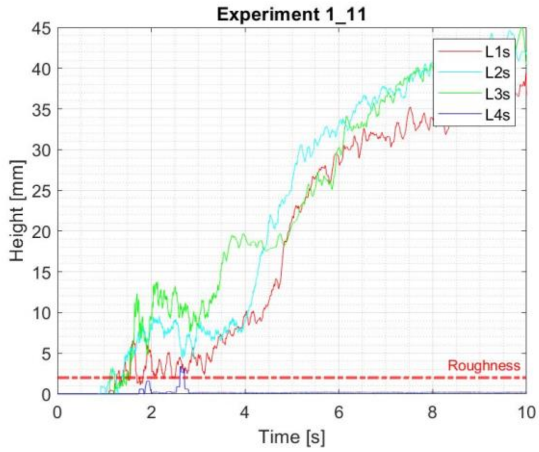

Figure A 148: Smoothed laser signals experiment R1W V1 repetition 2.

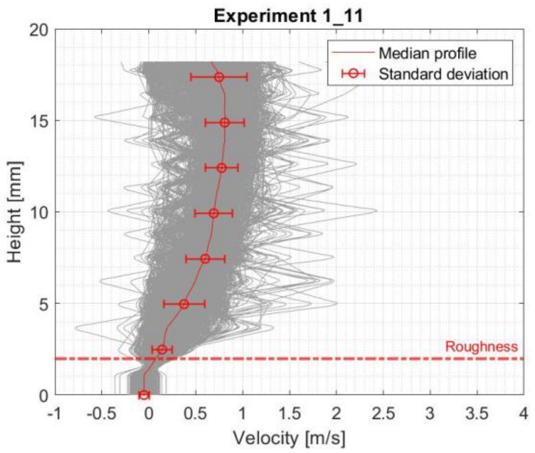

Figure A 149: Median profile R1W V1 repetition 2.

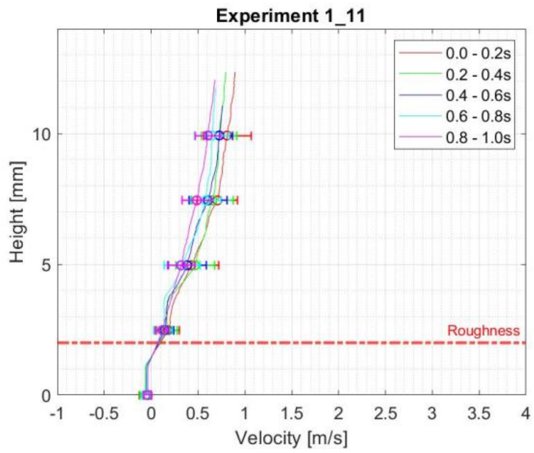

Figure A 150: Profiles over time R1W V1 repetition 2.

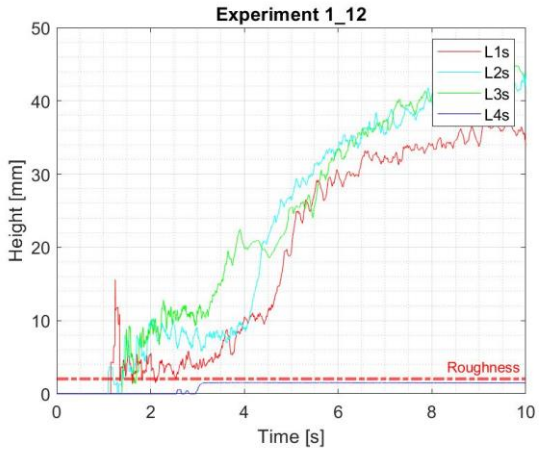

Figure A 151: Smoothed laser signals experiment R1W V1 repetition 3.

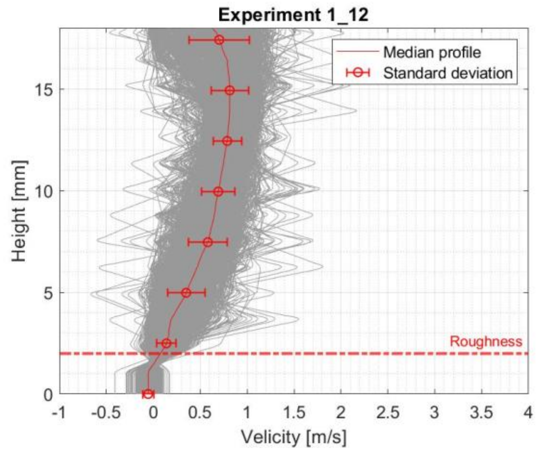

Figure A 152: Median profile R1W V1 repetition 3.

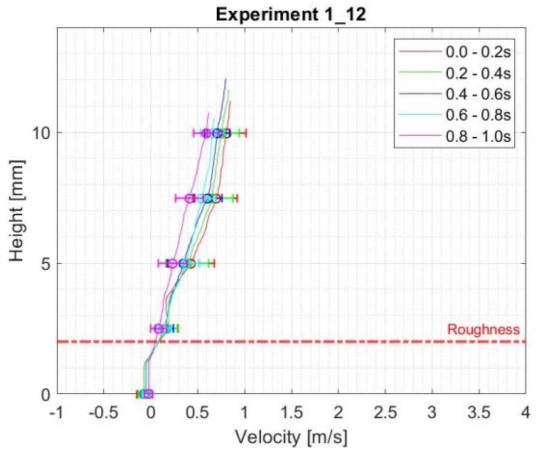

Figure A 153: Profiles over time R1W V1 repetition 3.

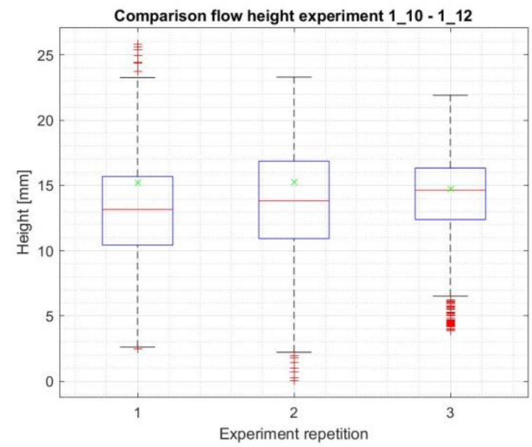

Figure A 154: Comparison boxplot flow heights R1W V1 repetition 1-3.

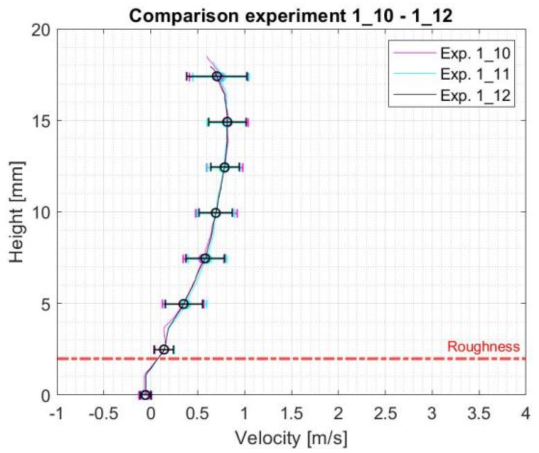

Figure A 155: Comparison profiles R1W V1 repetition 1-3.

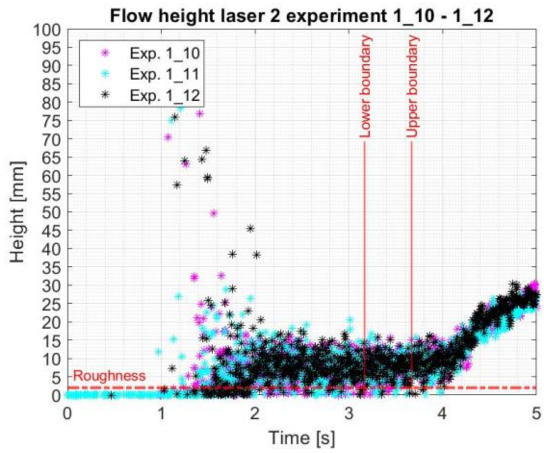

Figure A 156: Analysed section R1W V1 repetition 1-3.

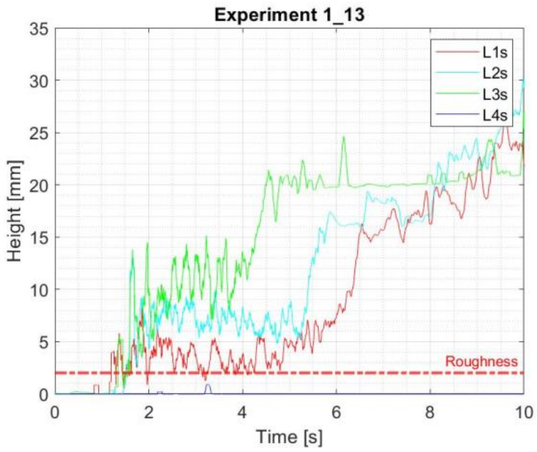

Figure A 157: Smoothed laser signals experiment R1W V2 repetition 1.

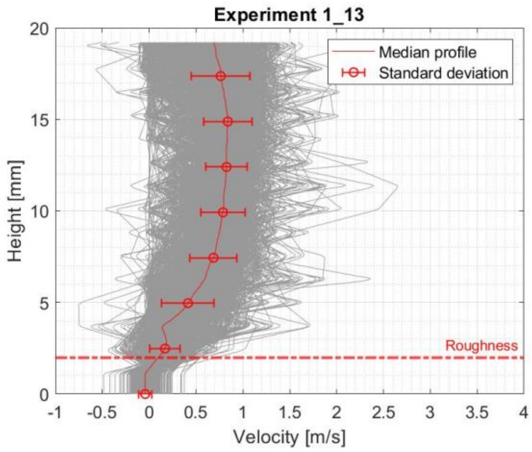

Figure A 158: Median profile R1W V2 repetition 1.

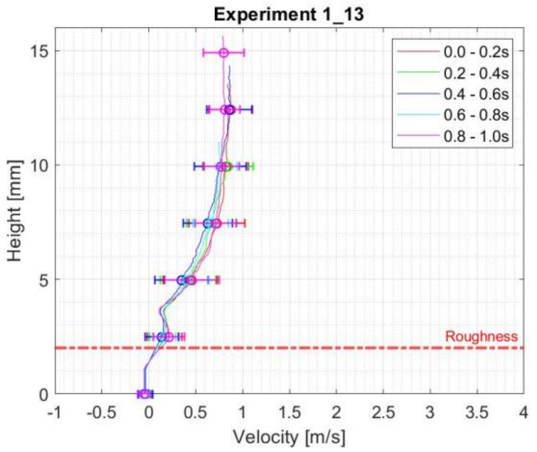

Figure A 159: Profiles over time R1W V2 repetition 1.

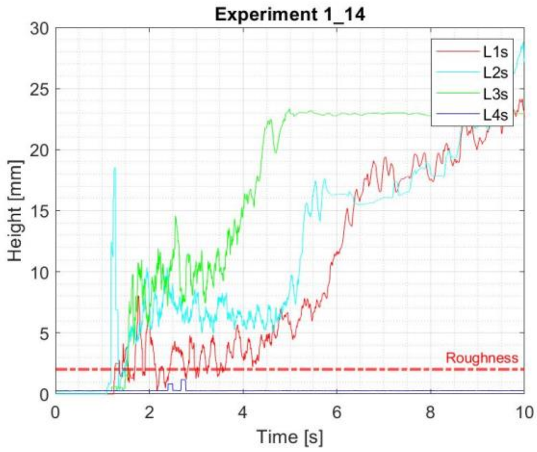

Figure A 160: Smoothed laser signals experiment R1W V2 repetition 2.

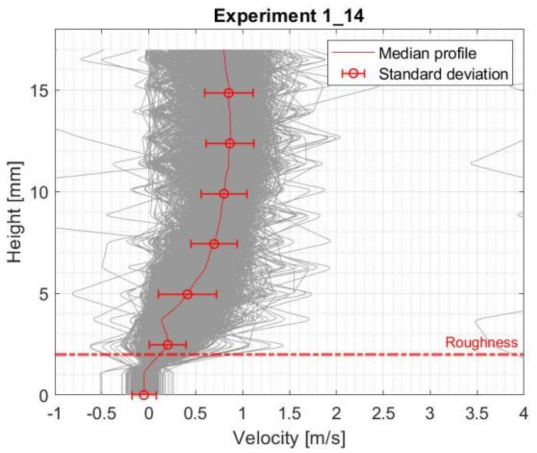

Figure A 161: Median profile R1W V2 repetition 2.

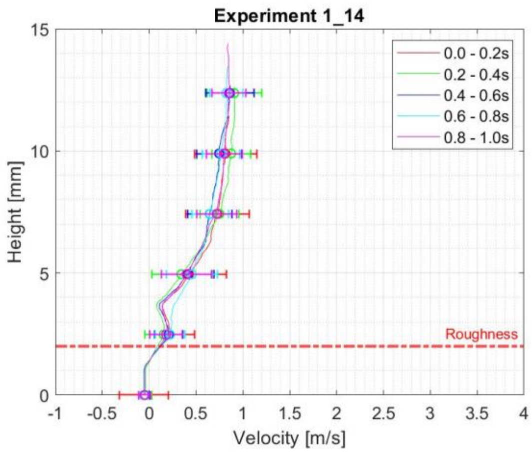

Figure A 162: Profiles over time R1W V2 repetition 2.

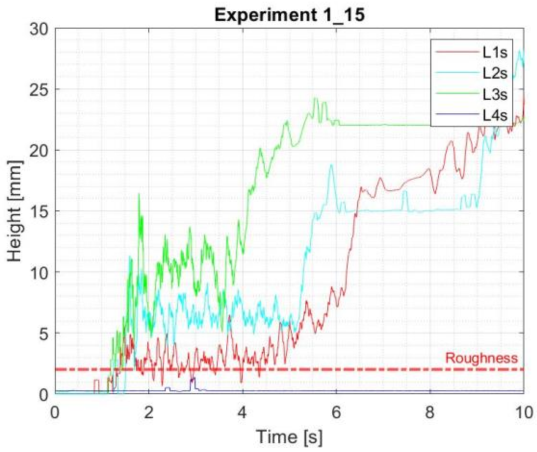

Figure A 163: Smoothed laser signals experiment R1W V2 repetition 3.

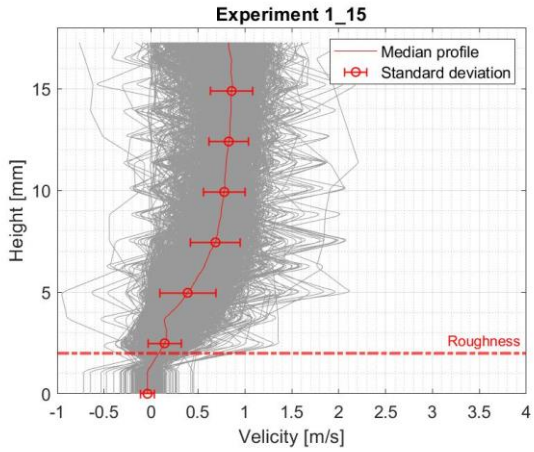

Figure A 164: Median profile R1W V2 repetition 3.

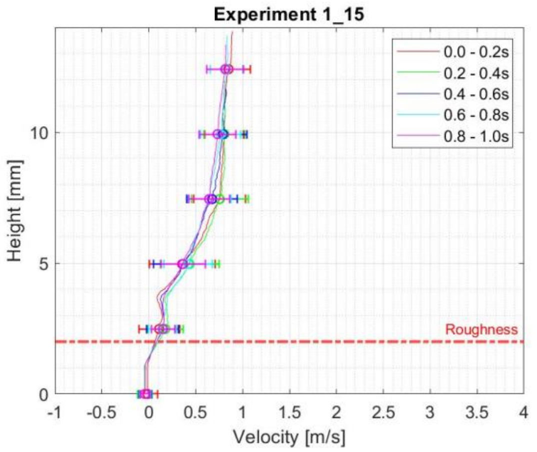

Figure A 165: Profiles over time R1W V2 repetition 3.

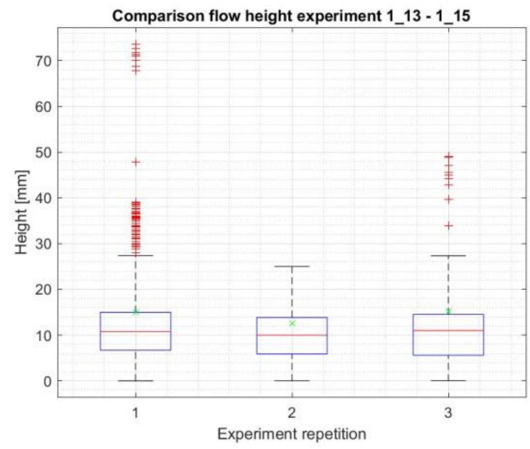

Figure A 166: Comparison boxplot flow heights R1W V2 repetition 1-3.

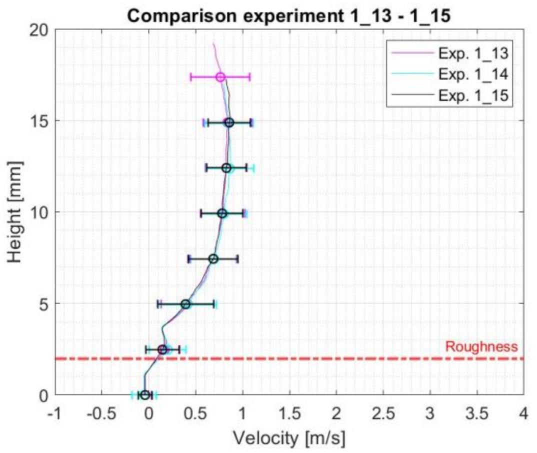

Figure A 167: Comparison profiles R1W V2 repetition 1-3.

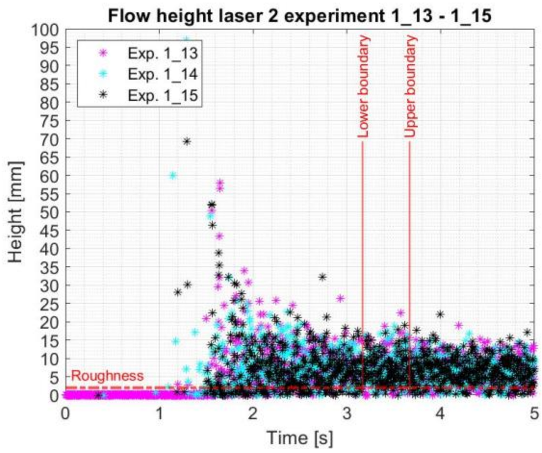

Figure A 168: Analysed section R1W V2 repetition 1-3.